

Electronic Thesis and Dissertation Repository

7-12-2022 2:00 PM

Magnetic Resonance Systems Development for Point-of-Care MRI Platforms

Eric J. Lessard, *The University of Western Ontario*

Supervisor: Chronik, Blaine A, *The University of Western Ontario*

A thesis submitted in partial fulfillment of the requirements for the Doctor of Philosophy degree in Medical Biophysics

© Eric J. Lessard 2022

Follow this and additional works at: <https://ir.lib.uwo.ca/etd>



Part of the [Medical Biophysics Commons](#), and the [Other Physics Commons](#)

Recommended Citation

Lessard, Eric J., "Magnetic Resonance Systems Development for Point-of-Care MRI Platforms" (2022). *Electronic Thesis and Dissertation Repository*. 8640.
<https://ir.lib.uwo.ca/etd/8640>

This Dissertation/Thesis is brought to you for free and open access by Scholarship@Western. It has been accepted for inclusion in Electronic Thesis and Dissertation Repository by an authorized administrator of Scholarship@Western. For more information, please contact wlsadmin@uwo.ca.

Abstract

Magnetic resonance imaging utilizes electromagnets to produce anatomical images in both clinical and research settings. In the race towards increasing performance head-optimized scanners have begun playing a significant role in providing high quality imaging of the head. However, they are implemented using smaller geometries and as such fail to allow entrance of the patient past their shoulders. This is overcome by designing asymmetric gradient coils which have their imaging region located towards one end of the gradient coil, as opposed to the geometric center, allowing brain imaging. There exists interest in compact configurations which allow imaging further into the cervical spine which is unfeasible using current asymmetric gradients. This work seeks to explore the design of asymmetric gradient coils with shoulder cut-outs to enable neck imaging by allowing the patient to enter further into the gradient coil while maintaining the small inner radius of a head-only platform.

First, the relative trade-offs in designing an asymmetric shoulder cut-out gradient coil are explored and extended by rotating the transverse gradient axes to produce gradient coils which compensate for some of the electromagnetic burden due to the loss of conducting surfaces on the sides. Next, a complementary set of spherical harmonic active shims are designed and explored for implementation within this gradient coil configuration. From there the design of a cylindrical radiofrequency coil using gradient design techniques is investigated as preliminary work towards implementing these low-frequency design techniques which have had success designing gradient coils towards the design of radiofrequency coils.

Finally, motivated by the complexity of the induced eddy currents in the surrounding conductive structures due to asymmetric gradient coils the final project explores the design of a multi-coil matrix array aimed at fitting within the compact gradient housing to dynamically compensate eddy currents during imaging.

This work ultimately demonstrates the feasibility of implementing an asymmetric shoulder cut-out gradient coil with rotated transverse gradient axes to enable neck imaging in a compact MRI scanner while providing potential solutions to handle the increased eddy current complexity associated with a setup such as this.

Keywords

Magnetic Resonance Imaging, Gradient Coil, Shim Coil, Radiofrequency Coil, Boundary Element Method, Stream Function, Eddy Current Compensation

Summary for Lay Audience

Magnetic resonance imaging (MRI) uses a series of nested electromagnets to produce anatomical images of the body. This thesis explores the design of three of these electromagnets: the gradient coil, the radiofrequency (RF) coil, and a set of shim coils. Many clinical MRI scans are performed of the head and as such development of “head-optimized” scanners have gained popularity. These are smaller than those used for full-body imaging and have limited patient entrance due to their small radius. In these systems the entrance into the MRI scanner is stopped by the shoulders limiting imaging to the brain region. This thesis asks the question “can we design an MRI gradient coil for compact head-optimized geometries which allows imaging of the cervical spine.”

The first chapter of this thesis goes into the necessary background information required to understand the work outlined here. The next two chapters in this thesis explore the design of a gradient coil with portions of the sides removed to accommodate the patient’s shoulders. This allows further entrance into the MRI scanner while maintaining geometries appropriate for a head-optimized system. This would allow the neck to slide into the region in the MRI scanner where the imaging takes places. I investigated the trade-offs in performance and propose designs which fit inside an experimental MRI scanner. This is extended in the fourth chapter by designing of a complimentary set of shim coils to improve imaging performance by dynamically shimming the MRI imaging environment. Radiofrequency coil design is explored in Chapter 5 where I design an RF coil using gradient coil design techniques, construct the coil and perform experimental validation. The constructed coil had field artefacts compared to the ideal design which I attribute to a violation of an assumption made in the design. Next, the sixth chapter investigates the design of a special type of coil to help improve imaging by actively compensating for eddy currents which produce parasitic magnetic fields of their own that degrade image quality. Finally, in Chapter 7 I summarize the work of the preceding chapters and outline some next steps to expand on this thesis.

Co-Authorship Statement

The following thesis contains work comprising:

Chapter 2 is an original research article which is an expansion of the peer-reviewed conference abstract: Eric J. Lessard, William B. Handler, and Blaine A. Chronik. *Preliminary Design Exploration for a Head and Neck Gradient Coil: Effect of Shoulder Cut-out Length on Performance*. International Society for Magnetic Resonance Imaging Annual Meeting 2019.

As first author of this work I was responsible for writing the entirety of the manuscript, performing design simulations, and performing analysis of all data. This included generation of all tables and figures. Drs Handler and Chronik were responsible for supervision and guidance on the work.

Chapter 3 is an original research article which is an expansion of the two peer-reviewed abstracts:

Eric J. Lessard, William B. Handler, and Blaine A. Chronik. *The X-Mode Gradient: Improved Performance for Select Applications*. International Society for Magnetic Resonance Imaging Annual Meeting 2020.

Eric J. Lessard, William B. Handler, and Blaine A. Chronik. *Development of an MRI Gradient Coil for Use in a Compact Head-only MRI Platform Capable of Imaging C7 and Below*. American Association of Physicists in Medicine and Canadian Organization of Medical Physicists Joint Annual Meeting 2020.

As first author of this work I was responsible for writing the entirety of the manuscript, performing design simulations, and performing analysis of all the data. This included generation of the tables and figures. Drs. Handler and Chronik were responsible for supervision and guidance of the work.

Chapter 4 is an original research article which is an expansion of the peer-reviewed abstract: Eric J. Lessard, William B. Handler, and Blaine A. Chronik. *Spherical Harmonic Active Shim Set Design for a Shoulder Cut-out MRI Platform*. International Society for Magnetic Resonance Imaging Annual Scientific Meeting 2022.

As first author of this work, I was responsible for writing the entirety of the manuscript, performing design simulations, and performing analysis of all the data. This included generation of the tables and figures. Drs Handler and Chronik were responsible for supervision and guidance of the work.

Chapter 5 is original research based on unpublished work titled: Eric J. Lessard, Kieffer J. Davieau, Diego F. Martinez, Colin Metrow, William B. Handler, and Blaine A. Chronik. *A 21 MHz RF Coil Designed Using a Boundary Element Method: Theoretical Design, Experimental Results, and Next Steps.*

As first author I was responsible for the writing the entirety of the manuscript, performing the design simulations, performing data analysis, construction of the coil, and measurement of the magnetic fields. Kieffer Davieau assisted with coil construction, measurements and constructed the matching circuit. Diego Martinez assisted with coil construction, measurements and contributed to the data import pipeline. Colin Metrow performed preliminary design simulations and full-wave simulations as part of his MSc project. Although, none of these results were included here it is important to note the early contributions of his to this project. Dr. Handler performed the full-wave simulations for the work presented here while providing supervision and guidance. Dr. Chronik provided supervision and guidance. Although not included as an author, Brian Dalrymple performed the CNC routing of the coils.

Chapter 6 is original research based on unpublished work titled Eric J. Lessard, William B. Handler, and Blaine A. Chronik. *Dynamic Eddy Current Compensation and Spherical Harmonic Shimming using a Matrix Array Coil.*

As first author I was responsible for conception of the original idea, writing the manuscript, performing data analysis and writing of the code to generate multi-coil arrays of various configurations. Drs Handler and Chronik provided supervision and guidance. Although not included as authors, Drs Bindseil and Harris provided experimental results and previously derived wire patterns for the shim coils. They also provided guidance and feedback on the work at various stages.

It should also be explicitly mentioned that the design methods used in this thesis are implemented using in-house MATLAB code which has been contributed to by past and present

generations of graduate students in the xMR lab. As part of code migrations and the research outlined in this thesis, I have played a role in modification and extension of this code base however, none of that would be possible without the significant contributions of those who have contributed.

Dedication

To Amanda,

for your unwavering love and support.

Acknowledgments

First, I would like to acknowledge my supervisor Dr. Blaine Chronik for providing me with the opportunity to pursue independent research and building the strong research environment in which I was lucky to be a part of. To the members of my advisory committee, Drs. Andrea Soddu, Ravi Menon, and Jean Theberge who have taken time to provide insight and support on my work, I appreciate everyone sharing their expertise with me and guiding me throughout my PhD.

To Dr. Will Handler, to list the amount of support you have provided me throughout my degree would leave no room for others to be included. In the interest of brevity, I am happy to have had you as my best-man at my kitchen wedding. I truly cannot overstate the contributions you've had towards my academic and personal development. To Drs. Geron Bindseil and Chad Harris for taking an active role in the development of my research projects over my time here, your feedback has been invaluable, and I truly appreciate you both taking the time to help and share your wealth of knowledge related to everything MR. I have been lucky to have the support of excellent research and technical staff throughout my degree and without the constant assistance and guidance from Frank Van Sas, Brian Dalrymple, Ryan Chaddock, and Colin McCurdy much of this work would have not been possible. From sharing practical advice, aiding with projects, and just being wonderful to chat with. Each of you have had your own meaningful impact throughout my time with the lab. To the other students in the xMR Labs Amgad Louka, Kieffer Davieau, Arjama Halder, Diego Martinez, Colin Metrow, Matt McCready, and John Adams each of you have made working together in 314 a pleasure in your own special ways.

To my family for supporting and encouraging me throughout the entirety of my academic training and finally, to my fiancé Amanda for always being by my side.

Table of Contents

Abstract.....	i
Summary for Lay Audience.....	iii
Co-Authorship Statement.....	iv
Dedication.....	vii
Acknowledgments.....	viii
Table of Contents.....	ix
List of Tables.....	xiii
List of Figures.....	xiv
List of Appendices.....	xvi
List of Abbreviations.....	xvii
Chapter 1.....	1
1 Introduction.....	1
1.1 The Physics of Magnetic Resonance Imaging.....	2
1.1.1 The Importance of Field Homogeneity.....	4
1.2 MRI Electromagnets.....	9
1.2.1 Main Magnet.....	9
1.2.2 RF Coils.....	12
1.2.3 Shim and Gradient Coils.....	13
1.2.4 Symmetric vs Asymmetric Head Gradient Coils.....	19
1.3 Matrix Coil Arrays.....	21
1.4 Quasistatic Electromagnet Design Methods.....	21
1.4.1 Quasistatic Magnetic Fields.....	21
1.4.2 Boundary Element Method.....	22
1.4.3 Performance Functional.....	24

1.4.4	Low vs. High Field	26
1.4.5	Point-of-Care MRI	26
1.4.6	Current Implementations	27
1.5	Thesis Overview	28
1.6	References	29
Chapter 2	33
2	Investigation of a Shoulder Cut-out MRI Gradient Coil.....	33
2.1	Introduction.....	33
2.2	Methods.....	35
2.3	Results.....	40
2.4	Discussion	42
2.5	Conclusion	51
2.6	References.....	51
Chapter 3	53
3	The X-Mode Gradient Coil Configuration.....	53
3.1	Introduction.....	53
3.2	Methods.....	55
3.2.1	Design Methods	55
3.2.2	Analysis.....	59
3.3	Results.....	60
3.4	Discussion	60
3.5	Conclusion	70
3.6	References.....	70
Chapter 4	72
4	Shoulder Cut-out Active Shim Set Design.....	72
4.1	Introduction.....	72

4.2	Methods.....	74
4.2.1	Design Methods	74
4.2.2	Eddy Current Analysis.....	77
4.3	Results.....	78
4.4	Discussion.....	78
4.5	Conclusion	86
4.6	References.....	86
Chapter 5.....		88
5	Design, Construction and Verification of 21MHz Radiofrequency Coil.....	88
5.1	Introduction.....	88
5.2	Methods.....	90
5.2.1	Computational Methods.....	90
5.2.2	Construction Methods.....	92
5.2.3	Field Measurements	92
5.2.4	Full-Wave Simulations	92
5.3	Results.....	93
5.4	Discussion.....	93
5.5	Conclusion	100
5.6	References.....	100
Chapter 6.....		103
6	Dynamic Eddy Current Compensation using a Matrix Array.....	103
6.1	Introduction.....	103
6.2	Methods.....	104
6.2.1	Theory	104
6.2.2	Design Methods	106
6.2.3	Spherical Harmonic Field profiles	107

6.2.4 Eddy Current Analysis	107
6.2.5 Power and Energy Analysis	108
6.3 Results	108
6.4 Discussion	109
6.5 References	118
Chapter 7	120
7 Thesis Conclusions and Future Directions	120
7.1 Overview and Research Questions	120
7.2 Summary and Conclusions	121
7.3 Limitations	123
7.4 Future Directions	123
7.4.1 Computational	124
7.4.2 Construction and Verification	124
7.5 Significance and Impact	125
Appendices	127
Appendix A: Stream Function Performance Functional	127
A.1 Creation of a Performance Functional	127
A.2 Calculating Magnetic Field	127
A.3 Calculating Power	129
A.4 Incorporating Shielding	130
A.5 Incorporating Torque	132
A.6 From Functional to Wire Pattern	133
A.7 References	135
Appendix B: Designing MRI Gradient Coils using Surface Eigenmodes	136
Curriculum Vitae	143

List of Tables

Table 1-1: List of Spherical Harmonic Electromagnets	14
Table 2-1: Selected Gradient Coil Performance Parameters	42
Table 2-2: Selected Gradient Coils Merit Values	46
Table 3-1: X-Mode Gradient Performance Parameters	61
Table 4-1: Example Shim Performance Parameters	80
Table 5-1: Larmor Frequency for Various Nuclei	88
Table 6-1: Multi-Coil Single Loop Inductance and Resistance	109
Table 6-2: Dynamic Eddy Current Compensation Field Reduction	114
Table B-1: Full vs Partial Eigenmode Solution Performance Parameters	140

List of Figures

Figure 1-1: Helmholtz Coil and Line Profile	11
Figure 1-2: Halbach Array Configuration.....	12
Figure 1-3: Bird Cage RF Coil Configuration	13
Figure 1-4: Magnetostimulation Operational Curve.....	17
Figure 1-5: Traditional Transverse Gradient Configurations	18
Figure 1-6: Symmetric and Asymmetric Gradient Configurations.....	20
Figure 1-7: Meshed Surface and Element.....	23
Figure 1-8: Example computational mesh, solved stream function and resultant wire pattern	26
Figure 2-1: Shoulder Cut-out Computational Mesh and Cartoon Illustration	36
Figure 2-2: Representative Shoulder Cut-out Gradient Wire Patterns	41
Figure 2-3: Effect of Adding Cut-out Surface	43
Figure 2-4: Effect of Moving Imaging Region	44
Figure 2-5: Selected Gradient Coil Homogeneity Plots	48
Figure 3-1: d_1 - and d_2 -gradient axes	56
Figure 3-2: X-Mode Computational Mesh	58
Figure 3-3: X-Mode Gradient Wire Patterns	62
Figure 3-4: X-Mode Gradient Coil Homogeneity Plots	64
Figure 3-5: X-Mode Gradient Field Plots.....	66
Figure 3-6: Inner Wire Cooling Analysis	67

Figure 3-7: X-Mode Gradient Eddy Current Analysis	68
Figure 4-1: Example Shim Wire Patterns	79
Figure 4-2: Shim Eddy Current Compensation	81
Figure 4-3: Shim Eddy Current Decomposition	82
Figure 4-4: Sample Eddy Current Field Coils	84
Figure 5-1: Performance Parameters vs Beta Value	94
Figure 5-2: RF Coil Wire Patterns	95
Figure 5-3: Simulated Field at [0,0,0] vs Time.....	96
Figure 5-4: Magnetic Field Plots	97
Figure 5-5: RF Coil Construction Photos	99
Figure 6-1: Multi-Coil Wire Patterns.....	109
Figure 6-2: Multi-Coil Static Eddy Current Compensation.....	110
Figure 6-3: Generating Spherical Harmonic Fields	111
Figure 6-4: Dynamic Eddy Current Compensation	112
Figure 6-5: Dynamic Eddy Current Compensation Power and Energy Plots.....	116
Figure A-1: Cylindrical Mesh, Stream Function, and Transverse Gradient Wire Pattern....	135
Figure B-1: Example Cylindrical Eigenmodes	138
Figure B-2: Full vs Partial Eigenmode Solution Example.....	139
Figure B-3: Higher Order Eigenmode Spatial Variation	141
Figure B-4: Example Eigenmode Frequency Analysis.....	142

List of Appendices

Appendix A: Stream Function Performance Functional.....	126
Appendix B: Designing MRI Gradient Coils using Surface Eigenmodes.....	135

List of Abbreviations

^1H	Hydrogen
^{19}F	Fluorine-19
^{129}Xe	Xenon-129
^3He	Helium-3
B_1^-	Radiofrequency Receive Field
B_1^+	Radiofrequency Transmit Field
BEM	Boundary Element Method
CT	Computed Tomography
DSV	Diameter Spherical Volume
DSV ₂₀	Diameter Spherical Volume with <20% Deviation
DSV ₃₀	Diameter Spherical Volume with <30% Deviation
DSV ₅₀	Diameter Spherical Volume with <50% Deviation
H_{\min}	Minimum Homogeneity
ID	Inner Diameter
IR_{offset}	Imaging Region Offset
MR	Magnetic Resonance
MRI	Magnetic Resonance Imaging
OD	Outer Diameter
RF	Radiofrequency

SCO	Shoulder Cut-out
T1	Longitudinal Relaxation Constant
T2	Irreversible Transverse Relaxation Constant
T2'	Reversible Transverse Relaxation Constant
T2*	Apparent Transverse Relaxation Constant
W_{\min}	Minimum Wire Spacing

Chapter 1

1 Introduction

Diagnostic imaging has found a critically important role in healthcare ranging from emergency room imaging to image guidance for irradiation. Magnetic resonance imaging (MRI) plays an important role across this entire range with its excellent soft tissue contrast and ability to provide a variety of complimentary information without the use of ionizing radiation. This has also motivated the design of head-optimized scanners which provide anatomical target delineation and functional information which is useful in treatment planning and patient triaging. Although the work presented in this thesis is applicable for a range of MR applications and environments the focus has been on the implementation of these designs within low-field head-optimized platforms currently implemented for point-of-care imaging. In systems such as these their head-optimized geometry leads to small internal radii limiting the room for the various subsystem components, which will be discussed within this introduction. This presents design and engineering challenges which must be overcome for implementation, a theme which will be maintained throughout the following chapters.

The low-field nature of these systems, the physics of which leads to a lower intrinsic MR signal, may be compensated for by using high-performance subsystems to maintain diagnostic quality imaging (1, 2). Much work has been performed exploring point-of-care low-field MR platforms with low-power requirements which can be implemented closer to the patient environment. These don't have the requirement of a separate equipment room for high-power electrical equipment. In this work I focused on the design of a complementary point-of-care platform with high-power, high-performance components. This choice will dictate some of the design decisions that are made throughout this thesis and will impact the final presented electromagnetic designs.

A traditional MRI machine is a complex set of electromagnets paired with high powered amplifiers, electromagnetic shielding, and a variety of other components which allow the

MR technologist to interact with and run the MRI scanner. This thesis is focused on the exploration and design of three types of electromagnets used in MR.

1.1 The Physics of Magnetic Resonance Imaging

MRI makes use of the physical phenomenon known as nuclear resonance in which nuclei are perturbed by the presence of a magnetic field. A full detailed treatment of the physical phenomenon that leads to image formation is out of the scope of this thesis. However, a brief introduction will be presented here to provide the necessary background information required to properly understand the following chapters.

Clinical MRI is primarily concerned with measuring signal from hydrogen nuclei within the body which is then used to formulate images of tissue. However, the MRI signal can be extended to any atom with a non-zero nuclear spin angular momentum. Classically, these nuclei can be thought of as magnetic moments arising due to the spinning of charged particles. Magnetic moments within a sample or patient will interact when exposed to magnetic fields. At thermal equilibrium these magnetic moments will be randomly oriented throughout the sample and no significant net magnetization is observable. In the presence of an external magnetic field a small net magnetization will exist parallel, or anti-parallel, to the external magnetic field. Although a small proportion of spins will align with the magnetic field ($\sim 10^{-6}$) in a small sample there exists on the order of Avogadro's number of spins ($\sim 10^{23}$) and this will still result in a large detectible magnetization. At thermal equilibrium the net magnetization is proportional as follows:

$$M = \frac{\gamma^2 h^2 N_s B_0}{4kT} \quad (1.1)$$

Where γ is the gyromagnetic ratio, h is Planck's constant, N_s is the number of spins, B_0 is the applied magnetic field strength, k is the Boltzmann constant, and T is the absolute temperature.

Within this magnetic field the net magnetization will also begin to precess about the direction of the polarizing field. The frequency of this precession is proportional to the magnetic field as follows:

$$f = \frac{\gamma}{2\pi} B_0 \quad (1.2)$$

This frequency, called the Larmor frequency directly depends on γ (gyromagnetic ratio) and B_0 (applied magnetic field strength). From these equations we can see two important things: 1) a large applied magnetic field will increase the strength of the magnetization and 2) if a spatially dependent magnetic field is applied the spins will have a positionally dependent frequency and phase information. In an MR experiment the first aspect is handled by the main magnet which produces a strong static single-valued uniform magnetic field over an imaging region causing spins in that region to precess about it at a known frequency. The second is accomplished using gradient coils which are high-powered electromagnets which produce linearly varying magnetic field values along the three cartesian axes. This causes the nuclei to precess at a different frequency depending on their spatial location. With the frequency and phase of the net magnetization containing spatially dependent information one can take measurements of this information and form an image using the inverse Fourier transform.

However, to make a measurement of this frequency and phase information the system must first be perturbed from its equilibrium. A transmit radiofrequency (RF) coil is used to produce a magnetic field perpendicular to the main magnetic field. This results in a torque on the magnetization vector causing it to tip into the transverse plane. The duration and strength of this transmit field (B_1^+) determines the angle at which the magnetization is tipped from the longitudinal axis (Z) towards the transverse (XY) plane. For maximum energy transfer this B_1^+ field is applied using a circularly polarized magnetic field tuned to the Larmor frequency. When the radiofrequency field is turned off the magnetization begins to realign (relax) along the longitudinal axis and decay in the transverse plane with timing governed by three time-constants. These are longitudinal relaxation (T1), reversible transverse relaxation (T2'), and irreversible transverse relaxation (T2). T1 describes the interaction of the spins and their environment and cannot be reversed with applied RF pulses, it is the longest of the constants and is the recovery of the magnetization along the longitudinal axis. T2' is the result of magnetic field inhomogeneities and describes the transverse plane dephasing which can be reversed using an RF pulse. T2 is dephasing due

to the spin-spin interactions. It is standard for T2' and T2 to be described by a combined metric T2*.

This changing magnetic field will induce a voltage in the nearby radiofrequency coil which is measured as the received signal. This voltage signal is governed by the principle of reciprocity.

$$V_s = -\frac{d}{dt} \int_{\text{Sample}} [\vec{M}(\vec{r}, t) \cdot \vec{B}_1^-(\vec{r})] dV \quad (1.3)$$

From this we can see that the signal is proportional to the sum net sample magnetization weighted by the sensitivity profile of the receive coil (B_1^-). The signal will then be weighted by the density of protons in the sample which allows formation of proton-density images as well as the various time constants (T1, T2, T2*) which govern the magnetization dynamics. Through specific timing of the electromagnets controlling the electromagnetic environment it is possible to change the weighting of the signal between proton density and specific time constants. This weighting of the signal by the tissue time constants will provide contrast between tissues and enable various tissue weightings to be performed by modifying the timing. Advanced techniques allow weighting based on flow and diffusion of fluid within the imaging volume are performed in similar ways.

1.1.1 The Importance of Field Homogeneity

From the above it is clear the MRI needs to have fine control over the magnetic field environment. During an imaging sequence it is ideal that the gradient fields produce the only known deviation in the measured frequency of the signal.

For example, when an x-gradient is applied the nuclei will accrue a positional dependent phase as:

$$B(\mathbf{r}) = B_0 + xG_x \quad (1.4)$$

$$\Phi_{total}(\mathbf{r}) = \gamma(x \int_0^t G_x d\tau) = \Phi_{grad}(\mathbf{r}) \quad (1.5)$$

However, in the case where the B_0 field contains local field inhomogeneities characterized by $\Delta B_0(\mathbf{r})$ then the total phase accrued will no longer be solely proportional to the applied gradient field.

$$B(\mathbf{r}) = B_0 + xG_x(\mathbf{r}) + \Delta B_0(\mathbf{r}) \quad (1.6)$$

$$\begin{aligned} \Phi_{total}(\mathbf{r}) &= \gamma(x \int_0^t G_x d\tau + \int_0^t \Delta B_0(\mathbf{r}) d\tau) \\ &= \Phi_{grad}(\mathbf{r}) + \Phi_{\Delta B_0}(\mathbf{r}) \end{aligned} \quad (1.7)$$

Therefore, since the phase information is used in the formation of the image the magnetic field environment must be homogeneous for image reconstruction to be geometrically accurate. In practice this is not the case and the total phase accrued will be affected by various static and time varying field inhomogeneities such as imperfections in the MR system, macroscopic field variations resulting from the MR sample, and induced eddy currents in conducting surfaces within the MR environment.

1.1.1.1 System Imperfections

Although much effort is employed to prevent errors during the design and manufacturing process of an MR system there will always exist small deviations from the ideal design calculations and the final installed scanner at a site. These deviations are a result of physics simplifications, machining, and human tolerances during construction and even the local magnetic environment at the installation site. These field inhomogeneities are static in nature and can be overcome in post-processing or through static shimming at the installation site. Static shimming is the process of adding magnetic materials to the surrounding environment in a particular way such that the field inhomogeneities induced by the local environment are corrected for by the presence of these magnetic materials.

These are installed during commissioning in an iterative process in which field error measurements are made, corrected for using a shimming algorithm placing magnetic materials at strategic locations and repeated until the field inhomogeneity is below acceptable limits. Acceptable limits are typically on the order of ppm and are application dependent with routine imaging having the most lenient requirements and techniques such as magnetic resonance spectroscopy having stricter requirements. These ferromagnetic materials are often installed within the gradient housing which limits radial space to accommodate the tubing in which they are installed. This process is done during MR commissioning and is not repeated unless major structural modifications are made such that the MR environment has significantly been changed.

1.1.1.2 Sample Induced Field Variations

Differences in tissue magnetic susceptibility will lead to variations in the magnetic field causing macroscopic field inhomogeneities. This is most noticeable in areas such as the lung or sinuses where air tissue interfaces are large and/or plentiful. Arising from differences in magnetic susceptibilities these are static inhomogeneities which vary from patient to patient and from sample to sample. Therefore, static shimming methods cannot be employed as the variations are unpredictable in nature. Instead, active shim coils are used which create spherical harmonic field profiles over the imaging region and are used to correct for these inhomogeneities prior to imaging. These electromagnets will be discussed in further detail later in the chapter.

Fluctuations can be induced through normal physiological variations such as patient movement during breathing, or flow of fluids throughout the body. Motion of the chest wall during a normal breathing cycle will result in spatial and temporal variations in the magnetic environment. Hardware timing techniques such as respiratory gating and dynamic updating of the resistive shims during the respiratory cycle are two example methods of handling physiological motion inhomogeneities.

1.1.1.3 Eddy Currents

As per Faraday's Law of Induction and Lenz's Law, conducting material in the presence of a changing magnetic field will have counter currents induced. These induced currents

will create their own time varying magnetic fields which in MR imaging are parasitic in nature, as they degrade image quality. As well, they will result in heating of the conducting material in the form of Joule Heating. The heating of components can be detrimental due to temperature dependent magnetic field shifts as well as the potential for a quench (loss of superconducting status). As MRI utilizes changing magnetic fields for image formation this is a physical problem that cannot be entirely avoided but can be minimized using either hardware modifications or post-processing image algorithms. The primary source of eddy current generation in an MR experiment is the changing gradient field as their frequency combined with the electromagnetic properties of the surrounding housing and coils result in the formation of relatively long-lived eddy currents (50 – 400 ms). A common hardware method of handling eddy currents is implementing actively shielded gradient coils with a second, larger radii electromagnet run in series with the gradient coil designed to minimize the stray magnetic field outside of the gradient coil structure. These actively shielded systems have enjoyed great success, as the majority of gradient coils operating today employ this solution. However, there is a trade-off in the design as the shielding will negatively impact the basic performance of the gradient by decreasing the speed at which it can be switched and lowering the gradient efficiency due to the extra current carrying wire which is run in series. A common method of handling induced eddy currents outside of hardware modifications is through the use of gradient pre-emphasis where the gradient waveform is modified to account for the induced eddy currents in the pulse sequence.

In a point-of-care environment eddy currents can pose an even larger threat. In a cryogen free system, the main magnet is often more susceptible to quenching as the windings are not submerged in cryogenic liquid. In a cryogen system, this will lead to boil-off of the cryogen but has more tolerance for quenching. Depending on the gradient shielding there runs the risk of inducing eddy currents in components not part of the MR system such as intensive care equipment. This makes proper shielding important when the room in which the MR is employed is multipurpose.

1.1.1.4 Spherical Harmonic Representation of the Magnetic Field

Within the imaging region there is an absence of internal sources allowing Maxwell's Equations to be conveniently reduced to decoupled equations as follows:

$$\nabla \cdot \mathbf{E} = \mathbf{0} \quad (1.8)$$

$$\nabla \times \mathbf{E} = \mathbf{0} \quad (1.9)$$

$$\nabla \cdot \mathbf{B} = \mathbf{0} \quad (1.10)$$

$$\nabla \times \mathbf{B} = \mathbf{0} \quad (1.11)$$

Considering only the equations for the magnetic fields Equation 1.10 and Equation 1.11 and the following vector relationship:

$$\nabla \times \nabla \times \mathbf{B} = \nabla(\nabla \cdot \mathbf{B}) - \nabla^2 \mathbf{B} \quad (1.12)$$

We can arrive at the familiar Laplace's equation and if we consider only the z-component of the magnetic field we have a simplified equation with its solution of a linear combination of spherical harmonic functions:

$$\nabla^2 B_z = 0 \quad (1.13)$$

$$B_z(r) = \sum_{n=0}^{\infty} \sum_{m=-n}^n C_n^m r^n P_n^m(\cos \theta) e^{im\vartheta} \quad (1.14)$$

This is the principle behind field inhomogeneity corrections, by performing a field map and decomposing the magnetic field into its spherical harmonic components as follows:

$$B_z(r) = B_0 + \frac{dB_z}{dx} + \frac{dB_z}{dy} + \frac{dB_z}{dz} + \frac{dB_z}{dxy} + \frac{dB_z}{dzy} + \frac{dB_z}{dz^2} + \frac{dB_z}{d(x^2 - y^2)} \quad (1.15)$$

The above equation, expanded to second order, describes the B_z component of the magnetic field in terms of our desired field value B_0 and the distortion of the magnetic field in three linear directions and distortion in five 2nd order directions. By using MR electromagnets to produce a set of spherical harmonics and fields with the same size and opposite magnitude of the measured spherical harmonic field decomposition the fields are superimposed and

the inhomogeneities are corrected. This process is referred to as active shimming of the magnetic field. This is performed during the imaging process and is sample dependent.

1.2 MRI Electromagnets

MRI relies on the formation of known magnetic fields such that the nuclei of interest can be perturbed in a known way. The timing and strength of these magnetic fields is outlined by a timing document known as a pulse sequence. This is played out by the MRI equipment using controllers, amplifiers, and a series of electromagnets. The electromagnets which comprise a typical clinical MRI scanner are: the main magnet, the radiofrequency (RF) coils, the shim coils, and the gradient coils.

An electromagnet, the design of which will be outlined in more detail later in this chapter, is made using conductive wire wound in a known pattern that when current is run through it will produce a desired electromagnetic field profile. Throughout this thesis I will be concerned only with the magnetic field produced, unless otherwise mentioned.

A brief description of each, as well as configurations used in the research setting, that are relevant to this thesis will be given below.

1.2.1 Main Magnet

The main magnet (denoted as B_0) within an MRI system is designed such that over the imaging region (typically 20-25 cm for head-only systems and 50 cm for whole body systems) the magnetic field is homogeneous. Essentially, this means that the B_z component of this field is equal to the manufacturer specified field strength at each spatial location within this imaging region. Main magnet construction typically falls into one of three categories: 1) cryogen cooled magnets where the magnet windings are submersed in liquid helium, 2) cryogen free magnets where the magnet windings are housed within a vacuum, and 3) permanent magnets where the magnetic field is achieved through use of a system of permanent magnets.

While traditional clinical and research MRI scanners have historically employed cryogenically cooled magnets with submerged windings these come with an increased

complexity and cooling requirements which make them more difficult for acute and focused settings. Cryogen free systems, however, have fewer siting requirements including not needing additional ventilation for liquid helium ventilation in the case of a quench. Lastly, permanent magnet systems require no cryogenic ventilation but are limited in their field strength, shape and orientation when compared to electromagnet produced fields.

The simplest method of producing a homogeneous magnetic field over the imaging region is using a Helmholtz Pair in which a circular pair of electromagnets are placed a distance equal to their radius apart. This produces a homogeneous magnetic field proportional to the winding density and inversely proportional to the radius. Modern systems require active shielding and have stricter homogeneity requirements and therefore use modified configurations based on this principle in which more coils are strategically added. They also implement shielding windings to ensure the stray field is reduced. Figure 1-1 shows an example Helmholtz configuration for a single loop of wire with a radius of 0.20 m and its corresponding magnetic field profile across the line $[0,0, z]$. From this it can be seen that within a 0.12 m segment the field is within 1% of the central field value and within 6% at the tips of the coils.

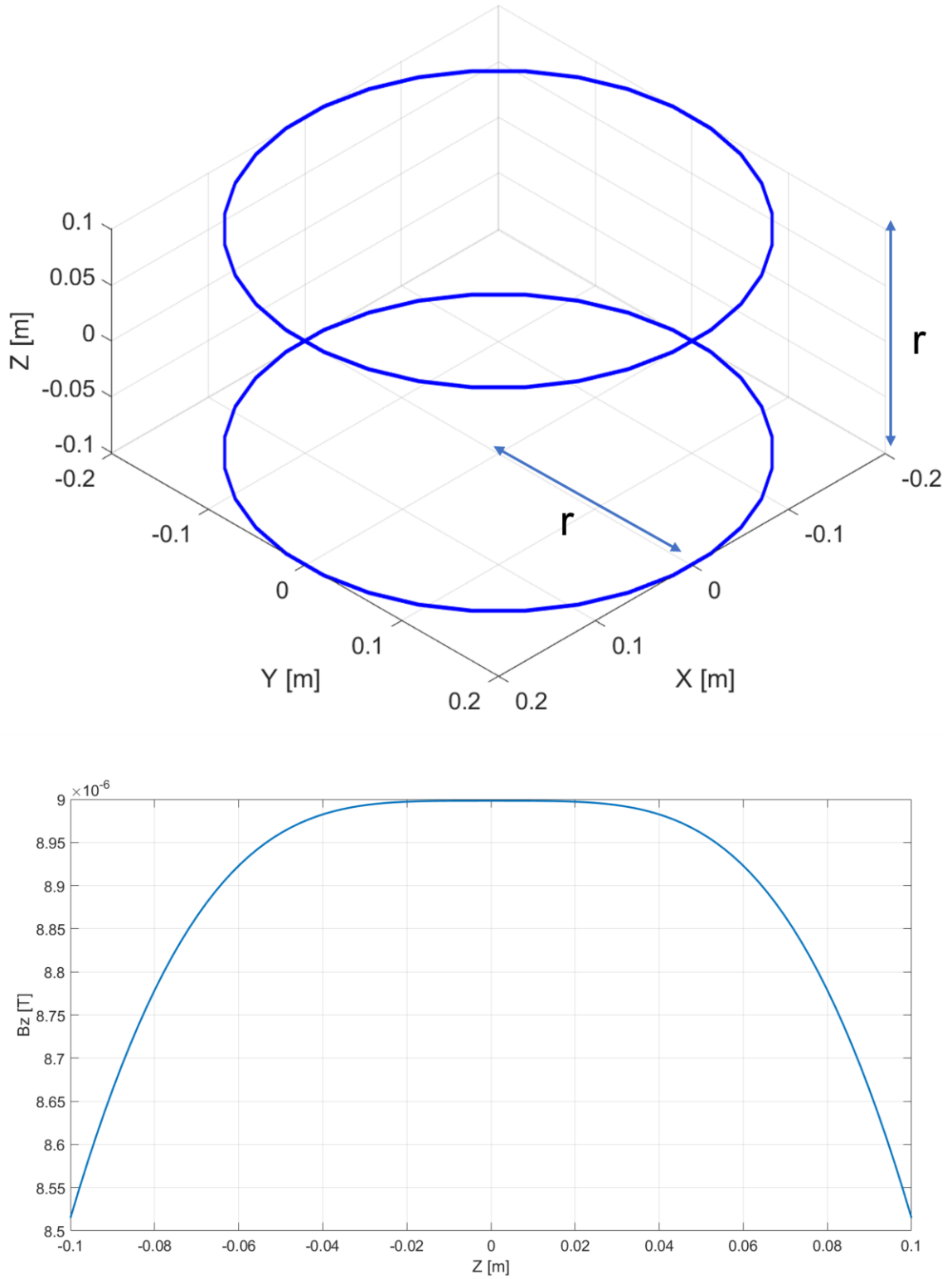


Figure 1-1: Helmholtz Coil and Line Profile

Example wire configuration and resultant field profile for a standard Helmholtz coil. Colour indicates current direction. In a Helmholtz coil each coil carries equal current in the same direction and the coils are spaced a distance of r apart where r is the coil radius.

Modern point-of-care permanent magnetic configurations often use Halbach Array style magnet configurations (3–5) which result in a homogeneous main magnetic field perpendicular to the traditional Z direction that a wound magnet provides.

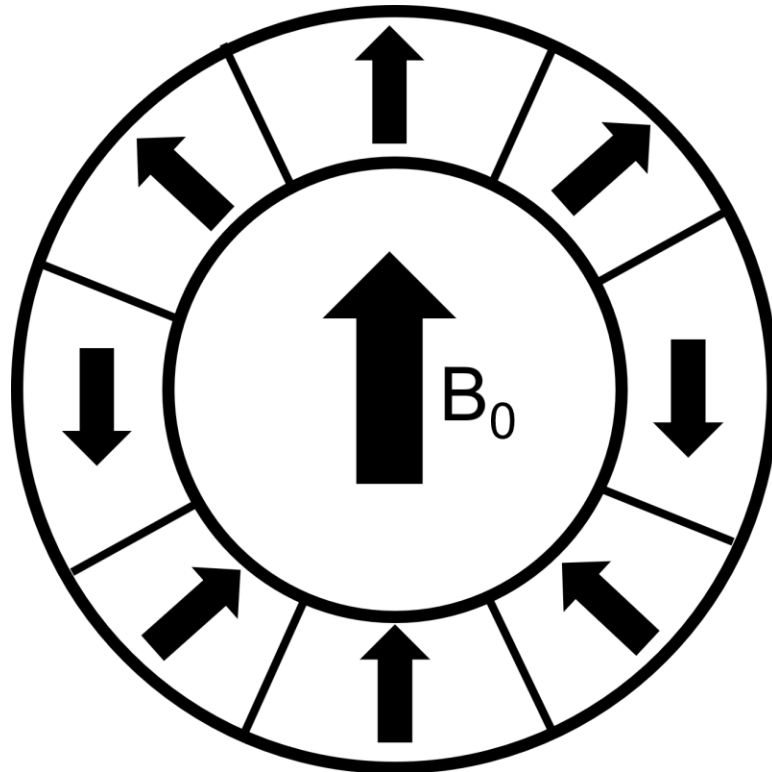


Figure 1-2: Halbach Array Configuration

Standard Halbach array configuration showing the polarization direction of the magnets circling the imaging region. This configuration creates a homogeneous magnetic field perpendicular to the cylinder axis.

1.2.2 RF Coils

The RF coils are responsible for perturbing the sample within the MRI system through the use of the transmit (B_1^+) fields and for measuring the sample signal (B_1^-) fields. This can be done either by using a single transmit/receive coil with a switch to change modes during the imaging sequence or using two separate coils one for transmitting and another for receiving. Bird cage style coils are the most popular style coil for their high homogeneity and strong magnetic field (6, 7). They consist of two circular end-rings connected by an

even number of rungs. Capacitors are distributed strategically throughout the coil such that the rungs are run out of phase with each other and create a circularly polarized magnetic field at the center. When driven using two input ports shifted in phase this produces the circularly polarized field however by using a single driven port it is possible to produce a linearly polarized field profile. To achieve maximum energy transfer to the imaging environment a circularly polarized field is preferred. The produced magnetic field from an RF coil is on the order of μT .

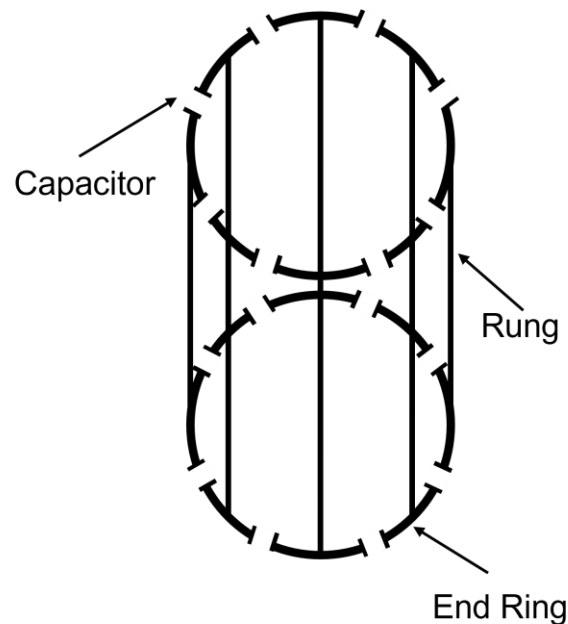


Figure 1-3: Bird Cage RF Coil Configuration

Bird cage style RF coil configuration with distributed capacitors on the end rings. Shown capacitor distribution creates a high-pass bird cage coil.

Receive arrays are sets of loops of wire each with their own sensitivity profile. The multiple channels are read simultaneously and used to reconstruct the image using their respective profiles. This provides high SNR and can enable accelerated imaging techniques by using the redundancy in the imaging profiles.

1.2.3 Shim and Gradient Coils

Gradient and shim coils are both designed in similar electromagnets but differ in their construction and use. Both sets are designed to produce spherical harmonics over the

imaging region. A list of spherical harmonics and their respective order and function are given in Table 1-1. First order spherical harmonic generating electromagnets are referred to as gradient coils. These produce magnetic fields which vary linearly across the three cartesian axes. Higher order spherical harmonic generating electromagnets are referred to as shim coils. These produce magnetic fields which vary across higher order axes as previously mentioned. Traditionally, shim coils are unshielded low power electromagnets run using small amplifiers. They are used for correcting inhomogeneities in the main magnetic field on a patient-by-patient and often slice-by-slice basis. Each individual coil is designed such that they produce a higher order spherical harmonic field profile over the imaging region. Clinical scanners often implement up to 2nd order shim coils with research settings utilizing higher orders. Gradient coils typically have field strengths on the order of 10s of mT whereas shim coils operate with fields closer to 10 μ T and both produce fields that vary as a function of position.

Table 1-1: List of Spherical Harmonic Electromagnets

	Name	n	m	Function
Gradient Coils	Z	1	0	z
	X	1	1	x
	Y	1	-1	y
Shim Coils	Z^2	2	0	$z^2 - (x^2 + y^2)/2$
	ZX	2	1	$3zx$
	ZY	2	-1	$3zy$
	X^2-Y^2	2	2	$3(x^2 + y^2)$
	XY	2	-2	$6xy$

First and second order (n) spherical harmonic functions. Each order has 2n+1 functions. First order generating electromagnets create linear variations in the magnetic field and are referred to as gradient coils. Second order generating electromagnets create higher order variations in the magnetic field and are referred to as shim coils.

Although the shim coils are often static during an imaging sequence dynamic shimming has been employed on a slice-by-slice basis using spherical harmonic active shims as well as matrix arrays of independently driven current loops. This has found promise at higher fields where field homogeneity has a larger impact on imaging performance. In addition to being employed to shim the main magnetic field, higher order shims can be used to compensate for more complex eddy currents induced by the gradient coils during operation. This is important when gradient coils move away from symmetrical designs (such as that found in a full-body clinical scanner) towards asymmetric designs. These designs are often found in head-only systems where the imaging region is not located at the geometric center of the gradient coil but instead is shifted towards the patient end. In systems such as these the induced eddy current in the surrounding conducting surfaces is more complex than in the symmetric case.

Gradient coils are traditionally shielded high-powered electromagnets which use strong current amplifiers to produce fields which are switched on and off during an imaging sequence to induce known frequency and phase information to the nuclei of interest. This information is used for spatial localization and advanced imaging techniques such as diffusion tensor imaging. The history of gradient coils can be traced back to 1958 when Marchel Golay introduced an electromagnet geometry now referred to as a “Golay Coil” which was intended to reduce field inhomogeneities for NMR experiments (8). Even though the Golay Coil was designed to provide shimming to NMR experiments it formed the basis for the eventual large-scale gradient coil. Peter Mansfield in his 1977 seminal paper proposed the usage of time dependent magnet field gradients to form two- or three-dimensional spin density images (9).

Performance of the gradient is not governed by the electromagnet alone and is dependent on the selection of amplifier to use with the coil. It is common to characterize gradient (and shim) coil performance in terms of maximum gradient field, defined as the maximum gradient field the coil can produce and slew-rate, which is a measure of how fast the electromagnet can change in field (10–12). This can also be written as rise-time which is the time it takes to reach the maximum magnetic field. This is not necessarily the maximum magnetic field possible by the electromagnet but the max field desired.

During the design process the winding density will play a role in the electromagnet efficiency which is the magnetic field produced per unit current defined as follows:

$$G = \eta I \quad (1.16)$$

Where G is the field gradient [mT/m], η is the gradient efficiency [mT/m/A], and I is the current flowing through the coil. This allows characterizing the maximum gradient field and slew rate as follows:

$$G_{max} = \eta I_{max} \quad (1.17)$$

$$SR = \eta \left(\frac{V - RI}{L} \right) \quad (1.18)$$

Where G_{max} is the maximum gradient strength the gradient coil axis can provide, η is the gradient efficiency, and I_{max} is the maximum current that can be output from the amplifier. SR is the slew rate of the gradient coil [T/m/s], V is the voltage of the amplifier, I is the current running through the gradient coil, and L and R are the inductance and resistance of the gradient coil, respectively. Early gradient coils had typical field gradients on the order of 1 mT/m with a slew rate of 1 T/m/s. For comparison, research setting gradient coils today can reach 200 mT/m at slew rates of up to 500 T/m/s (13, 14). In the clinic these values are typically lower with whole body gradients reaching 50 mT/m at slew rates of 200 T/m/s and head-gradients having higher average values due to their smaller radius.

This high switching speed can interact with the nervous system of a patient and produce peripheral nerve stimulation. Although not typically a major safety consideration limits are placed on operation of gradient coils to certain G_{max} and SR values based on experimental testing of each gradient coil configuration. This is another practical limitation when running a gradient coil and is an active area of research as gradient coils push their performance boundaries.

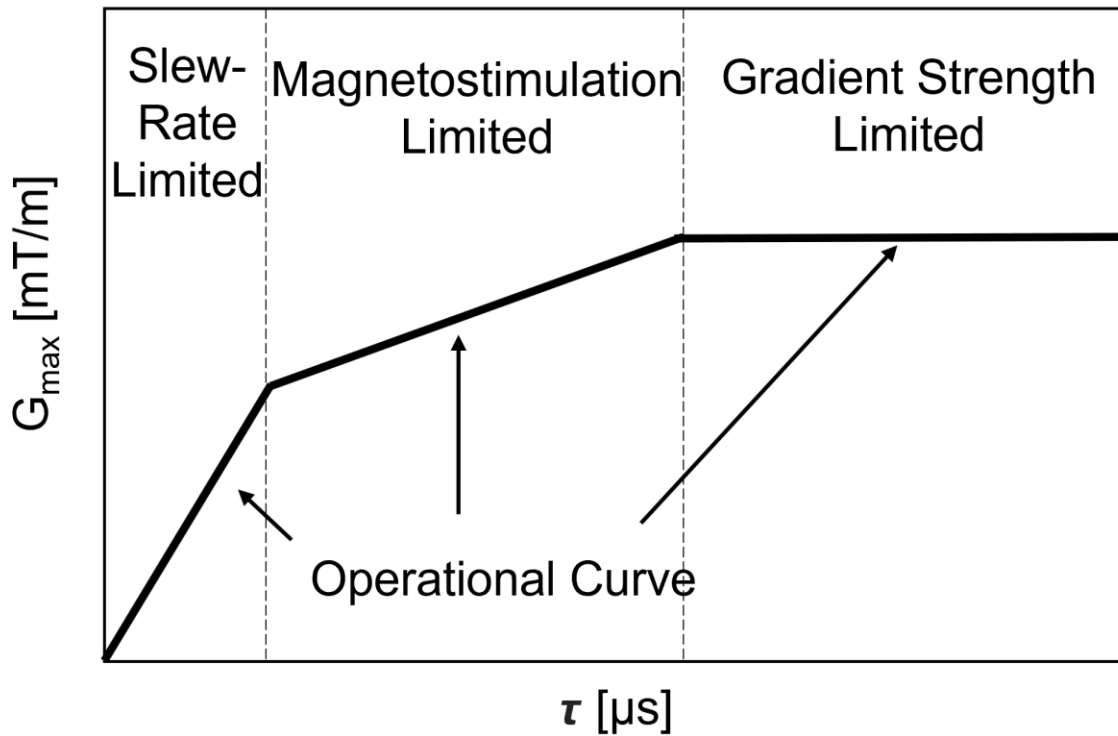


Figure 1-4: Magnetostimulation Operational Curve

An example experimentally derived operational curve indicating G_{\max} and τ combinations which are determined to be safe for minimizing stimulation. The first region of the curve is limited by maximum achievable slew-rate, the second is limited by experimentally derived magnetostimulation results, and the third is limited by the maximum achievable gradient strength.

In Figure 1-4 the switching speed is written as τ which is the time it takes to go from 0 to G_{\max} and is the rise-time and related to the slew-rate of the gradient coil. In the regions of Figure 1-4 the first region is limited by the slew-rate of the gradient coil, the second is limited by experimentally derived magnetostimulation measurements and the third is limited by the maximum gradient strength that the gradient coil is able to achieve. In general, the smaller radius of head-optimized gradient coils pushes the curve upwards enabling stronger gradients and quicker slew-rates before magnetostimulation occurs.

Construction of gradient coils is an intricate engineering task ensuring that the windings are located at the desired location, electrical connections can handle the current and voltage the coil will be subjected to, and that the coil does not move during operation from the high Lorentz forces it will experience. Modern gradient coils are typically either cut into sheets

of copper and affixed to structural support or wound with either hollow or solid wire. It is also important that the gradient coil is cooled which can be accomplished using hollow wire in which coolant is directly run or through cooling lines in contact with the wire structures. In a typical gradient configuration, the X-gradient lays on the left and right of the cylindrical structure, the Y-gradient on the top and bottom and the Z-gradient is wound around the cylinder. The X- and Y-gradient configurations with current direction and produced magnetic fields are shown graphically in Figure 1-5. In this figure the copper gradient thumbprints are shown saddling the full cylinder with their respective current directions and resultant magnetic field profiles. Large wires are used to handle the currents required to drive the gradient coils and traditionally the windings are encased in epoxy to prevent motion during operation as a result of the Lorentz forces. Finally, the choice of gradient coils for manufacturing are often balanced for forces and torques during the design process so that the net values are limited during operation.

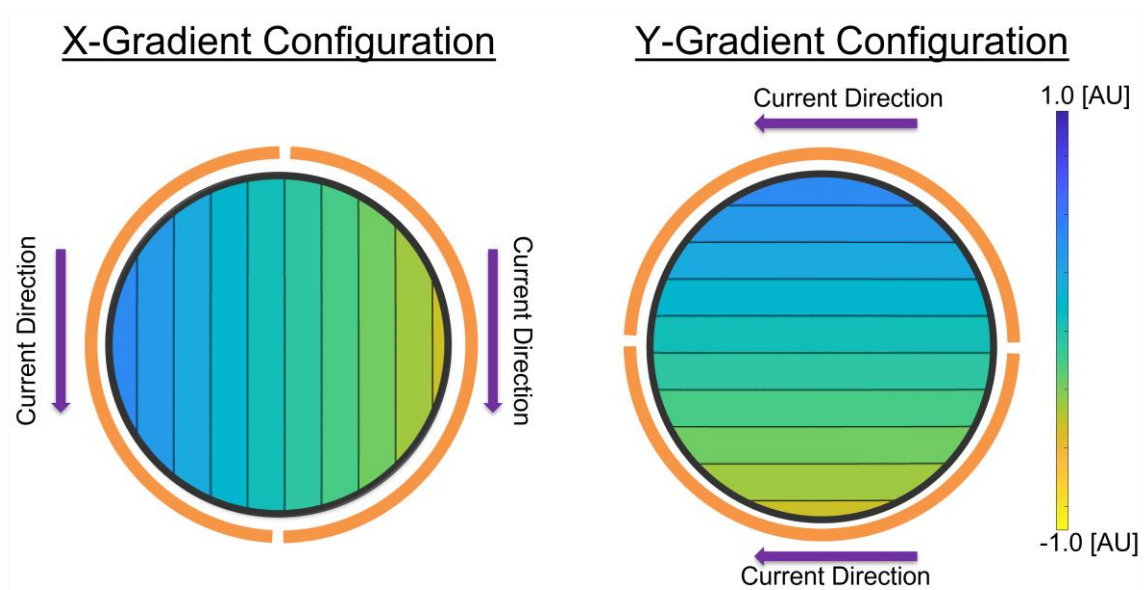


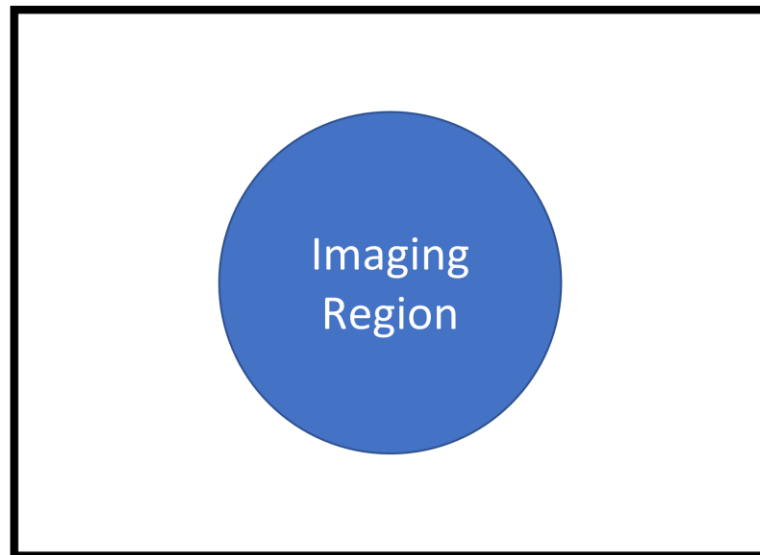
Figure 1-5: Traditional Transverse Gradient Configurations

Cross-sectional view of a gradient coil configuration showing the gradient layers (copper coloured) saddling the structural support (black circle). When current is run through the gradient coil a magnetic field is produced. Colour indicates the strength of the magnetic field produced. The linear variation in the magnetic field produced by the X-gradient and Y-gradient coils is highlighted through contour lines.

1.2.4 Symmetric vs Asymmetric Head Gradient Coils

The anatomical target of an MRI is a significant dictator of the size of the electromagnets with head-optimized scanners utilizing small internal radii which poses an inherent issue with patient entrance. Symmetric gradient coils have their imaging region located at the geometric center of the gradient coil whereas asymmetric gradient coils have their imaging region shifted towards the patient side. Figure 1-6 shows a birds-eye view cartoon illustration of this for symmetric and asymmetric gradients to scale with a 0.25 m imaging region which is typical of a head-optimized system. Here the imaging region offset (IR_{offset}) is the extent to which the imaging region is shifted from the isocenter and the black box represents the gradient coil size and shape with everything drawn to scale for a representative head-optimized gradient coil.

Symmetric Gradient



Asymmetric Gradient

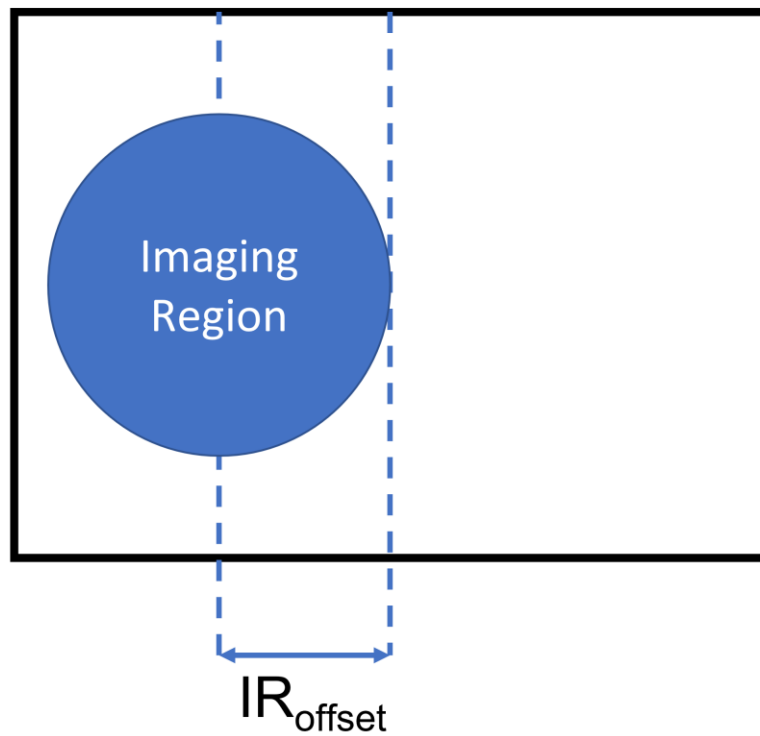


Figure 1-6: Symmetric and Asymmetric Gradient Configurations

Birds eye view of a symmetric gradient coil with the imaging region located at the geometric centre and an asymmetric gradient coil with the imaging region shifted linearly from the geometric centre by a distance IR_{offset} towards the patient end.

For a symmetric gradient to encompass the entire brain region this requires short gradient coils which are difficult to design. If the design is too long the imaging region only contains the upper portion of the head with the lower portion outside of the homogeneous field region. This is solved by utilizing asymmetric gradient coils with a shifted linear field region allowing the imaging region to completely encompass the head. However, asymmetric gradient coils are more difficult to design with poorer shielding, tighter wires due to the current density required near the patient end, an increase in eddy current complexity, and difficulty balancing for forces and torques during operation. This plays a role in limiting the extent to which the imaging region can be moved towards the patient end requiring extra consideration in the design process balancing this asymmetry with performance goals.

1.3 Matrix Coil Arrays

Another method of creating magnetic field profiles which has had success in the research setting is arrays of independently driven coil loops. These have been explored for dynamic slice-by-slice shimming (15, 16), creating gradient fields (17), and full imaging (18). Instead of a single electromagnet producing a single magnetic field profile in the case of a matrix array arbitrary magnetic field shapes are produced by driving the individual current loops with a predetermined current profile. These matrix array elements are traditionally placed near the body and have begun competing with the RF receive chain for spacing. This has led to the integration of the multi-coil elements and the RF coil into a single integrated system such as the integrated parallel reception excitations and shimming (iPRES) coil (19) or the AC/DC coil (20).

1.4 Quasistatic Electromagnet Design Methods

1.4.1 Quasistatic Magnetic Fields

The quasistatic regime is the transition between electrostatics and electrodynamics and “refers to the regime for which the finite speed of light can be neglected, and fields treated

as if they propagated instantaneously. Said in other, equivalent words, it is the regime where the system is small compared with the electromagnetic wavelength associated with the dominant time scale of the problem.” (21). Functionally, this allows one to neglect the contribution from Maxwell displacement current to Ampere’s Law (22). This work is concerned with magnetoquasistatic fields as the electromagnets that govern the MR environment such as the gradient coils fall within this range. It is important to note that RF coils typically fall outside this and therefore have a different requirement for their electromagnetic design and simulations. In this regime although the magnetic fields are varying with time, they are slowly varying with respect to the time scale of the problem and therefore at any instance in time can be treated as a static case. Effectively, this means no significant wavelength effects and that the magnetic fields fully penetrate the body. This assumption greatly simplifies the underlying physics and allows approximations, such as the Biot-Savart approximation, to be acceptable methods of computing magnetic fields.

1.4.2 Boundary Element Method

There exist many methods of designing wire patterns for electromagnets however, a review of all of them is outside of the scope of this thesis. However, this thesis makes significant use of a Boundary Element Method (BEM) stream function approach to derive wire patterns for MR gradient coils, active shims, and RF coils. A brief introduction to the key equations will be presented here with a further derivation included in Appendix A. For the interested reader, the author directs them to the following references (23–29).

1.4.2.1 The Stream Function

A stream function is a mathematical representation of steady incompressible fluid over a surface. The goal in designing an electromagnet using the BEM is to calculate a current distribution over any arbitrary surface that produces a desired magnetic field profile at chosen target points. In the stream function representation this current distribution can be thought of as the fluid flow of electrons over a surface.

In the case of a current profile with no sources or sinks the electromagnetic continuity equation is equal to:

$$\nabla \cdot \mathbf{J} = 0 \quad (1.19)$$

With the surface current density as a divergence free vector field, it follows that the surface current density can be written as the curl of a scalar stream function residing on the surface tangential to the normal. This tangential requirement ensures the stream function is constrained to the surface itself.

$$\mathbf{J}(\mathbf{r}) = \nabla \times [\psi(\mathbf{r})\mathbf{n}(\mathbf{r})] \quad (1.20)$$

The problem domain is then discretized with the surface represented as nodes and triangles and the stream function approximated by a piece-wise stream function at each node. An example planar surface highlighting an example node and its surrounding triangles are shown in Figure 1-7.

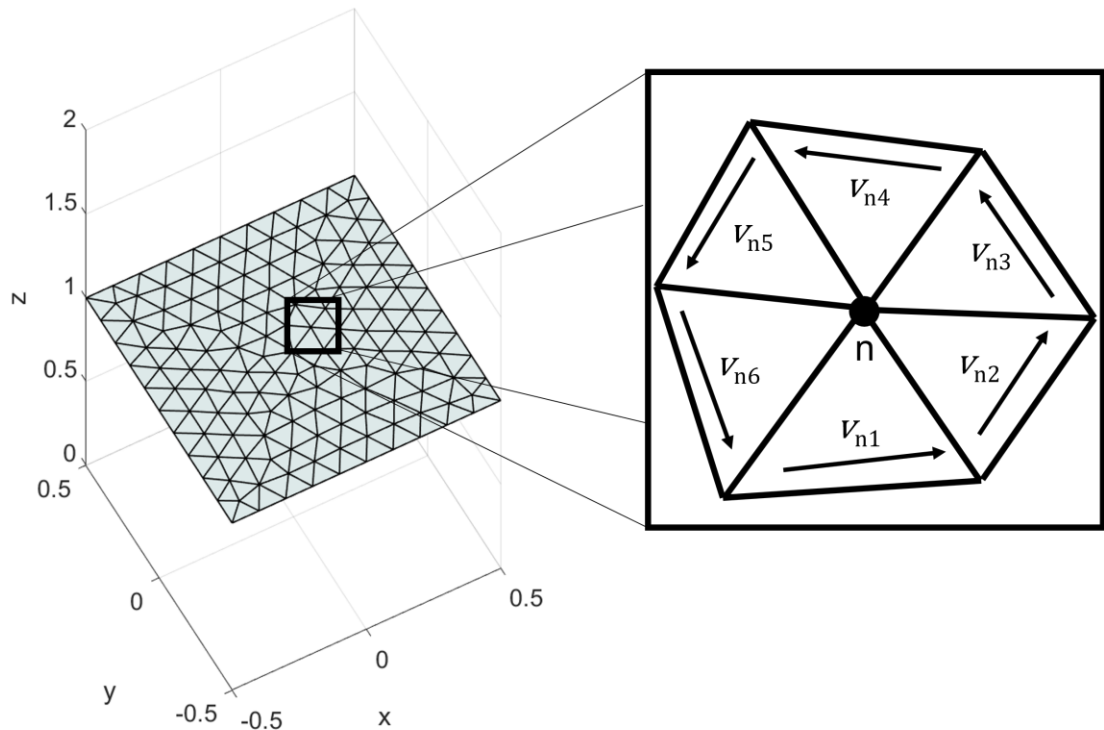


Figure 1-7: Meshed Surface and Element

Discretized planar surface and example zoomed in node on example node n . Zoomed in node n is surrounded by six triangular elements each with an encircling current basis function (v_{n1}, \dots, v_{n6}).

With the surface discretized the stream function must be appropriately discretized as well. The stream function is approximated as the sum of a piece-wise function of the stream function values at each node on the surface multiplied by a surface basis function:

$$\psi(\mathbf{r}) = \sum_{n=1}^N I_n \psi_n(\mathbf{r}) \quad (1.21)$$

$$\psi_n(\mathbf{r}) = \begin{cases} N_{nj}(\tilde{x}, \tilde{y}); & \text{if } \mathbf{r} \text{ is inside } \Delta_j \\ 0; & \text{if } \mathbf{r} \text{ is outside } \Delta_j \end{cases} \quad (1.22)$$

ψ_n is a set of basis functions consisting of linear shape functions over the elements of the discretized surface previously described (25, 26), I_n is the stream function value at node n on a surface with a total of N nodes, and N_{nj} is the linear shape functions for element j . With the stream function discretized in this way the current density is similarly written as:

$$\mathbf{J}(\mathbf{r}) = \sum_{n=1}^N I_n \nabla \times [\psi_n(\mathbf{r}) \mathbf{n}(\mathbf{r})] \quad (1.23)$$

$$\mathbf{J}(\mathbf{r}) = \sum_{n=1}^N I_n \mathbf{J}_n(\mathbf{r}) \quad (1.24)$$

$$\mathbf{J}_n(\mathbf{r}) = \sum_{k=1}^K \mathbf{v}_{nk} = \sum_{k=1}^K \frac{\mathbf{e}_{nk}}{2A_k} \quad (1.25)$$

Here, K is the total number of triangular elements which surround the node n , \mathbf{e}_{nk} is the edge vector opposite of node n within element k , and A_k is the area of element k . In Figure 1-7 the middle node n is surrounded by six triangular elements with encircling current basis functions ($\mathbf{v}_{n1} \dots \mathbf{v}_{n6}$) around the node. They are equivalently equal to the vector of the opposite edge divided by twice the elemental area.

1.4.3 Performance Functional

Relevant electromagnetic parameters such as produced magnetic field, gradient dissipative power, shielding, and forces/torques can be written in terms of the stream function and

incorporated into a performance functional. The introduction of a performance functional accomplishes two things. First, it allows fine tuning the relative importance of various electromagnetic features of the electromagnet such as field homogeneity, heating, and shielding. This is important because one desires electromagnets to be designed that achieve certain standards. Second, it reduces the problem to a single solution satisfying the design problem and functional specifics. I begin by defining a performance functional U and incorporating the terms of importance into it to be used in the design process. Full derivations of each are included in Appendix A

$$U = \frac{1}{2} \sum_{k=1}^K [B_z(r_k) - B_z^{\text{tar}}(r_k)]^2 + \frac{\beta}{2} P + \frac{\gamma}{2} P^{\text{cryo}} - \lambda_x M_x - \lambda_y M_y - \lambda_z M_z \quad (1.26)$$

Here, B_z is the produced magnetic field from the stream function, B_z^{tar} is the target field profile used in the design algorithm, both of which are calculated at k target points with position values r_k . β is the weighting of gradient dissipative power (P), γ is the weighting of the induced power in a representative bore surface due to an induced eddy current (P^{cryo}), and M_x , M_y , and M_z are torque constraints with a corresponding Lagrange multipliers λ_x , λ_y , and λ_z .

With the performance functional complete, it is differentiated with respect to the stream function and Lagrange multipliers. This is used to formulate the problem in a series of matrix equations which are solved through matrix inversion to calculate the stream function value over the surface. An example mesh, solved surface stream function and resultant gradient wire pattern are shown in Figure 1-8.

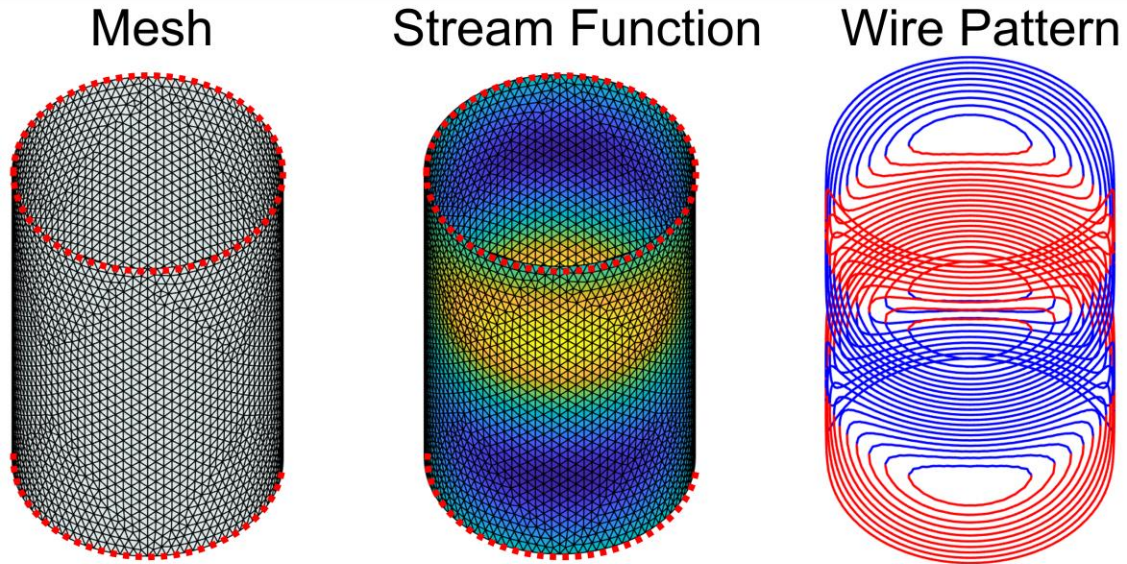


Figure 1-8: Example computational mesh, solved stream function and resultant wire pattern

Cylindrical computational mesh and solved stream function over the mesh. Red dots indicate nodes which are constrained to the same value to prevent flow over the surface. This process is outlined in Appendix A. The solved stream function plot shows surface colour using the stream function value at each node linearly interpreted over the elements. Final portion shows resultant wire pattern after contouring the stream function. Wire pattern colour indicates the current direction with respect to the azimuthal direction.

1.4.4 Low vs. High Field

As outlined in Chapter 1.1 there are direct benefits because of the underlying physics towards using higher magnetic field strengths. From Equation 1.1 we see that the initial magnetization is directly proportional to the magnetic field strength, the number of spins, and is inversely proportional to the temperature. This leads to higher MR signals in substances with greater spin density but also allows methods of increasing the signal through increased magnetic fields or decreased temperatures. Increasing the spin density of tissue is not possible and as an MR experiment is mostly performed in-vivo it is impractical to cool the patient for little return in terms of signal. This has resulted in a drive towards higher field strengths.

1.4.5 Point-of-Care MRI

Point-of-care MRI has no standard definition and can mean a range of different things to different works. In this thesis, I define point-of-care MRI as “*the use of MRI outside of the*

imaging department” a simple definition which differentiates traditional usage of MRI where a patient is referred to a separate department within a hospital or brought to an imaging center. This includes MRI implementations which are housed within a department such as emergency medicine but consists of a dedicated unit, often smaller and easier to implement, or a design which can be brought directly to patients. In addition, since the distribution of imaging scans is not the same across all body parts or pathologies these scanner implementations often choose to tackle a small subset of the imaging capability of a full scanner. Much work has been geared towards head imaging however some scanners have been designed for extremity imaging (30) and concurrent MR and irradiation (31, 32).

1.4.6 Current Implementations

There exists great interest in both the research and commercial setting for point-of-care MRI platforms. The following sub-chapters will outline a non-exhaustive list of some of the further along examples.

1.4.6.1 Research Implementations

He *et al.* (33) has demonstrated the feasibility of their head-only lightweight MRI system consisting of a permanent magnet design with a 50.9 mT B_0 field strength. The total system weight is 350 kg and employ biplanar gradients with the aim of intensive care unit imaging of cerebral stroke cases.

Nakagomi *et al.* (34) recently demonstrated the feasibility of their 200 mT small joint MRI scanner. With a total weight of 280 kg including equipment, it is designed to fit within the limited space of a cube van and has demonstrated the utility of this system screening for elbow injuries. Their imaging volume was a 0.1 m diameter sphere and employed biplanar gradient coils. They demonstrated sufficient but low SNR when compared to a commercial scanner. In their experiments room shielding was unavailable so they designed a copper shielding box to be placed by the magnet setup and a rectangular aluminum shield for placing around the bottom to help alleviate electromagnetic noise.

O’Reilly *et al.* (4) designed a Halbach Array style head-optimized MRI with a B_0 field strength of 50.4 mT and an inner bore diameter of 0.27 m with an imaging region of 0.20

m. The magnet system had a cost of approximately 4000 euros and a total weight of 75 kg making it an economical and lightweight choice. This short magnet configuration employed gradients of 0.29 m long and 0.25 cm in outer diameter. They demonstrated imaging capabilities performing 3D imaging in a brain phantom inside a Faraday cage to minimize noise.

1.4.6.2 Commercial Implementations

Panther *et al.* (35) with Synaptive Medical demonstrated the feasibility of their 500 mT head-optimized scanner as compared to clinical field strengths. This setup uses a superconducting cryogen-free magnet with a separate hot room for electrical connections and amplifiers. While not designed to be transported to patients the low siting requirements of their magnet setup allows the MRI system to be placed in areas where typical clinical MRI scanners would be infeasible given their siting requirements.

Hyperfine, Inc., created the first FDA-cleared portable MRI system which uses a permanent magnet setup with a B_0 field of 64 mT which has shown clinical utility imaging at the bedside of critically ill patients (36).

1.5 Thesis Overview

This thesis outlines computational design work which started as an investigation of the question “*can we design an MRI gradient coil for compact head-optimized geometries which allows imaging of the cervical spine*” and evolved into the experimental testing of design methods for frequencies greater than gradient operational frequencies and an exploration of adapting multi-coil techniques to the demands of complex eddy current compensation. Chapter 2 begins the story by investigating the design of a small radius gradient coil with shoulder cut-outs to allow patients to further enter the gradient coil and enabling neck imaging. Chapter 3 proposes a unique gradient axis configuration, with updated gradient geometries to ensure fitting an appropriate range of patients, to mitigate some of the performance loss due to employing a shoulder cut-out gradient coil. Chapter 4 explores the trade-offs in spherical harmonic resistive shim placement in a shoulder cut-out MRI platform. Chapter 5 tests the design methods used for gradient technologies for the application of low-frequency RF coils to enable unique geometries. Chapter 6 proposes

the use of a multi-coil matrix array as a method of actively compensating for higher order dynamic eddy currents using experimental eddy current data from a high-performance research prototype gradient coil. Finally, Chapter 7 outlines a summary and significance of the work while discussing the avenues in which this project may go in the future.

1.6 References

- [1] Wald LL, McDaniel PC, Witzel T, Stockmann JP, Cooley CZ: Low-cost and portable MRI. *J Magn Reson Imaging* 2020; 52:686–696.
- [2] Sarracanie M, Salameh N: Low-Field MRI: How Low Can We Go? A Fresh View on an Old Debate. *Front Phys* 2020; 8(June):1–14.
- [3] Cooley CZ, McDaniel PC, Stockmann JP, et al.: A portable scanner for magnetic resonance imaging of the brain. *Nat Biomed Eng* 2021; 5:229–239.
- [4] O’Reilly T, Teeuwisse WM, de Gans D, Koolstra K, Webb AG: In vivo 3D brain and extremity MRI at 50 mT using a permanent magnet Halbach array. *Magn Reson Med* 2021; 85:495–505.
- [5] O’Reilly T, Teeuwisse WM, Webb AG: Three-dimensional MRI in a homogenous 27 cm diameter bore Halbach array magnet. *J Magn Reson* 2019; 307:106578.
- [6] Gruber B, Froeling M, Leiner T, Klomp DWJ: RF coils: A practical guide for nonphysicists. *J Magn Reson Imaging* 2018; 48:590–604.
- [7] Ahmad SF, Kim YC, Choi IC, Kim HD: Recent progress in birdcage RF coil technology for MRI system. *Diagnostics* 2020; 10:1–19.
- [8] Golay MJE: Field Homogenizing Coils for Nuclear Spin Resonance Instrumentation. *Rev Sci Instrum* 1958; 29:313–315.
- [9] Mansfield P: Multi-planar image formation using NMR spin echoes. *J Phys C Solid State Phys* 1977; 10:L55–L58.
- [10] Turner R: A target field approach to optimal coil design. *J Phys D Appl Phys* 1986;

19:L147–L151.

[11] Turner R: Gradient coil design: A review of methods. *Magn Reson Imaging* 1993; 11:903–920.

[12] Hidalgo-Tobon SS: Theory of Gradient Coil Design Methods for Magnetic Resonance Imaging. *Concepts Magn Reson Part A* 2010; 36:223–242.

[13] Setsompop K, Kimmlingen R, Eberlein E, et al.: Pushing the limits of in vivo diffusion MRI for the Human Connectome Project. *Neuroimage* 2013; 80:220–233.

[14] Foo TKF, Tan ET, Vermilyea ME, et al.: Highly efficient head-only magnetic field insert gradient coil for achieving simultaneous high gradient amplitude and slew rate at 3.0T (MAGNUS) for brain microstructure imaging. *Magn Reson Med* 2020; 83:2356–2369.

[15] Juchem C, de Graaf RA: B₀ magnetic field homogeneity and shimming for in vivo magnetic resonance spectroscopy. *Anal Biochem* 2017; 529:17–29.

[16] Stockmann JP, Wald LL: In vivo B₀ field shimming methods for MRI at 7 T. *Neuroimage* 2018; 168(June 2017):71–87.

[17] Littin S, Jia F, Layton KJ, et al.: Development and implementation of an 84-channel matrix gradient coil. *Magn Reson Med* 2018; 79:1181–1191.

[18] Juchem C, Theilenberg S, Kumaragamage C, et al.: Dynamic multicoil technique (DYNAMITE) MRI on human brain. *Magn Reson Med* 2020; 84:2953–2963.

[19] Han H, Song AW, Truong TK: Integrated parallel reception, excitation, and shimming (iPRES). *Magn Reson Med* 2013; 70:241–247.

[20] Gao Y, Mareyam A, Sun Y, et al.: A 16-channel AC/DC array coil for anesthetized monkey whole-brain imaging at 7T. *Neuroimage* 2020; 207(August):116396.

[21] John David Jackson: *Classical Electrodynamics*. 1998.

- [22] Larsson J: Electromagnetics from a quasistatic perspective. *Am J Phys* 2006; 75:230–239.
- [23] Poole M: Improved Equipment and Techniques for Dynamic Shimming in High Field MRI. *PhD thesis, Univ Nottingham, United Kingdom, 2007(August):25.*
- [24] Harris CT: Optimization of a boundary element approach to electromagnet design with application to a host of current problems in Magnetic Resonance Imaging. *Phd thesis, West Univ* 2013.
- [25] Lemdiasov RA, Ludwig R: A stream function method for gradient coil design. *Concepts Magn Reson Part B Magn Reson Eng* 2005; 26B:67–80.
- [26] Peeren GN: Stream function approach for determining optimal surface currents. *J Comput Phys* 2003; 191:305–321.
- [27] Tomasi D: Stream function optimization for gradient coil design. *Magn Reson Med* 2001; 45:505–512.
- [28] Poole M, Bowtell R: Novel gradient coils designed using a boundary element method. *Concepts Magn Reson Part B Magn Reson Eng* 2007; 31B:162–175.
- [29] Harris CT, Haw DW, Handler WB, Chronik BA: Shielded resistive electromagnets of arbitrary surface geometry using the boundary element method and a minimum energy constraint. *J Magn Reson* 2013; 234:95–100.
- [30] Bretlau T, Christensen OM, Edström P, Thomsen HS, Lausten GS: Diagnosis of scaphoid fracture and dedicated extremity MRI. *Acta Orthop Scand* 1999; 70:504–508.
- [31] Fallone BG: The Rotating Biplanar Linac-Magnetic Resonance Imaging System. *Semin Radiat Oncol* 2014; 24:200–202.
- [32] Lagendijk JJW, Raaymakers BW, van Vulpen M: The Magnetic Resonance Imaging-Linac System. *Semin Radiat Oncol* 2014; 24:207–209.
- [33] He Y, He W, Tan L, et al.: Use of 2.1 MHz MRI scanner for brain imaging and its

preliminary results in stroke. *J Magn Reson* 2020; 319:106829.

[34] Nakagomi M, Kajiwara M, Matsuzaki J, et al.: Development of a small car-mounted magnetic resonance imaging system for human elbows using a 0.2 T permanent magnet. *J Magn Reson* 2019; 304:1–6.

[35] Panther A, Thevathasan G, Connell IRO, et al.: A Dedicated Head-Only MRI Scanner for Point-of-Care Imaging. In *Proc Intl Soc Mag Reson Med 27*; 2019.

[36] Sheth KN, Mazurek MH, Yuen MM, et al.: Assessment of Brain Injury Using Portable, Low-Field Magnetic Resonance Imaging at the Bedside of Critically Ill Patients. *JAMA Neurol* 2021; 78:41–47.

Chapter 2

2 Investigation of a Shoulder Cut-out MRI Gradient Coil

This chapter consists of an expanded version of the peer-reviewed conference abstract:

Eric J. Lessard, William B. Handler, and Blaine A. Chronik. *Preliminary Design Exploration for a Head and Neck Gradient Coil: Effect of Shoulder Cut-out Length on Performance*. International Society for Magnetic Resonance Imaging Annual Meeting 2019.

2.1 Introduction

The primary cause of ischemic stroke is due to narrowing of the arteries which provide the brain with blood. Cholesterol deposits within the arteries in the head or neck can either dislodge, resulting in it becoming trapped in the narrower arteries downstream in the brain (embolism), or they can stay within the artery in which they were initially formed (thrombosis). In acute ischemic stroke in which a patient visits the emergency room, diagnostic imaging can play an important role in differentiating between patients who need immediate intervention and those of which who do not. This is important because in treatment of acute ischemic stroke, “time is brain” (1) as every minute a patient does not receive appropriate treatment results in neuronal loss. Outside of acute scenarios, monitoring of arterial plaque build-up within the carotid arteries (atherosclerosis) is important for determining response to treatment and patient screening.

Magnetic resonance imaging (MRI) plays an important role in diagnostic imaging of the head and neck, as it provides excellent soft tissue contrast with no delivered ionizing radiation. Typically, neck pathologies are imaged using full-body MRI scanners designed for general hospital use. Purpose built head-only MR systems, however, have the potential to provide improved imaging of the head compared to using full body systems (2), due to their higher peripheral nerve stimulation (PNS) limits and electromagnet scaling relationships. Such head only systems are limited for imaging of the neck due to the position of the neck and cervical spine outside of the main imaging region, as the patient

is unable to slide their shoulders into the gradient coil due to the smaller radius of a head only system, typically ~ 20 cm.

Development of advanced design techniques, specifically the boundary element method (BEM) allows design and development of unique geometry gradient coils (3). This technique can be implemented to design a wire pattern over a complex geometry which produces a desired field profile. Gradient coil performance can be characterized in many ways, but end-users are typically concerned with maximum gradient strength (G_m) and slew-rate (SR). However, as gradient amplifiers vary in specifications, efficiency (η) is often used in the design process which denotes the gradient strength per unit amperage (mT/m/A). It is also important to evaluate the gradient coils shielding either in the form of stray magnetic fields or in power deposited into the bore surface. Proper shielding is paramount because induced eddy currents within conducting surfaces will have major impacts on the MR environment. Parasitic magnetic fields resultant from the eddy currents, will negatively impact imaging. The eddy currents themselves will contribute to temperature build-up within the conducting surfaces of the main magnet which can result in helium boil-off, or worse a quench scenario. This temperature build-up will also produce temperature dependent field variations in the imaging environment. Therefore, it is important that during the design process shielding is appropriately accounted for.

Much work has been done within the area of gradient coil designs for head and neck imaging. Nevertheless, due to geometrical limitations of traditional head-only gradient coils they must be designed either asymmetrically, with the imaging region shifted towards the patient end leading to an asymmetric wire pattern or with the imaging region at the centre of the gradient coil. An imaging region located at the isocentre requires a short gradient coil such that the head is located at the isocentre. However, it is possible to lengthen the gradient coil and add cut-outs to accommodate the patient's shoulders while moving the extent of the gradient coil imaging region into this cut-out region. Previous work has examined a cylindrical gradient coil with square cut outs at the patient end to accommodate the patient's shoulders (4). While other work has explored conical widening of the gradient shield to accommodate the shoulders (5). There does exist research head-only gradient coils with shoulder cut-outs (6) or shoulder-steps (7), however these are

optimized for head imaging and do not provide imaging down into the lower cervical spine. Overall, there has been no work exploring the effect of cut-out length on performance and no evaluation of purpose-built shoulder cut-out head gradient coils for the purpose of imaging both the head and neck.

In this work the effect of shoulder cut-outs for a gradient coil for imaging the head and neck is explored. I hypothesized that the use of shoulder cut outs would allow the imaging region of the gradient coil to extend further into the neck and shoulders, while maintaining acceptable imaging performance. A secondary objective was to evaluate the effect of moving the gradient coils linear region (imaging region) towards the patient end on imaging performance.

2.2 Methods

Triangular element meshes with shoulder cut-outs (cut-out height: 0.15 m, cut-out length: 0.07 – 0.21 m) on the primary surface were designed in, and exported from, COMSOL Multiphysics (COMSOL, Burlington, MA) for use in MATLAB (Mathworks, Natick, MA). The surfaces had between 4000 and 4700 boundary elements and between 320 and 400 edge elements (example mesh shown in Figure 2-1a with the red lines denoting the cut-out on the primary surface and the blue dotted region representing the target linear region). Figure 2-1b shows an example 3D rendered image of an example body model within a 0.21 m cut-out gradient coil illustrating the potential extent of patient coverage. The primary (shield) surface geometries were designed to fit within a bore of diameter 0.60 m and length 1.0 m and thus the x-, y-, and z-surfaces had internal diameters of 0.41 m (0.56 m), 0.44 m (0.58 m) and 0.42 m (0.57 m), respectively with varying lengths of 0.55 m (no cut-out), 0.62 m (0.07 m cut-out), 0.69 m (0.14 m cut-out), and 0.76 m (0.21 m cut-out). The shield surface could run the entire length of the bore and therefore had a maximum allowable length of 1.0 m.

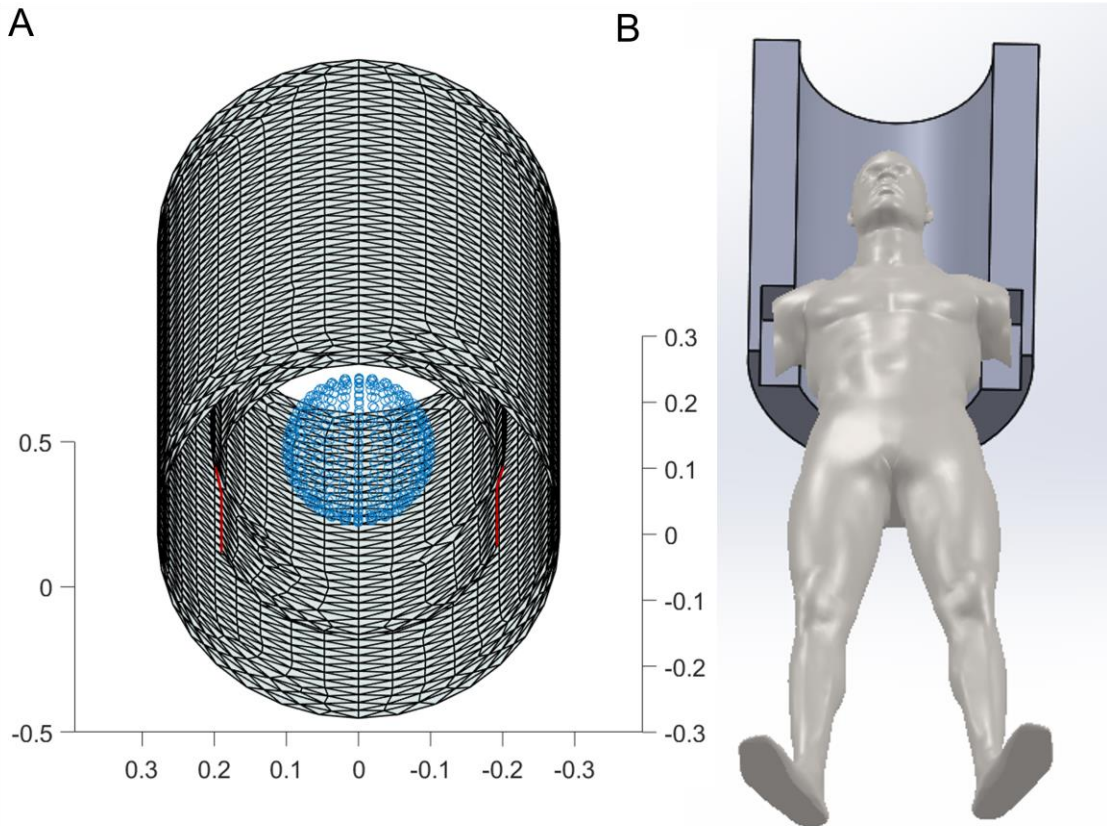


Figure 2-1: Shoulder Cut-out Computational Mesh and Cartoon Illustration

A) an example meshed surface with a discretized blue sphere showing the imaging region. Red lines are included to highlight the shoulder cut-out location. B) cartoon illustration demonstrating the further patient entrance achievable using a shoulder cut-out configuration.

The BEM method was implemented using custom built MATLAB software, taking advantage of optimized parallel routines written in C++, aiming for control of field uniformity and minimum wire spacing (8). The design algorithm was optimized to provide a minimization of the power deposited into the bore surface. In this method a set of field targets were chosen and the problem of current density flowing on the surface was solved using a stream function based approach (3, 4, 9, 10) solving for the stream function value at each of the boundary element nodes. The stream function is then contoured to produce a wire pattern which matches the desired field at the targets. The contour spacing can be modified to account for design constraints arising from minimum wire spacing. I also introduced a set of Lagrange multipliers to ensure that the net torque on the gradient coil is zero. This is done by introducing Lagrange multipliers into the functional as follows.

$$U = \frac{1}{2} \sum_{k=1}^k [B_z(\mathbf{r}_k) - B_z^{tar}(\mathbf{r}_k)]^2 + \frac{\beta}{2} P + \frac{\gamma}{2} P^{bore} + \lambda_x M_x + \lambda_y M_y + \lambda_z M_z \quad (2.1)$$

Where, U is our functional to be minimized, B_z is the z-component of the produced magnetic field (from the gradient coil) and B_z^{tar} is the magnetic field targets which are set as part of the design process (linearly varying field in the case of gradient coil design). P and P^{bore} are the power deposited into the coil and bore surfaces, respectively and their relative weighting are given by β and γ . M_x , M_y and M_z are the torque matrices with M_{nx} , M_{ny} , and M_{nz} , being the torque on the n^{th} node due to the stream function at that node (I_n) in the x, y, and z directions and λ being the corresponding Lagrange multiplier. The torque is calculated using an idealized perfectly homogeneous magnetic field profile. Included in the design is an iterative algorithm (8) which modifies functional weights based on a designs field uniformity (homogeneity) and wire spacing. The algorithm uses user specified values for target maximum field inhomogeneity (H_{max}), minimum wire spacing (W_{min}), and number of times to iterate the algorithm (N). This allows fine tuning the inhomogeneity for each design and allowing minimum wire spacing to be directly incorporated into the design stage. The minimum wire spacing is the smallest physical separation between any wire combination in the derived wire pattern.

It can be seen from above that there are many design inputs arising from the functional (β , the weighting of our gradient coil system power and γ , the weighting of our power deposited into the bore surface) and our iterative control of wire spacing and field homogeneity algorithm (W_{min} , the target acceptable wire spacing, H_{max} , the maximum field inhomogeneity and N , the number of iterations) produces a 5-dimensional design space of input metrics (β , γ , W_{min} , H_{max} and N). Briefly, this means for a combination of β , γ , W_{min} , H_{max} and N a single gradient coil is designed. Each of these parameters is varied to build up a design space, where each combination results in a single candidate gradient coil. This design space search was performed initially on a coarse mesh, for computational speed. The β and γ spacing span a larger range of reasonable values than W_{min} , H_{max} and N which led to the design space being initially filled using coarse spacing between β and γ values. In the interest of time this coarse search was used to locate the region in the design space

where the solution to our problem is physical, manufacturable, and provides performance parameters suitable for imaging. After this region was narrowed down and identified the fineness of the spacing between β and γ values was increased to explore the final design candidates further. Once a final gradient coil design has been chosen, the fineness of the computational mesh was increased so that the final gradient coils had the smoothest wire pattern and most accurate calculations of relevant performance parameters. In the design algorithm it is possible to set certain metrics. In this work I initially set the efficiency to 0.10 mT/m/A, this influences the design problem as the minimum separation between wires will not necessarily converge on the input W_{\min} as a certain design may require unphysically tight wires in order to achieve the target efficiency. It is possible to increase efficiency without increasing wire density on a surface using a third computational surface for current to flow. This will increase efficiency at a cost, namely inductance, and was deemed unnecessary for this work as the efficiency target was achievable given the two-surface design approach.

For this work a target imaging region was chosen as a 0.2 m diameter sphere situated +0.07 m (control coil), +0.14 m (0.07 m cut-out coil), +0.14 m and +0.21 m (0.14 m and 0.21 m cut-out coils), and +0.14 m, +0.21 m and +0.28 m (0.21 m cut-out coil) from the isocenter. These additions increased the complexity of our design space. A 3D rendered example of this is shown graphically in Figure 2-1b, illustrating an example of a 0.21 m cut-out.

The large design space grid search and combination of cut-out lengths and IR_{offset} resulted in, for each gradient axis, thousands of candidate coils each with their own performance metrics. However, in order to meet the efficiency target a particular candidate may not converge onto a manufacturable W_{\min} and were therefore discarded for analysis if the wire spacing required was unphysically small. If such a coil were manufactured using a water-jet cutter gradient axes required an absolute minimum wire separation of ~ 3.5 mm and if they were manufactured from all hollow wire they would require an absolute minimum separation of ~ 5.5 mm (11). Our in-house manufacturing method involves using a 5-axis water-jet cutter to cut the gradient thumbprints into copper sheets which are then rolled to a specific radius and mounted to G10. The water-jet cutter uses garnet dust and a fine stream of water at high pressure (95,000 psi) and cuts the copper at locations determined

by the BEM. This directly couples the manufacturing method with the design method to ensure that any design which is chosen from a design study such as this adheres to the tolerances of all manufacturing steps.

Some designs had efficiencies higher than the target efficiency and therefore for evaluation of gradient coil performance, I also used a performance metric of gradient coil inductance merit value defined as $M_L = \eta/\sqrt{L}$, where L is the gradient coil inductance and η is the efficiency. Another important metric is the gradient coils homogeneity over the imaging region. I define the gradient homogeneity as the relative deviation in the gradient field at a point $r = (x, y, z)$ to the gradient field at the centre of the imaging region.

$$\text{Homogeneity} = \frac{|G(\vec{r}) - G(r = 0, 0, IR_{\text{offset}})|}{G(r = 0, 0, IR_{\text{offset}})} \quad (2.2)$$

Where $G(\vec{r})$ is the gradient value at a point in space, IR_{offset} is the distance from the centre of the imaging region to the geometric centre of the gradient coil, and $G(r = 0, 0, IR_{\text{offset}})$ is the gradient value at the centre of the imaging region. I use this metric to define our DSV_{30} which is the diameter of a spherical volume over which the inhomogeneity is $<30\%$. For this work a 30% deviation in the gradient field was chosen due to advancement in gradient unwarping algorithms. However, it is possible to implement a stricter inhomogeneity target (i.e $<30\%$) within the design process.

Post-hoc I incorporated several modifications to the design requirements which were raising the target efficiency for the x-gradient (from 0.10 to 0.125 mT/m/A), y-gradient (from 0.10 to 0.15 mT/m/A), and z-gradient (from 0.10 to 0.15 mT/m/A) while also lowering the minimum wire spacing for the z-gradient (from 5.5 to 3.5 mm). The z- and y-gradient change was based on preliminary data which led us to believe it was possible to achieve a higher efficiency in these axes due to the additional space for current to flow (relative to the x-axis). The z-gradient modification was chosen due to the wire patterns which are necessary to provide the required gradient field which have a physical profile closer to that of a transverse gradient than that of a wound longitudinal gradient. This would allow the use of a water-jet for manufacturing the z-gradient wire patterns.

With these definitions and requirements in place, designs which did not meet the required minimum wire spacing were eliminated from contention. This narrowed down the candidate pool however, in the end only one design will be chosen for manufacturing. At this point all designs remaining fit engineering requirements and could be manufactured however, other performance metrics such as the size of the imaging region (DSV_{30}), inductance and effective shielding must be accounted for to ensure the final chosen gradient coils provide the best balance of all parameters. Here, we used the induced eddy current stream function in a representative bore surface and its dissipative power (Bore Power) as a measurement of shielding. Ultimately, there is no correct coil choice as gradient coil design is a complex balancing act where an increase in one parameter will result in a trade-off of another.

2.3 Results

Table 2-1 provides the theoretical electromagnetic properties of the final selected candidate coils. All gradient coils provided fields suitable for imaging, however the final selected gradient coils had the best balance of all target metrics. Table 2-2 shows the effect of moving the imaging region towards the patient end and the effect of shoulder cut-out length (constant IR_{offset}) on merit value. These metrics are given as averages \pm standard deviation across all candidates meeting the minimum efficiency and wire spacing thresholds. The effect on multiple performance parameters on moving the imaging region for constant cut-out size and adding cut-outs while keeping the imaging region at the same location are shown in Figures 2-3 and 2-4.

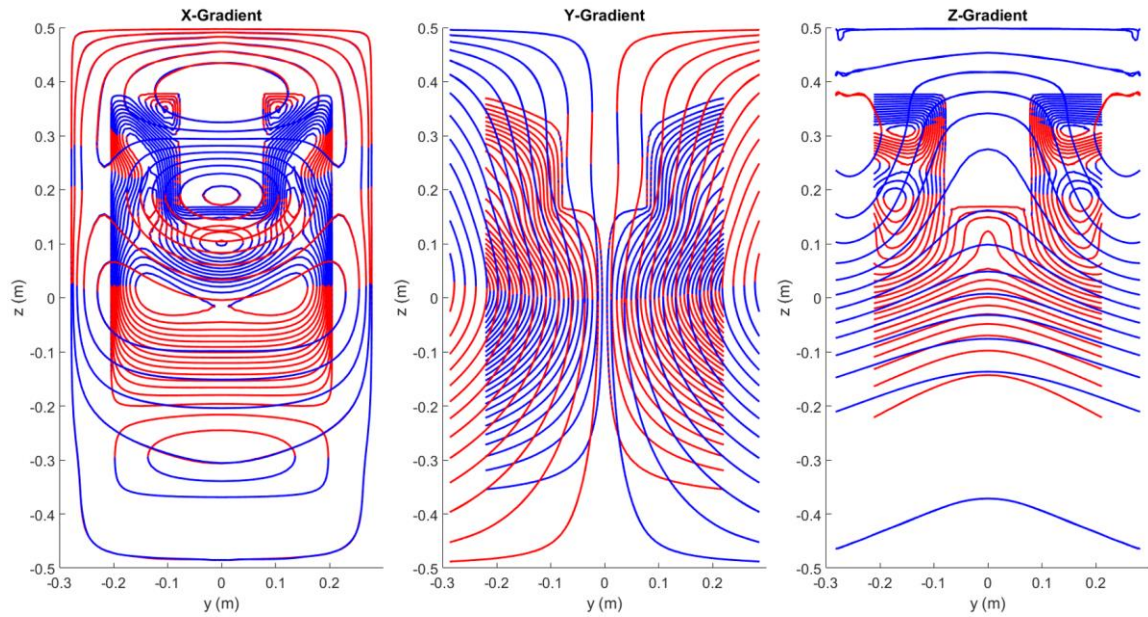


Figure 2-2: Representative Shoulder Cut-out Gradient Wire Patterns

Example gradient coil wire patterns with relevant performance parameters in Table 2-1. Wire pattern colour indicates direction of current with respect to the azimuthal direction.

Figure 2-2 shows the final selected gradient coils. Figure 2-5 shows deviations from the central value of the gradient field for the final selected gradient coil cut-out length and imaging region offset combination.

Table 2-1: Selected Gradient Coil Performance Parameters

Property	Gradient Coil		
	X	Y	Z
Cut-out Length (m)	0.21	0.21	0.21
IR_{offset} (m)	0.21	0.21	0.21
Efficiency ($\text{mT m}^{-1} \text{A}^{-1}$)	0.125	0.150	0.150
Resistance ($\text{m}\Omega$)	81	95	69
Inductance (μH)	225	284	180
Min Wire Spacing (mm)	3.8	7.1	4.2
M_L ($\text{mT m}^{-1} \text{A}^{-1} \text{H}^{-0.5}$)	8.3	8.9	11.2
DSV_{30} (m)	0.25	0.27	0.24
$ B_{\text{max}} $ at 30 cm (mT)	3.8	3.0	4.9

Relevant electromagnetic performance parameters for coils shown in Figure 2-2. DSV_{30} = diameter of spherical volume where the gradient field deviates <30%.

2.4 Discussion

To design a shoulder cut-out gradient coil for improved head and neck imaging, I explored a parameter space search of candidate gradient coils and made the following observations: (1) The X-gradient axis proved the most challenging to design due to the location of the shoulder cut-outs (2) adding longer shoulder cut-outs allowed the imaging region to be shifted further down the patient allowing both head and neck imaging (3) shifting the imaging region towards the patient end allows imaging of a greater number of anatomical regions at the expense of decreased performance.

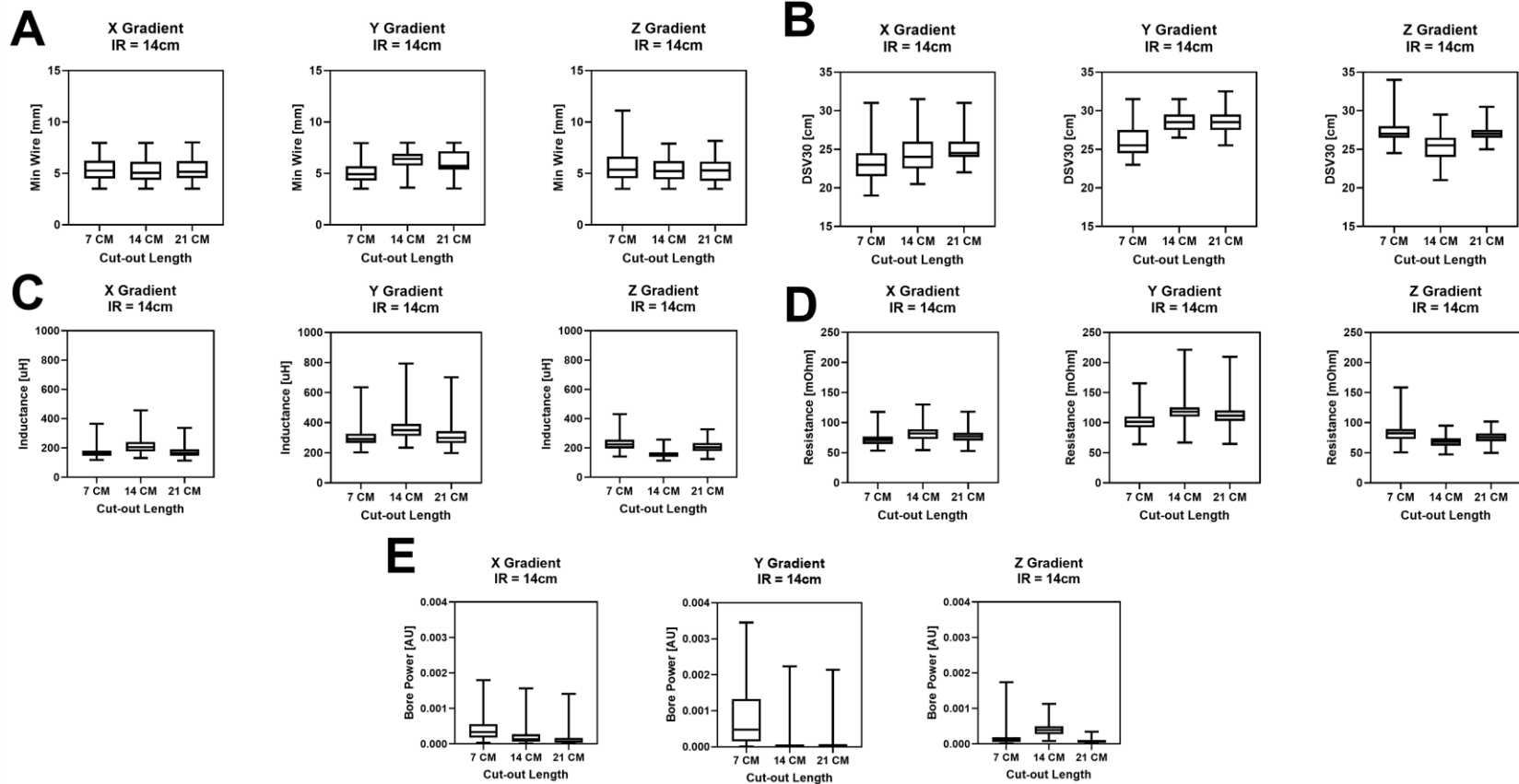


Figure 2-3: Effect of Adding Cut-out Surface

Box and whisker plots for all candidate coils across all cut-out lengths (7 cm, 14 cm, and 21 cm) when the imaging region is held constant at 14cm A) minimum wire spacing, B) Diameter of spherical volume where the gradient field deviates <30% (DSV30), C) Inductance, D) Resistance, and E) Bore Power; a measurement of shielding performance. Each candidate coil is one combination of performance functional weighting where the coil had a minimum wire spacing >3.5 mm and efficiency >0.125 mT/m/A (for X-gradients) or >0.150 mT/m/A (for Y- and Z-gradients). Candidates with values below those minimums were discarded from analysis and are not included in these plots.

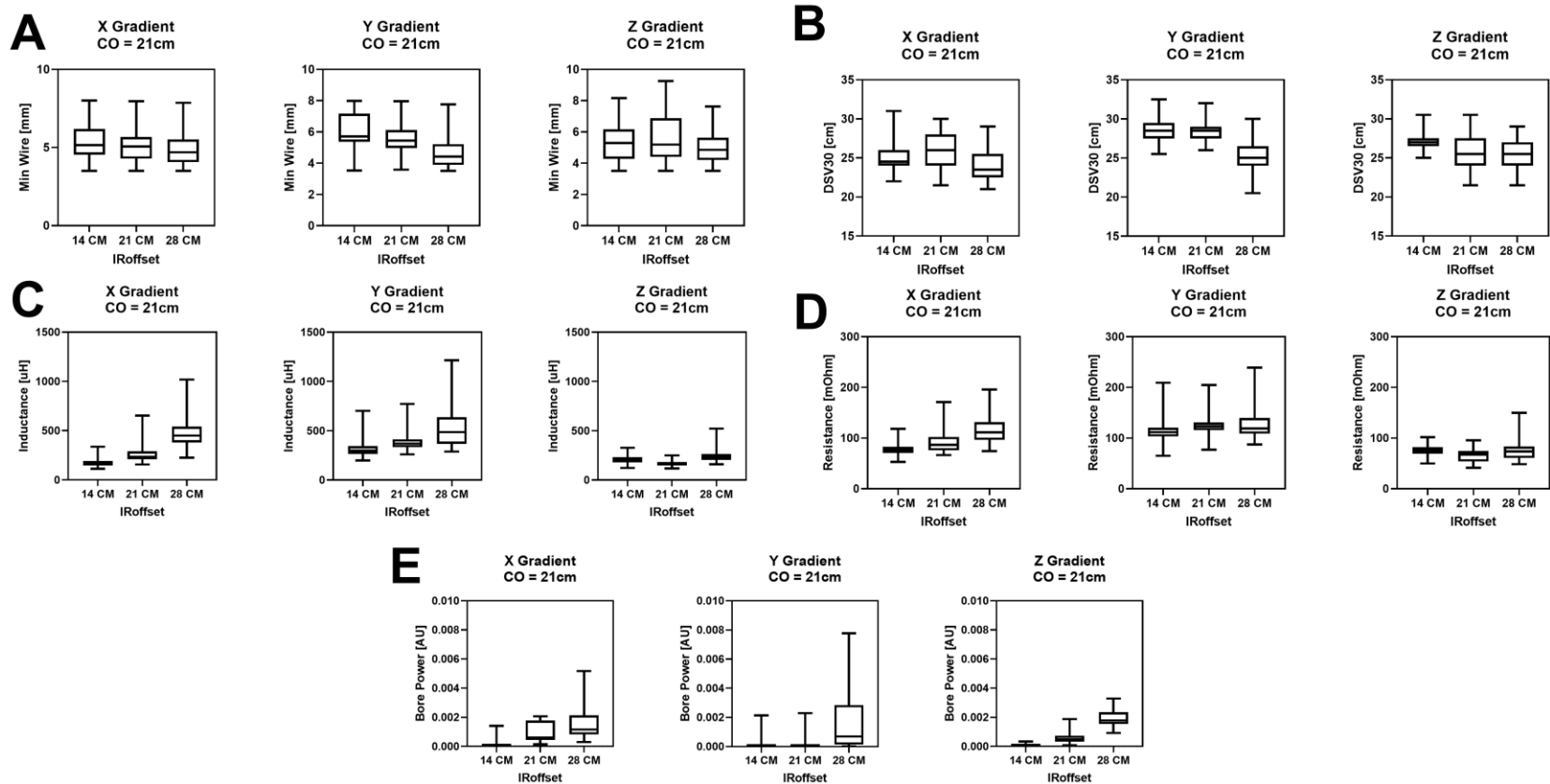


Figure 2-4: Effect of Moving Imaging Region

Box and whisker plots for all candidate coils across all imaging region offsets (14 cm, 21 cm, and 28 cm) when the cut-out size is held constant at 21 cm A) minimum wire spacing, B) Diameter of spherical volume where the gradient field deviates <30% (DSV30), C) Inductance, D) Resistance, and E) Bore Power; a measurement of shielding performance. Each candidate coil is one combination of performance functional weighting where the coil had a minimum wire spacing >3.5 mm and efficiency >0.125 mT/m/A (for X-gradients) or >0.150 mT/m/A (for Y- and Z-gradients). Candidates with values below those minimums were discarded from analysis and are not included in these plots.

Selection of the final gradient coils from the candidate pool was accomplished by first eliminating the candidates that did not meet the minimum efficiency or wire spacing criteria. Afterwards, the candidate pool was further narrowed by considering effective shielding through examining the power deposited into the bore surface. This quantity, along with the region of uniformity were used to further narrow down the candidate pool. This region of uniformity, after analysis of the successful candidate coils, was aimed to be ~ 0.25 m to allow a large imaging region for both head and neck applications. The selected imaging region offset, and cut-out length was chosen based on target anatomical regions. Although, all combinations allowed imaging further down the patient and into the cervical spine region, the longer cut-out allowed the imaging region to extend down towards the aortic arch allowing more encompassing imaging of stroke cases.

I observed a drop in the average merit value as the imaging region was moved further towards the patient end of the gradient coil. This was expected due to the tighter wires required to produce a field profile which is shifted towards a coil end. This results in an increase in inductance which results in a decrease in inductive merit for a fixed efficiency. However, this trend was only noticeable for the X- and Y-gradient axes, and not the case for the Z-gradient axis. This was an unexpected result and may be due to the fact that there were less candidate coils for the 0.28 m cut-out as compared to the 0.14 and 0.21 m cut-outs. However, this does warrant further investigation.

Table 2-2: Selected Gradient Coils Merit Values

		IR_{offset}		
Gradient Axis		0.14 m	0.21 m	0.28 m
0.21 m cut-out				
X Gradient M_L (mT m ⁻¹ A ⁻¹ H ^{-0.5})		9.7 ± 0.9	8.0 ± 0.9	6.0 ± 0.8
Y Gradient M_L (mT m ⁻¹ A ⁻¹ H ^{-0.5})		8.7 ± 0.8	7.8 ± 0.6	6.9 ± 1.1
Z Gradient M_L (mT m ⁻¹ A ⁻¹ H ^{-0.5})		10.7 ± 1.1	12.0 ± 0.8	10.0 ± 0.9
		Cut-out Length		
Gradient Axis		0.07 m	0.14 m	0.21 m
0.14 m IR_{offset}				
X Gradient M_L (mT m ⁻¹ A ⁻¹ H ^{-0.5})		9.8 ± 0.8	8.8 ± 0.9	9.7 ± 0.9
Y Gradient M_L (mT m ⁻¹ A ⁻¹ H ^{-0.5})		8.8 ± 0.7	8.1 ± 0.7	8.7 ± 0.8
Z Gradient M_L (mT m ⁻¹ A ⁻¹ H ^{-0.5})		10.2 ± 1.1	10.2 ± 1.1	10.7 ± 1.1

Calculated gradient coil merit values for all successful candidate gradient coils with constant cut-out length (0.21 m) and imaging region offset (0.14 m). A clear decrease in performance is observed for the X- and Y-gradient axes as the imaging region is shifted towards the patient end.

Given the complexity of designing a high-performance gradient coil with shoulder cut-outs it was anticipated that moving the imaging region towards the patient end of the gradient would have a negative impact on performance. This was indeed determined to be the case. However, the decrease in performance as the imaging region was moved was most noticeable in terms of gradient inductance, observed in the drop-in merit value. Surprisingly, I did not observe a discernible trend in merit value as the cut-out length was made larger. This may be since the gradient coil length was not held constant and varied with each cut-out length change ultimately effecting the overall gradient length. This is important as adding cut-outs to a gradient coil without extending the length would be expected to have a negative impact on performance due to the decreased area over which current can flow.

When looking outside of the merit value and at all performance parameters the effect of adding cut-outs sees a performance increase in some cases which is clear when looking at the results in Figure 2-3 where there is an increase in DSV_{30} and shielding, as measured by the decrease in bore power) while the minimum wire spacing remains relatively the same. This is due to the addition of conducting surfaces and the trouble of designing short gradient coils. Therefore, by lengthening the gradient and allowing further room for current to flow there is a net benefit on the gradient performance regardless of the loss of the cut-out space along the shoulders. However, when looking at the case where the cut-out is held constant in Figure 2-4, and the imaging region is moved towards the patient end it is clear this comes with negative performance. This is true for traditional asymmetric gradient coils and is observed here. As the imaging region is moved forward the wires tighten around the shoulder cut-outs as the field is shifted to one side which is clear from the calculated bulk minimum wire spacing. The DSV_{30} also worsens as the imaging region has less current flow on each side of it and the gradient struggles to maintain the homogeneity. Further, shielding is decreased as is expected as the gradient becomes more asymmetric.

Overall, development of a high-performance gradient coil capable of imaging both the head and neck has many advantages over a head-only coil. One example is in evaluation of strokes. The majority (80%) of all strokes are ischemic strokes resulting from a blocked artery which supplies blood to the brain. This is primarily in the form of atherosclerosis resulting in fatty plaque deposits forming within the carotid artery. Imaging plays an important role in evaluating and identifying patients who require immediate intervention. A high-performance gradient can provide the capability to perform magnetic resonance angiography of both the neck and intracranial regions with high gradient strength for diffusion imaging. This is important for monitoring of arterial health as well as provides the possibility for imaging in a point-of-care scenario where time is paramount to save neuronal health. This style gradient coil has the potential to ultimately build the foundation for an all in one stroke imaging platform. There is at least one modern commercially-available head-only clinical scanner that employs high-strength gradients, but it does not use a shoulder cut-out geometry (12). The addition of a shoulder cut-out gradient to such a compact system may enable imaging further into the neck.

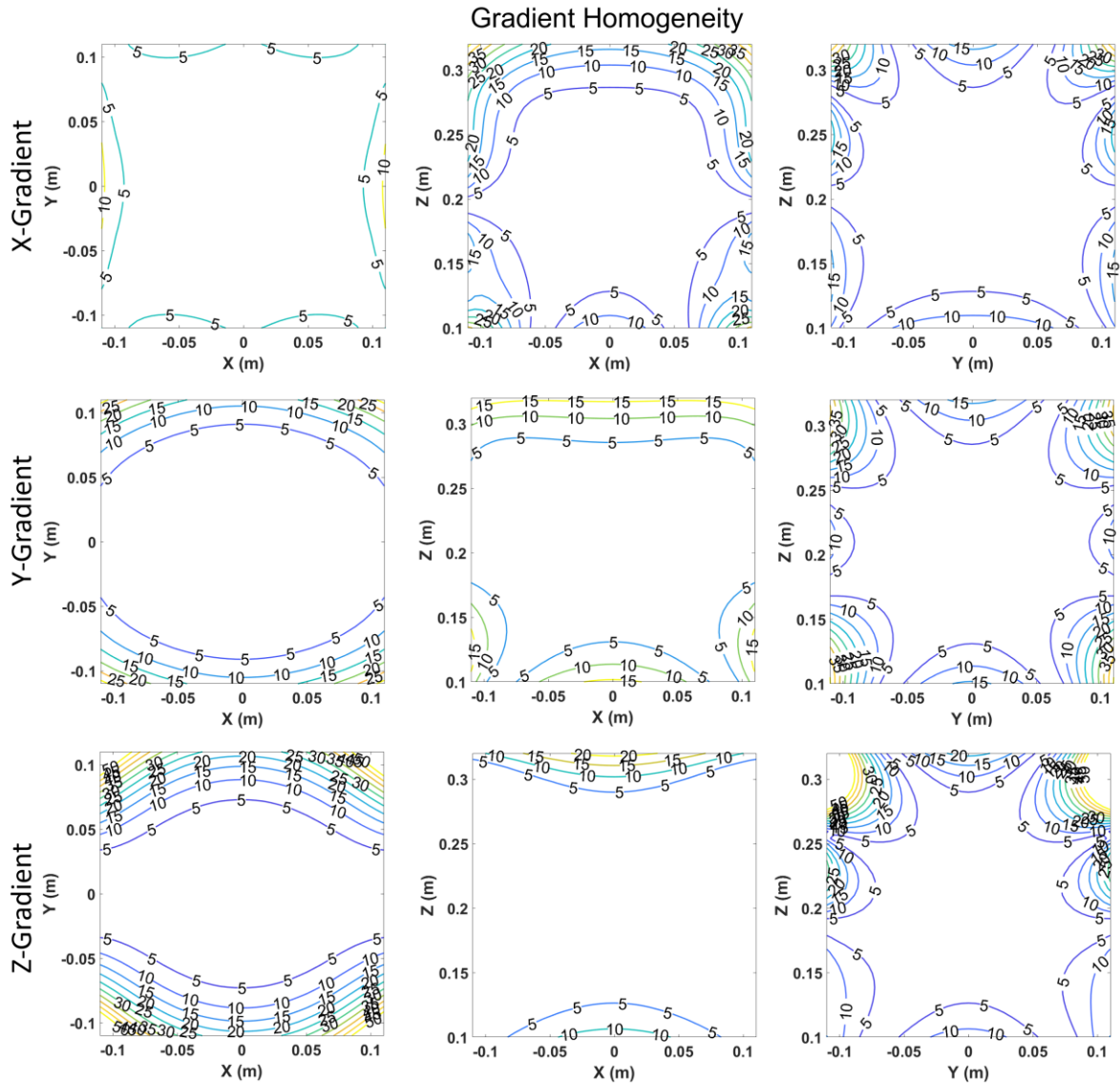


Figure 2-5: Selected Gradient Coil Homogeneity Plots

Simulated gradient coil homogeneity plots showing the percent deviation from central gradient field value contour lines across three planes for all three gradient axes.

A secondary application of this gradient coil design is in radiotherapy contouring. In treatment of head and neck cancers targeted radiotherapy applications require contouring of the tumour and surrounding tissues. Although MRI within the context of radiotherapy is a relatively new field, the multi-parametric capabilities of MR have provided valuable in terms of tumor delineation with diffusion (13) and improved soft tissue contrast. With the design of an all-in-one gradient coil capable of high-resolution imaging of both the head and cervical spine

treatment planning can be done using high quality imaging of both regions while taking advantage of non-contrast enhanced flow and diffusion measurements. This is important because visualization of important structures such as the Brachial plexus originating from the lower cervical spine are difficult to visualize on conventional treatment planning devices such as CT and may serve as a point-of-care head and neck system within a radiotherapy department, where a dedicated MRI capable of imaging these fine structures may be unavailable.

Although all gradient coils presented here provide fields suitable for imaging with appropriate electromagnetic properties there is some work which must be performed before any of them can be used in an actual MRI system. Primarily, it must be ensured that the gradient coil does not move or overheat during operation. This requires the wire pattern to be balanced for forces using realistic fields of which it will be subjected to. Another important consideration before the gradient coils presented here can be used clinically is in development of shoulder cut-out shim coils. For the final potted gradient coil to maintain slots for the shoulders the active shims must also have cut-outs. This can be accomplished using the BEM method, like how it is presented here, using a target field profile of spherical harmonics while accounting for the mutual inductance between the shim and gradient layers.

Another manufacturing issue that may arise is the loss of the Z-gradient in terms of cooling during operation. Traditionally, hollow copper wire is used for the z-axis which allows water to be run through cooling the gradient during operation (11). Research will be required to determine the optimal cooling configuration that minimizes heat build-up and avoids local hotspots.

The study presented here is not without limitations. Primarily, although the final designs derived here are balanced for torque during the design process, in order to ensure proper force balancing a realistic operational B_0 field would be required. This will result in small modifications in the wire patterns to ensure that there are no significant net forces when operating inside an actual field. Another limitation, touched on above, is the lack of shims into the design. They will ultimately need to fit within the already limited radial space available. Another important note is in the induced eddy currents within the bore surface.

Asymmetric gradient coils produce more complex eddy current patterns within the surrounding surfaces and the removal of current carrying surfaces, in the form of shoulder cut-outs, can increase this complexity. There does exist BEM approaches to limit the field produced by induced eddy currents however, these methods fail to account for the time evolution of the eddy currents which can introduce a sense of false shielding. Finally, initial calculations to build up the candidate gradient coil pool are calculated over a coarse mesh. This ensures a fast solution; however, it leads to slight differences in the calculated inductance and resistance between the final gradient coils (calculated using a finer mesh) and the entire candidate pool. Importantly, this is not a practical concern as the selection of the final gradient coil is made using the information from the coarse mesh and therefore there is no bias towards any gradient coil. The fine mesh is solely used to ensure smooth wire patterns and more accurate electromagnetic calculations for the final selected coils. It is also important to note that with the addition of shoulder cut-outs the patient or volunteer will be located further into the high-performance gradient coil. This may influence cardiac stimulation and PNS thresholds compared to a head-only gradient. One possible way to mitigate this would be the incorporation of a “head-mode” and “neck-mode” which modifies the maximum allowable slew-rate to limit stimulation. This will need to be explored experimentally.

This present study builds upon previous examples of MRI gradient coils for head and neck imaging. Although previous shoulder cut-out gradient coils have been constructed (6) or designed theoretically (4), this is the first study to examine the effects of cut-out length and imaging region location on performance. Future work will be on incorporation of active shims into the radial space available, balancing the design for forces within a realistic field, and exploring novel ways of assembling the gradient coil to account for the shoulder cut-outs. Once these engineering challenges have been overcome the final selected gradient coils, with any small design modifications, will be manufactured in-house. Once built, electromagnetic measurements (inductance, resistance, field profile..etc) will be performed to verify the design study and operational limits (for peripheral nerve stimulation) will be determined. The final constructed coil will be installed in our cryogen-free magnet housed within our lab. This will allow eddy current and thermal measurements to be performed to determine shielding performance as well as allow testing for imaging performance.

2.5 Conclusion

I have explored the effect of adding shoulder cut-outs of varying length to a head-only gradient coil while moving the imaging region towards the patient. I have also presented here a proposed design for a high-performance head and neck gradient coil which can be used as part of an all-in-one platform for a host of head and neck imaging applications from high resolution anatomical images to the demanding needs to functional brain imaging.

2.6 References

- [1] C. R. Gomez, “Editorial: Time is brain!,” *Journal of Stroke and Cerebrovascular Diseases*, 1993.
- [2] B. Zhang, Y.-F. Yen, B. A. Chronik, G. C. McKinnon, D. J. Schaefer, and B. K. Rutt, “Peripheral nerve stimulation properties of head and body gradient coils of various sizes,” *Magn. Reson. Med.*, vol. 50, no. 1, pp. 50–58, Jul. 2003.
- [3] R. A. Lemdiasov and R. Ludwig, “A stream function method for gradient coil design,” *Concepts Magn. Reson. Part B Magn. Reson. Eng.*, vol. 26B, no. 1, pp. 67–80, Aug. 2005.
- [4] M. Poole and R. Bowtell, “Novel gradient coils designed using a boundary element method,” *Concepts Magn. Reson. Part B Magn. Reson. Eng.*, vol. 31B, no. 3, pp. 162–175, Aug. 2007.
- [5] F. Tang et al., “A cone-shaped gradient coil design for high-resolution MRI head imaging,” *Phys. Med. Biol.*, vol. 64, no. 8, p. 085003, Apr. 2019.
- [6] M. Davids, B. Guérin, A. vom Endt, L. R. Schad, and L. L. Wald, “Prediction of peripheral nerve stimulation thresholds of MRI gradient coils using coupled electromagnetic and neurodynamic simulations,” *Magn. Reson. Med.*, vol. 81, no. 1, pp. 686–701, Jan. 2019.

- [7] T. K. F. Foo et al., “Highly efficient head-only magnetic field insert gradient coil for achieving simultaneous high gradient amplitude and slew rate at 3.0T (MAGNUS) for brain microstructure imaging,” *Magn. Reson. Med.*, p. mrm.28087, Nov. 2019.
- [8] C. T. Harris, W. B. Handler, and B. A. Chronik, “Electromagnet design allowing explicit and simultaneous control of minimum wire spacing and field uniformity,” *Concepts Magn. Reson. Part B Magn. Reson. Eng.*, vol. 41 B, no. 4, pp. 120–129, Oct. 2012.
- [9] C. T. Harris, D. W. Haw, W. B. Handler, and B. A. Chronik, “Shielded resistive electromagnets of arbitrary surface geometry using the boundary element method and a minimum energy constraint,” *J. Magn. Reson.*, vol. 234, pp. 95–100, Sep. 2013.
- [10] W. B. Handler et al., “Design and construction of a gradient coil for high resolution marmoset imaging,” *Biomed. Phys. Eng. Express*, vol. 6, no. 4, p. 45022, Jul. 2020.
- [11] W. B. Handler et al., “New head gradient coil design and construction techniques,” *J. Magn. Reson. Imaging*, vol. 39, no. 5, pp. 1088–1095, May 2014.
- [12] A. Panther et al., “A Dedicated Head-Only MRI Scanner for Point-of-Care Imaging,” in *Proc. Intl. Soc. Mag. Reson. Med.* 27, 2019.
- [13] P. Dirix, K. Haustermans, and V. Vandecaveye, “The Value of Magnetic Resonance Imaging for Radiotherapy Planning,” *Seminars in Radiation Oncology*. 2014.

Chapter 3

3 The X-Mode Gradient Coil Configuration

This chapter is an expanded version of the two following peer-reviewed conference abstracts:

Eric J. Lessard, William B. Handler, and Blaine A. Chronik. *The X-Mode Gradient: Improved Performance for Select Applications*. International Society for Magnetic Resonance Imaging Annual Meeting 2020.

Eric J. Lessard, William B. Handler, and Blaine A. Chronik. *Development of an MRI Gradient Coil for Use in a Compact Head-only MRI Platform Capable of Imaging C7 and Below*. American Association of Physicists in Medicine and Canadian Organization of Medical Physicists Joint Annual Meeting 2020.

3.1 Introduction

The drive for higher performance gradient coils has come with an increased use of more complex designs. These include head-optimized scanners which utilize asymmetric gradient coils (1) and unique geometries like gradient coils with shoulder cut-outs (2,3). Shoulder cut-out gradient coils provide a unique design to further enable patient entrance into the bore. One example was demonstrated in Poole and Bowtell's 2007 paper (2) where they designed an unshielded shoulder slotted gradient coil as a proof of concept and observed a difference between their X- and Y-gradient axis of 17% lower efficiency, 45% tighter wire spacing, and 14% higher resistance, when inductances are matched. Looking at the figure of merit, a numerical value to compare gradient coil performance showed a 40% decrease from the Y-gradient for the X-gradient. In addition to this, Siemens has designed both the clinical AC84 and experimental AC88 head-gradient coils which incorporate varying degrees of cut-outs in their design. Shvartsman et al. explored the design of an unshielded shoulder cut-out gradient coil (4) for head imaging however, in this proof-of-concept design technique paper they demonstrated the utility of their technique by designing an unshielded single axis gradient coil. While they explored some of the trade-offs of incorporating shoulder cut-outs such as the complexity of the induced

eddy current profile, they did not compare performance between the transverse axes. The high-performance MAGNUS gradient (5) utilizes a stepped bore which is analogous to a shoulder cut-out style in terms of increasing patient access. The C3T-HG (6) has a stepped gradient design which enables imaging into C2-C3 junction with its 0.26 cm imaging region extending to the edge of the step. These shoulder slotted and stepped gradients are designed for head imaging and fail to provide imaging further into the neck. Previously (7) I have proposed the use of a similar style actively shielded gradient coil for head and neck imaging in which the imaging region is moved further into the cut-out area. In my previous work I noted the difficulty in balancing the transverse axes performance as was seen in (2). In this work with fixed efficiencies of 0.125 mT/m/A and 0.150 mT/m/A for the X- and Y-gradients we observed a difference in inductive merit value of 7%, 54% tighter wire, and an 8% decrease in imaging region size. This is due to the location of the X- and Y-gradient producing wire patterns relative to the location of the shoulders. When conducting surfaces are removed on the left and right of the gradient coil surface this disproportionately affects the X-gradient and has a limited effect on the Y-gradient.

Head-optimized scanners operate with small inner radii with entrance into the bore limited by the small size of the head-gradient coil. This limits patient access limiting imaging to the head and does not provide imaging of the neck. Asymmetric head gradients use imaging regions which are shifted towards the patient end of the gradient coil instead of at the geometric center. An asymmetric shoulder cut-out gradient coil with the imaging region extending slightly into the cut-out region would provide a unique ability to image both the head and neck in a compact head-only scanner. This would have applications in point-of-care MRI where brain and cervical spine imaging provide important diagnostic information used for triaging. As mentioned, previous investigations and current implementations of shoulder cut-out gradient coils are limited to head imaging only and do not provide imaging down into the cervical spine.

In this work I propose the design of a shoulder cut-out gradient coil producing linearly varying magnetic fields along the diagonals as opposed to the X- and Y-axes. I denote these new gradients as the d_1 - and d_2 -gradients. In this proof-of-concept study aimed to demonstrate the feasibility of this rotated design and hypothesized that by rotating the

gradient axes I could design a set of balanced transverse gradient coils for head and neck imaging in a compact MR platform. I demonstrate the utility of this configuration by extending the imaging region into the cut-out portion to enable imaging further into the neck.

3.2 Methods

3.2.1 Design Methods

Using in-house electromagnetic software written in MATLAB I derived wire patterns for asymmetric d_1 - and d_2 -gradient (orientations shown in Figure 3-1) electromagnets through the boundary element method (2, 8-10). In this method a current density over a discretized surface is represented as a stream function flowing on that surface. Using a target field approach the stream function is solved for which produces the magnetic field targets as constrained by a minimization functional. I used a performance functional accounting for deviation from the target field points, power deposited into a representative computational bore, dissipative power within the gradient coil, and force/torque balancing. The field targets were linearly varying X- and Y-gradient fields rotated by 45 degrees, the representative bore surface had a radius of 0.30 m and a length of 1.0 m with end flanges and the force/torque balancing was done using measured field data from an in-house superconductive cryogen-free head-optimized magnet. This functional is as follows:

$$U = \frac{1}{2} \sum_{k=1}^K [B_z(r_k) - B_z^{\text{tar}}(r_k)]^2 + \frac{\beta}{2} P + \frac{\gamma}{2} P^{\text{cryo}} - \lambda_x M_x - \lambda_y M_y - \lambda_z M_z - \lambda_x F_x - \lambda_y F_y - \lambda_z F_z \quad (3.1)$$

$B_z(r_k)$ and $B_z^{\text{tar}}(r_k)$ are the produced and target magnetic field values at the design point r_k , β is the dissipative power weighting, P is the gradient power term, γ is the bore power weighting, P^{cryo} is the bore power term, λ is a Lagrange multiplier term corresponding to the torque (M) and force (F) balancing. In detail the first term describes the least-squares difference between the produced magnetic field and ideal and represents the importance of homogeneity. The second term describes the power dissipated within the gradient coil through Joule Heating and represents power loss. The third term describes the

power dissipated in a nearby conducting surface, in this case a representative bore, via the induced eddy current and represents a measurement of shielding. The final terms are Lagrange Multipliers responsible for constraining our forces and torques such that they are balanced during operation.

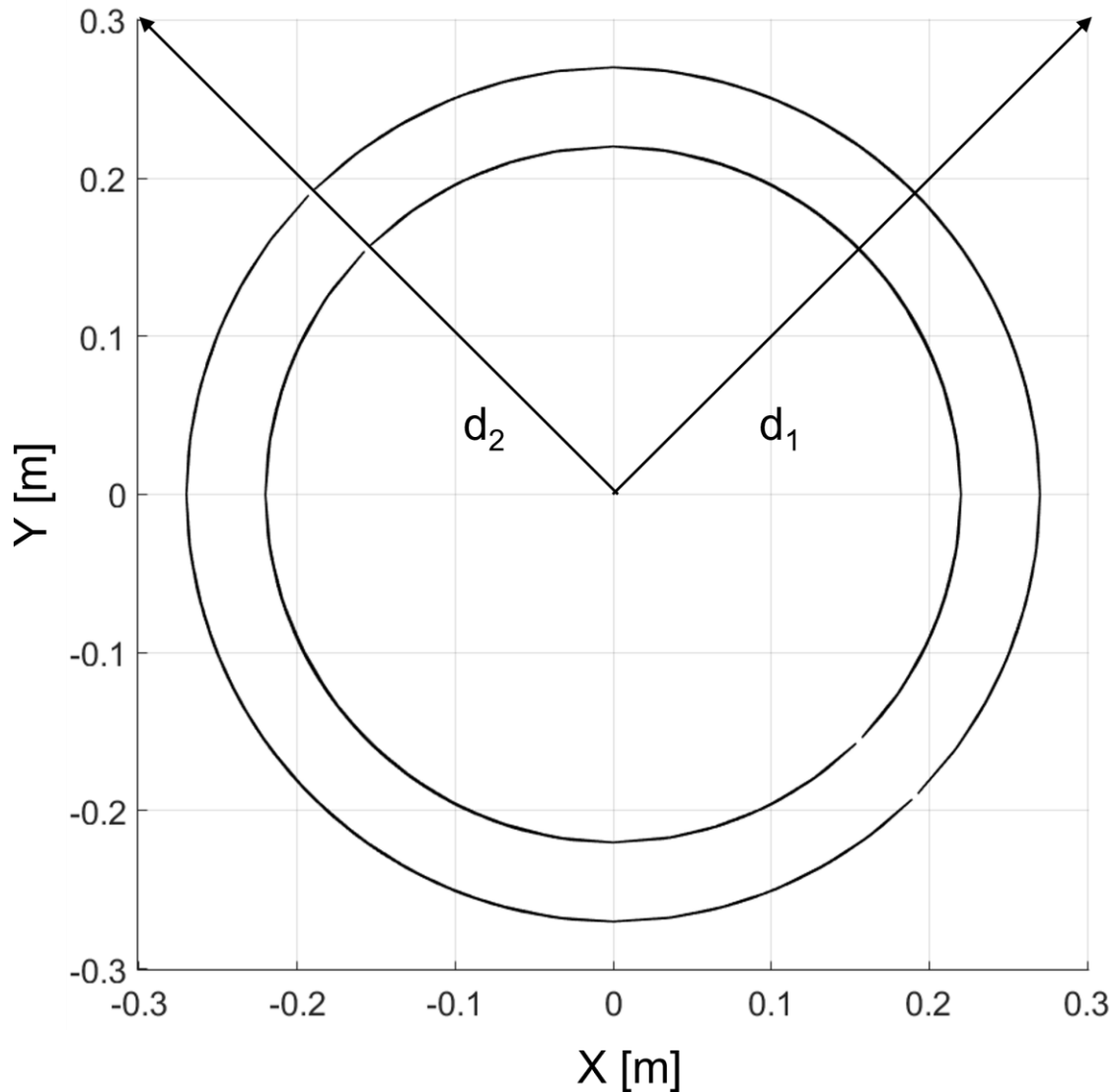


Figure 3-1: d_1 - and d_2 -gradient axes

Example gradient coil surfaces (primary surface = smaller circle, shielding surface = outer circle) showing the rotated d_1 and d_2 reference frame.

To select final gradient coils a grid search was performed by varying the design performance functional, specifically the β and γ values controlling the relative importance

of field homogeneity, dissipative power, and shielding. I made small modifications to the design geometry from our previous work (7), which explored a shoulder cut-out gradient coil with traditional gradient axis orientation and here I designed the primary and shield surfaces based on 95 percentile US adult sizes. The primary (shield) surfaces for the d_1 - and d_2 -gradients, had radii of 0.22 m (0.27 m), 0.23 m (0.28 m), respectively. The primary axis of each had a cut-out height of 0.15 m and a length of 0.225 m whereas the shield surface had no cut-out as it was designed to fit outside of the shoulder breadth. The target field region was defined as a 0.20 m sphere situated at the geometric centre. The primary surface ran from $z = -0.4$ to 0.3 m for a total allowable length of 0.7m and the shield surface from $z = -0.45$ to 0.45 m for a total allowable length of 0.90 m. This configuration was designed to allow the imaging region to partially extend into the cut-out region for neck anatomical targets. The geometry of the total system was designed to fit within a 0.6 m diameter, 1.0 m long cryogenic bore. An example meshed surface is shown in Figure 3-2 this figure shows the primary inside surface highlighted in red for visibility and shows an example 0.2 m imaging region in blue.

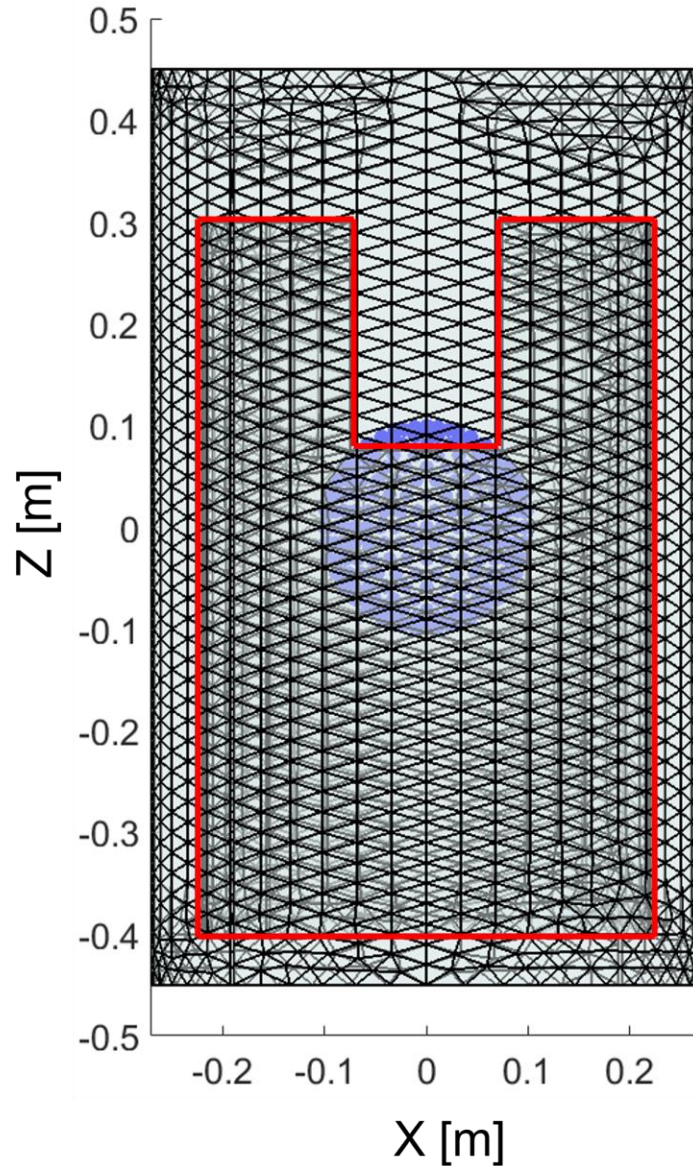


Figure 3-2: X-Mode Computational Mesh

Sample computational mesh used in this study with the inner (primary) surface highlighted in red showing the smaller diameter and shoulder cut-out. Blue sphere shows discretized imaging region used in design calculations.

Once the stream function over the surface is known it is contoured in 3D space to derive a wire pattern which best approximates the stream function over the surface. With the stream function and wire pattern solved for it is simple to calculate performance parameters such as: W_{\min} – the minimum wire spacing, calculated using the stream function contours; DSV_{20} – the diameter of a spherical volume where the gradient field varies <20% from the

central field value; efficiency – the gradient field produced per unit current; resistance – calculated using the resistivity of the material and the wire pattern; inductance – calculated using the wire pattern geometry; slew rate- calculated using the efficiency, inductance, resistance and amplifier information; and bore power – calculated using the induced stream-function in the bore surface and its induced power.

To maintain the ability to construct the finalized gradient from the candidate pool a subset of candidates with a W_{\min} of greater than 0.004 m was made. This was based on the wire intended to be used plus tolerances in the manufacturing process. Two other subsets were determined based on a minimum efficiency of 0.1 mT/m/A and a minimum linearity of a DSV_{20} of 0.15 m. From this, the intersection of the three sets was determined to find the candidates which meet the requirements. Since it is difficult to determine the shielding metric in which appropriate shielding has been achieved from this set the selected coils are the ones with the minimum bore power.

3.2.2 Analysis

In addition to using the induced eddy current in the bore surface for the purpose of shielding by minimizing the power deposition this eddy current can be used to calculate the magnetic field of this induced current. To evaluate the complexity of the induced eddy currents both the gradient coil and the induced eddy current on the computational bore surface were decomposed into spherical harmonics.

To explore heating, I calculated the required current through the gradient axes which leads to a 30-degree temperature rise in cooling water. The water was assumed to run through hollow wire of 4 mm with a variable inner diameter. I varied the inner diameter from 1 mm to 3.994 mm in 500 steps and for each configuration calculated the total resistance of the wire based on the cross-section and length. Using the inner diameter, the flowrate was solved for using the Darcy-Wesibach equation (11) assuming a pressure drop across the gradient coil of 3 atm. With the flowrate and resistance information the current required for a 30 degree temperature rise was calculated. A technique employed to increase the cooling capacity of gradient coils (12) is to break the continuous section of wire into

parallel sections and as such I performed this for the total gradient length (L), half gradient length ($L/2$), quarter gradient length ($L/4$), and eight gradient length ($L/8$).

3.3 Results

Electromagnetic performance parameters for the d_1 - and d_2 -gradient coils are given in Table 3-1 with their corresponding wire patterns shown in Figure 3-3. Magnetic field maps are shown in Figure 3-4. The gradient and eddy current magnetic field profile spherical harmonic decomposition is shown in Figure 3-5. Gradient field homogeneity plots are shown in Figure 3-6. The current required to induce a 30 °C temperature change in the cooling water as a function of wire inner diameter is given in Figure 3-7.

3.4 Discussion

In this work I explored the design of a shoulder cut-out gradient coil that I have named the X-Mode Gradient Configuration whereby the X- and Y-gradient axes are rotated by 45° creating d_1 - and d_2 -gradients to improve transverse axis performance in a shoulder cut-out configuration. I designed the gradient coils to have an imaging region extending into the shoulder cut-out region allowing head and neck imaging in a compact scanner. Throughout this work I observed the following: 1) the X-Mode configuration is a method of designing an actively shielded gradient coil for head- and neck-imaging which balances the transverse axis performance 2) the strongest harmonic in the eddy-current field is a ZX term, and 3) potential improvements include better torque balancing.

Table 3-1: X-Mode Gradient Performance Parameters

	d1-Grad	d2-Grad
Primary Radius [m]	0.22	0.23
Shield Radius [m]	0.27	0.28
DSV ₂₀ [cm]	25.5	23.5
DSV ₃₀ [cm]	28.5	26.0
Efficiency [mT/m/A]	0.1	0.1
Inductance [μ H]	142	133
Resistance [m Ω]	134	132
Bore Power [AU]	2.8E-5	1.2E-5
Minimum Wire Spacing [mm]	4.1	4.2
Slew Rate [T/m/s]	527	568

DSV₂₀ = diameter of spherical volume where the gradient field deviates <20%, DSV₃₀ = diameter of spherical volume where the gradient field deviates <30%.

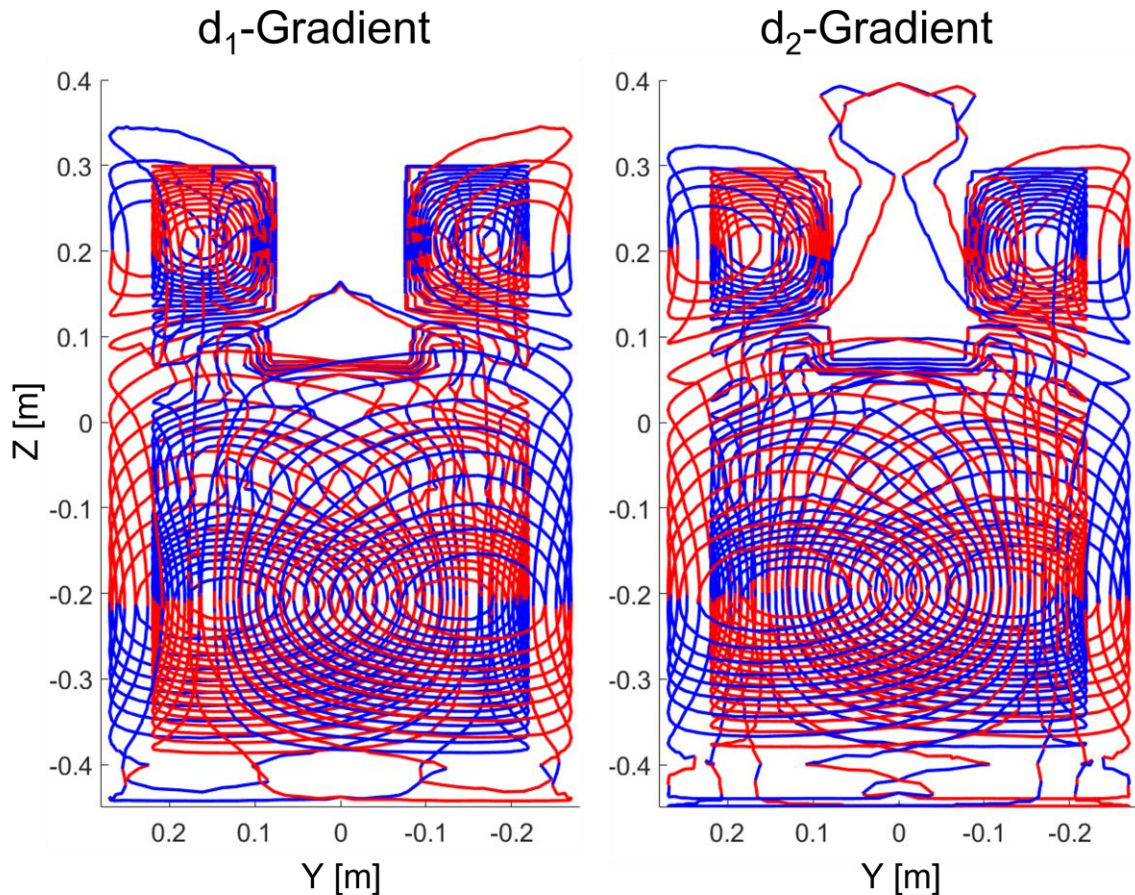


Figure 3-3: X-Mode Gradient Wire Patterns

Derived wire patterns for the X-Mode transverse gradients with colour indicating the direction of current flow with respect to the azimuthal direction.

The high homogeneity of the achieved designs with DSV_{20} values of 25.5 and 23.5 cm for the d_1 - and d_2 -gradient axes is promising for enabling lower cervical spine imaging in a platform such as this. The target imaging region of 20 cm was designed to allow overhang of the imaging region into the shoulder cut-out region and the designs have acceptable inhomogeneity extending even further into the cut-out region. Previous gradient coils such as the C2T-HG (6) had imaging regions that reach the tip of the stepped surface which allowed imaging into the C2-C3 junction. With an assumption that the mean cervical vertebrae size is approximately 1.1 cm the remaining four vertebra would extend approximately 4.4 cm further into the cut-out space (13). In this work the DSV_{20} extends 5.25 cm and 4.25 cm into the cut-out region whereas the DSV_{30} extends 6.5 cm and 5.5 cm into the cut-out region for the d_1 - and d_2 -gradients, respectively. Looking at the extreme

end of the homogeneity both gradient axes have DSV_{50} values of 30.5 cm which extends 7.75 cm into the cut-out region. While it may be impractical to image in regions extending into that DSV_{50} edge case advances in gradient unwarping and image reconstruction techniques enable improved imaging in cases of known gradient inhomogeneities. With the <5 cm of imaging region required to extend into the shoulder cut-out region to potentially cover to the C7 space the DSV_{30} of the presented coils presents an appropriate imaging region size to enable lower cervical spine imaging. In addition to the benefit of cervical spine imaging performance there is a gain in the application of brain imaging by having the homogeneous field extend into the shoulder cut-out region in that when the patient is positioned with the brain at the isocenter the important anatomical structures of the brain remain within a high homogenous region covering the entire brain. Combining this, if the aim is for a 25 cm imaging region which would extend 5 cm into the cut-out then the d_1 - and d_2 -gradients have inhomogeneities over this imaging region of 23% and 27%, respectively. Figure 3-4 shows gradient homogeneity plots with contour lines showing the deviations from the central gradient field in percent. The red line at $z = 7.5$ cm illustrates the z location of the shoulder cut-out and the extent of the patient entrance where the shoulders contact the surface.

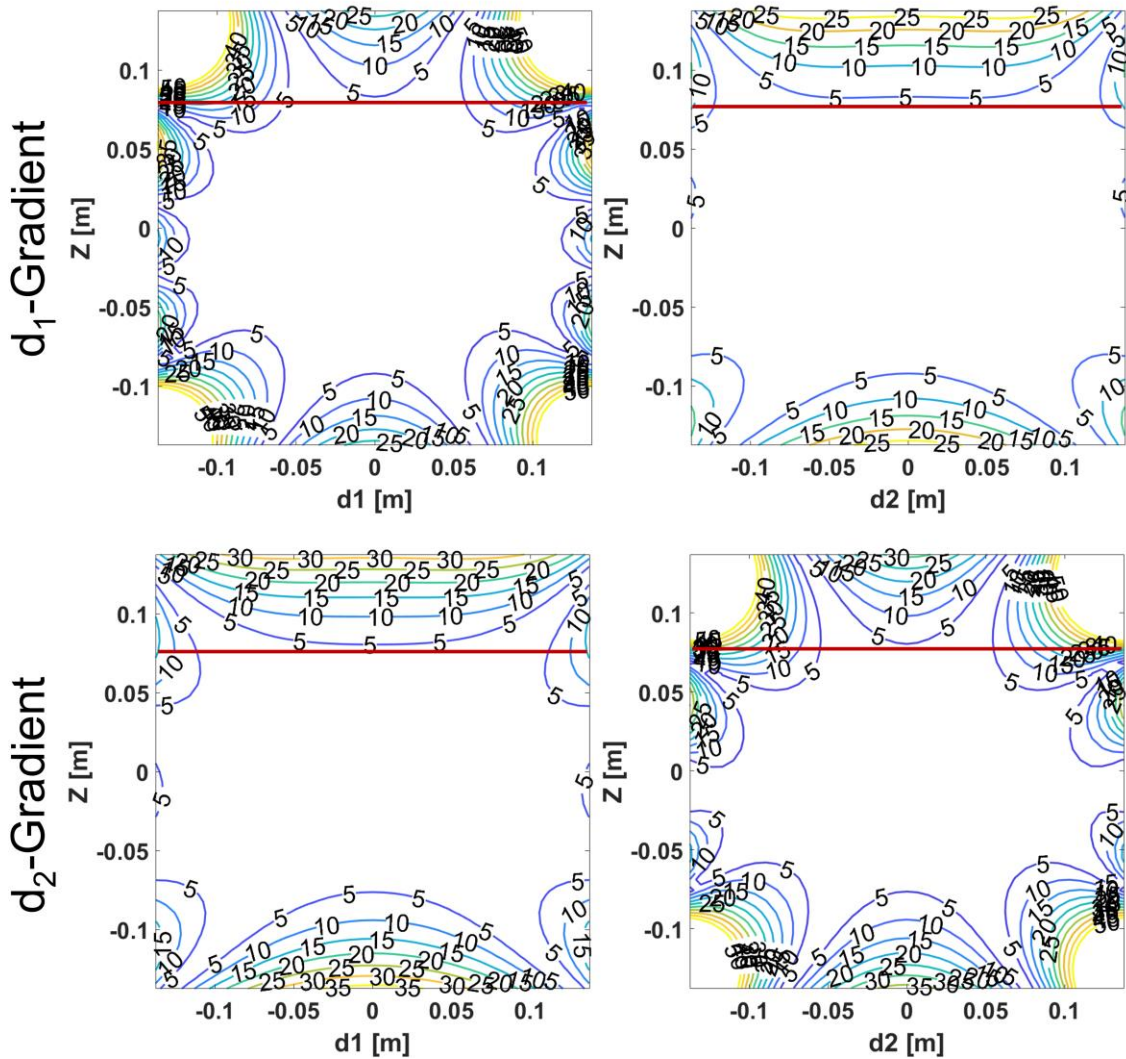


Figure 3-4: X-Mode Gradient Coil Homogeneity Plots

Simulated homogeneity plots with contour lines showing the percent deviation from the central gradient field value over representative planes. Red lines show the location of the shoulder cut-out surface.

Many gradient performance metrics such as the efficiency, linearity, and shielding are independent of the choice of amplifier. However, it is important to acknowledge the role of the amplifier in gradient performance with the maximum gradient strength and slew rate achievable being dependent on the choice of amplifier. While modern gradients have increased in performance this has been matched by an increase in amplifier capabilities. In this work, I calculated maximum gradient strength and slew-rate assuming a 900 A, 2100 V high-performance amplifier. It is important to note that these high currents will lead to large Joule heating potentially limiting the duty cycle at which this could be run, to help

mitigate that using all-hollow wire for both axes would greatly increase the cooling capacity. I explored this by calculating the current required to raise cooling water by 30 degrees as it runs through for various inner diameter wire for the 0.004 m wire anticipated

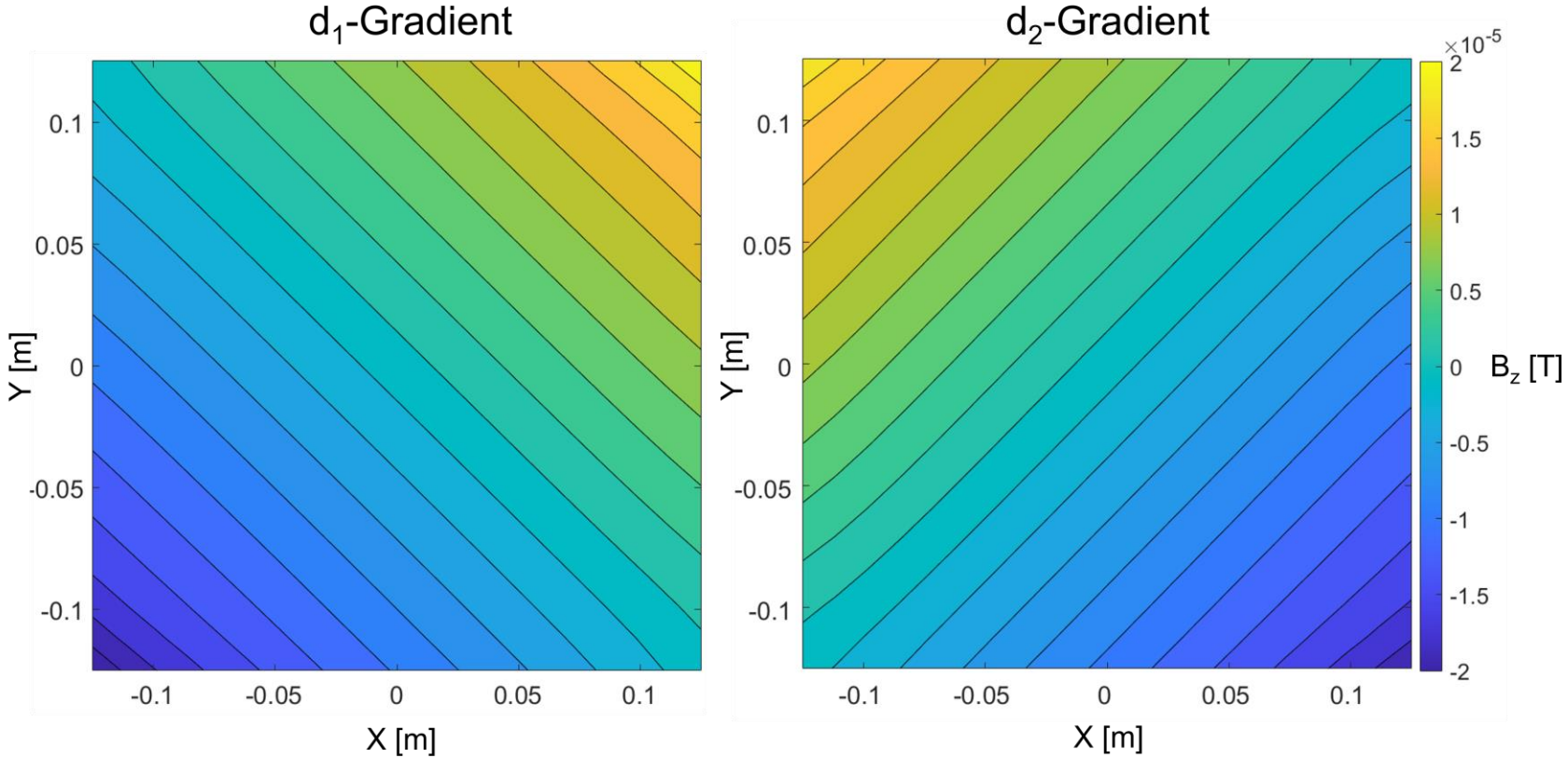


Figure 3-5: X-Mode Gradient Field Plots

Simulated magnetic field profiles for the d₁- and d₂-gradients. Current running through the coils is 1A.

to be used in the design of coil such as these. As expected, parallelization of the cooling line increases the maximum current. It should be noted that this simplified parallelization situation assumes constant pressure across each segment and gives a good approximation but is not the complete picture. However, these results indicate that construction of the gradient coils presented here should use 0.003 m inner diameter wire to maximize the cooling capability of an all hollow design. It is important to note that parallelization of the wire pattern may be tricky but at minimum breaking it into two halves is easy to accomplish and provides a benefit in cooling capabilities making it worthwhile.

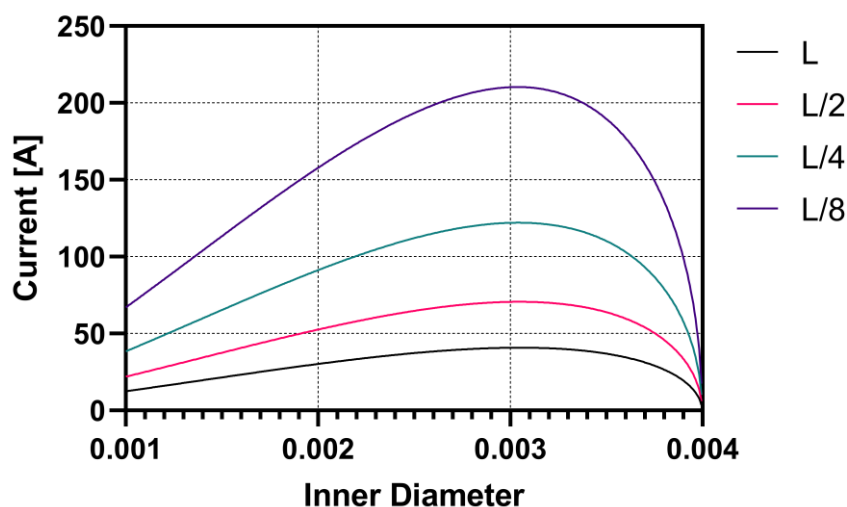


Figure 3-6: Inner Wire Cooling Analysis

Plot of current required to produce a 30 degree temperature change in cooling water across a range of inner diameter wire sizes for 4 gradient coil lengths.

It is known that as the gradient coil configuration moves away from symmetry the complexity of the induced eddy current increases. Shielded symmetric gradients have less complex eddy currents than those induced by shielded asymmetric gradients. Previous work has demonstrated the increased complexity of the eddy currents induced by a symmetric shoulder cut-out gradient axis (4). In this work, with the rotated gradient axes coupled with the shoulder cut-out geometry I sought to explore the complexity of the induced eddy current field by examining the stream function profile induced on the computational bore surface. Both gradients induced eddy current fields with predominant

ZX field components. The d_2 -gradient had approximately half of the fit coefficient of the d_1 -gradient. This is interesting and may be evidence of the increased shielding as seen in the bore power reduction between the axes. Although it should be noted that although it is lower, both axes are extremely well shielded compared to other designs within the study. In both cases the eddy currents also had significant X and Y components which is to be expected from the induced eddy currents as they will contain predominant terms on the order of the produced field which has primary X and Y components which can be compensated using gradient compensation. However, this additional ZX term will remain post compensation and either affect imaging or require additional steps to handle. Additionally, asymmetric gradient coils are typically not symmetrically torque balanced. Acceptable levels of total force and torque are 200 N and 75 Nm for each gradient axis (3). In order to evaluate the force and torque balancing I calculated the forces and torques on the gradient coils at an operational current of 900 A, the absolute maximum based on the chosen amplifier configuration. At this high current the d_1 -gradient was below these thresholds for both total force and torque however, unfortunately the d_2 -gradient has torque as high as 92 Nm. The d_2 -gradient is below these thresholds when the current is below 733 A.

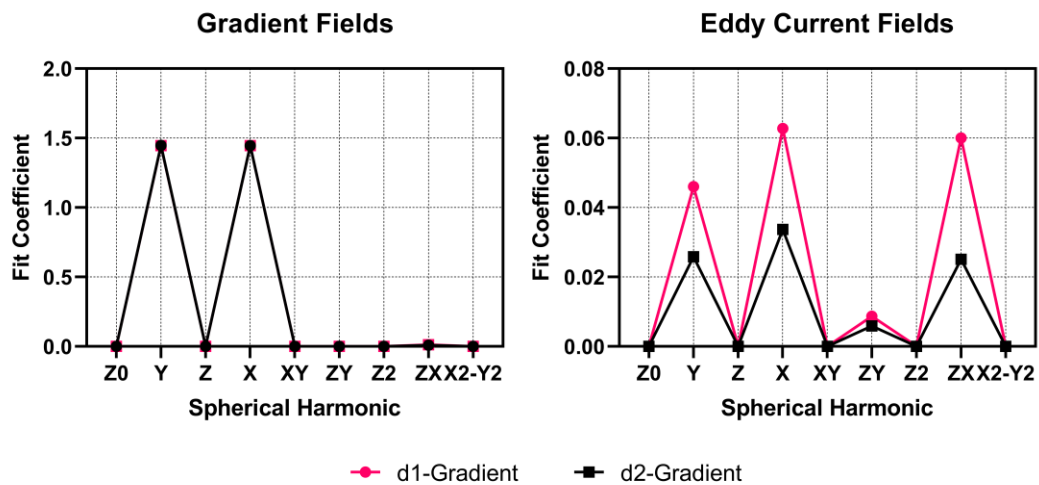


Figure 3-7: X-Mode Gradient Eddy Current Analysis

Spherical harmonic decomposition of the simulated gradient magnetic field and the induced eddy current magnetic field.

Future work should be focused on development of a complimentary set of spherical harmonic active shims to fit within the compact gradient housing. These spherical harmonic shim coils consist of layers of low-power electromagnets of which each is designed to produce a particular spherical harmonic field profile over the imaging region. In a setup like presented here where the inner coils have shoulder cut-outs and the outer coils have a full cylinder it would be beneficial to explore the relative trade-offs between where to put the shim coils and this is currently on-going work. Evaluation of the electric field of these presented coils would be useful for investigating the potential PNS limits in a system such as this. Previous work has explored E-field measurements of a similar setup (14) but it is important with the imaging region extending further towards the cardiac region.

It is important to note that this study is not without limitations. While the chosen geometries were based off the findings of previous work it is impossible to try the infinite number of primary and shield surface lengths, ordering and radii. As such, a decision was made to place the radii of the primary and shield surfaces dependent on percentile information. This already will limit the population that will fit within a gradient coil such as this. Next, the evaluation of hollow wire cooling performance is a simplistic case and may benefit from further simulations. However, the relative results presented here provide motivation for a further study and provide a first step in optimal wire selection. Finally, the chosen geometries in this work make a direct comparison with our previous shoulder cut-out gradient impractical. This is due to the variation in gradient coil radii and cut-out lengths which will significantly impact the final designs. Further, the gradient efficiencies in our previous work were different between the X- and Y-gradients and in this work they were equal. A rough comparison can be made and, in this work, although the d_1 -gradient had up to 10% better imaging region homogeneity compared to the d_2 -gradient, as measured by DSV, the gradients were effectively matched for efficiency, resistance, wire spacing, and slew-rate. Whereas in the previous work the X-gradient had a 7.5% smaller DSV_{30} , 17% lower efficiency, 5% lower resistance, 47% tighter minimum wire spacing, and 6% higher slew-rate compared to the Y-gradient. Important to note the differences observed in this previous work in resistance, wire spacing, and slew-rate would be worse if the wire density of the X-gradient was increased to match the Y-gradient efficiency. It may be worth

performing additional explorations by designing an X-Mode gradient coil with geometry and an image region location that matches a literature study. This would allow direct comparison to a previously reported coils performance and is a limitation of this study.

3.5 Conclusion

In this proof-of-concept study I have demonstrated the feasibility of designing a rotated transverse gradient coil configuration to improve the balance between axis performance within a shoulder cut-out system. I have shown the benefit of using an asymmetric design where the imaging region extends into the cut-out portion enabling cervical spine imaging within a compact inner radius.

3.6 References

- [1] Turner R: Gradient coil design: A review of methods. *Magn Reson Imaging* 1993; 11:903–920.
- [2] Poole M, Bowtell R: Novel gradient coils designed using a boundary element method. *Concepts Magn Reson Part B Magn Reson Eng* 2007; 31B:162–175.
- [3] Eberlein E, Schmitt F, vom Endt A, Kimmlingen R, Riegler J: A high-performance head gradient coil for 7T systems. *Proc 14th Sci Meet Int Soc Magn Reson Med* 2006; 11:1370.
- [4] Shvartsman S, Steckner MC: Discrete design method of transverse gradient coils for MRI. *Concepts Magn Reson Part B Magn Reson Eng* 2007; 31B:95–115.
- [5] Foo TKF, Tan ET, Vermilyea ME, et al.: Highly efficient head-only magnetic field insert gradient coil for achieving simultaneous high gradient amplitude and slew rate at 3.0T (MAGNUS) for brain microstructure imaging. *Magn Reson Med* 2020; 83:2356–2369.
- [6] Foo TKF, Laskaris E, Vermilyea M, et al.: Lightweight, compact, and high-performance 3T MR system for imaging the brain and extremities. *Magn Reson Med* 2018; 80:2232–2245.
- [7] Lessard EJ, Handler WB, Chronik BA: Preliminary Design Exploration for a Head

and Neck Gradient Coil: Effect of Shoulder Cut-out Length on Performance. *Proc Intl Soc Mag Reson Med* 27 2019.

[8] Peeren GN: Stream function approach for determining optimal surface currents. *J Comput Phys* 2003; 191:305–321.

[9] Lemdiasov RA, Ludwig R: A stream function method for gradient coil design. *Concepts Magn Reson Part B Magn Reson Eng* 2005; 26B:67–80.

[10] Harris CT, Handler WB, Chronik BA: Electromagnet design allowing explicit and simultaneous control of minimum wire spacing and field uniformity. *Concepts Magn Reson Part B Magn Reson Eng* 2012; 41 B:120–129.

[11] Brown G (Oklahoma SU: ENVIRONMENTAL AND WATER RESOURCES HISTORY 34 The History of the Darcy-Weisbach Equation for Pipe Flow Resistance Glenn O. Brown 1. *Enviornmental Water Resour Hist* 2002:34–43.

[12] Handler WB, Harris CT, Scholl TJ, et al.: New head gradient coil design and construction techniques. *J Magn Reson Imaging* 2014; 39:1088–1095.

[13] Prameela MD, Prabhu L V., Murlimanju B V., Pai MM, Rai R, Kumar CG: Anatomical dimensions of the typical cervical vertebrae and their clinical implications. *Eur J Anat* 2020; 24:9–15.

[14] Halder AA, Lessard EJ, Handler WB, Chronik BA: Gradient induced electric field within a shoulder cut-out gradient coil built for head and neck imaging. *Proc Intl Soc Mag Reson Med* 29 2021.

Chapter 4

4 Shoulder Cut-out Active Shim Set Design

This chapter is an expanded version of the peer-reviewed conference abstract:

Eric J. Lessard, William B. Handler, and Blaine A. Chronik. *Spherical Harmonic Active Shim Set Design for a Shoulder Cut-out MRI Platform*. International Society for Magnetic Resonance Imaging Annual Scientific Meeting 2022.

4.1 Introduction

A highly homogeneous magnetic field is crucial for high-performance magnetic resonance imaging (MRI). Many aspects can contribute to field inhomogeneity with two primary ones being the affect of material inside the magnetic environment and induced eddy currents and their respective magnetic fields. Active shimming is a method of correcting for inhomogeneities in the magnetic field profile due to macroscopic magnetization of samples placed in the field. This can be done once per imaging volume or dynamically where the optimal shim setup changes on a slice-by-slice basis (1,2). Eddy currents are minimized by employing actively shielded gradient designs but ones that persist are handled through gradient preemphasis. Shimming the magnetic field is done using either a dedicated set of individual electromagnets which produce spherical harmonic fields or using multi-channel matrix arrays. In asymmetric gradient systems like head-optimized scanners the eddy current field may have higher order terms which cannot be compensated using gradient compensation alone. This has motivated work exploring the use of the active shim coils in compensating for these residual higher order terms. These exist in situations where the symmetry of the gradient coil is broken such as those found in asymmetric designs but also non-cylindrical geometries such as a shoulder cut-out platform.

Both shimming and higher order dynamic eddy current compensation uses independent resistive shim coils of which each approximates a spherical harmonic. These shim coils can be designed as an insert or incorporated within the gradient coil structure and can be implemented like gradient coil compensation to cancel out the induced eddy current magnetic field. Other methods of shimming include multi-coil shim arrays composed of an

array of independently driven circular loops (3). As opposed to being designed to produce a single spherical harmonic, the array is driven with an appropriate current profile which in turn corrects for the inhomogeneities in the magnetic field. This allows quick and efficient dynamic shimming in real-time. These sorts of methods play an important role in high-field MRI due to the large effect that inhomogeneities have on the image quality. However, they can also be used to compensate for eddy currents in the same way as resistive shim sets.

Design of electromagnets such as active shims is a multi-stage computational process with many factors which must be considered to design the best electromagnet for the job. One significant consideration in the design is the radius at which the electromagnet will be placed as it plays an important role in performance. This is due to the various scaling relationships that govern spherical harmonic electromagnet design (4).

With this the efficiency of an electromagnet η , defined as magnetic field per unit current, is proportional as follows:

$$\eta \propto \frac{1}{r^{n+1}} \quad (4.1)$$

Where η is the efficiency, r is the electromagnet radius, and n is the field order (1 for gradients, 2 for 2nd order shim coils).

For dynamic applications the benefit in slew-rate is even larger with it proportional as:

$$SR \propto \frac{1}{r^{n+2}} \quad (4.2)$$

Whereas in general electromagnet resistance and inductance will scale as:

$$L \propto r \quad (4.3)$$

$$R \propto r \quad (4.4)$$

This makes selection of the radius important in the design stage as too large of a radius will lead to a decrease in coil performance however physical entrance into the coil is prohibited

with too small of a radius. Typically, the shim radius is governed by the other electromagnets and their respective geometries. The gradient coil must fit within the main magnet bore and the resistive shims must either fit within the gradient housing or in the case of an insert coil must fit inside the remaining bore space. In head-optimized scanners this real estate is at an even greater premium as radial space is already limited. Previously, I have proposed the design of a shoulder cut-out (SCO) actively shielded gradient coil for head and neck imaging (5,6). In this, the primary windings consist of partial cylinders with rectangular shoulder cut-outs to allow further entrance into the coil whereas the shield windings are located further away and outside of the typical bideltoid shoulder breadth.

For an active spherical harmonic shim set for use in a system such as this the shims can be placed with either the primary windings (requiring a shoulder cut-out) or the shield windings (complete cylinder). In this work I present the designs of spherical harmonic shims with and without shoulder cut-outs at different design radii with a focus on performance evaluation through efficiency and field homogeneity. I hypothesize that while the shoulder cut-out shim set will see an increase in magnetic field efficiency this will be at a cost of field homogeneity due to the removal of conducting surface by the shoulders.

4.2 Methods

4.2.1 Design Methods

An in-house MATLAB function was used to generate computational meshes for use in an in-house boundary element method (BEM) software. Two sets of meshes were generated with different radii: 0.27 m for fitting outside of the bideltoid shoulder breadth and 0.25 m to fit overtop the typical biacromial shoulder breadth just outside from the acromia. The shoulder cut-out shim set was designed on a computational surface of $r = 0.25$ m with a square cut-out of 0.225 m along Z and 0.15 m along Y. The cut-out was achieved not by removing portions of the mesh but by setting the resistivity of the surface within the cut-out region such that the cost associated with placing current elements in that region is too high and the algorithm places no current there resulting in no wires when contoured. The full cylinder shim set was designed on a computational surface of $r = 0.27$ m. In both cases the maximum allowable length was 0.6 m.

In the BEM (7-10) the shim surfaces are represented by discretized meshes consisting of nodes and triangles and a stream function is defined over the surface which is approximated as a weighted sum of basis functions relating the current density to the stream function values at each node.

$$\psi(\mathbf{r}) \approx \sum_{n=1}^N I_n \psi_n(\mathbf{r}) \quad (4.5)$$

$$J(r) = \nabla \times [\psi(r)n(r)] \approx \sum_{n=1}^N I_n \nabla \times [\psi(r) n(r)] = \sum_{n=1}^N I_n J_n(r) \quad (4.6)$$

Where $\psi(r)$ is the stream function, $J(r)$ is the corresponding current density, I_n is the stream function value at node n , $J_n(r)$ is the current density basis and N is the total number of nodes on the surface.

This allows calculation of all relevant electromagnetic parameters solely in terms of the stream function. A functional is introduced of relevant coil metrics which is minimized to solve for the stream function value at each node. This functional will dictate the final performance of the design. Once the stream function is known, it is contoured to produce wire patterns which approximate the current density on the surface. In this work, the BEM was implemented using a minimum power method utilizing a performance functional as follows:

$$U = \frac{1}{2} \sum_{k=1}^K \left[\sum_{n=1}^N (I_n C_n(r_k)) - B_z^{\text{tar}}(r_k) \right]^2 + \frac{\beta}{2} \sum_{n=1}^N \sum_{m=1}^M I_n I_m R_{nm} \quad (4.7)$$

$$U = \frac{1}{2} \sum_{k=1}^K [B_z(r_k) - B_z^{\text{tar}}(r_k)]^2 + \frac{\beta}{2} P \quad (4.8)$$

Where $B_z(r_k) = \sum_{n=1}^N (I_n C_n(r_k))$ is the z component of the magnetic field at target point r_k due to the all stream function nodes, $C_n(r_k)$ is the field matrix describing the field contribution from node n at target point r_k , $B_z^{\text{tar}}(r_k)$ is the ideal field profile, at point r_k , defined by a set of magnetic field targets, I_n and I_m are the stream function value at the n^{th}

and m^{th} node, respectively; and $P = \sum_{n=1}^N \sum_{m=1}^M I_n I_m R_{nm}$ is the power dissipated in the coil surfaces with a resistance matrix R_{nm} . N is the total number of surface nodes and K is the total number of target points. The value β weights the relative importance between homogeneity and power minimization. Traditionally, when designing shim coils, one must be careful of higher order shims coupling directly with the gradient coils. Incorporating the known wire pattern for the gradient coils and using the BEM with an additional mutual inductance term introduced to the functional can minimize this coupling (4). As this study was primarily focused on the evaluation and comparison of shoulder cut-out and non-shoulder cut-out spherical harmonic shims this was not employed. In addition to the performance functional one can modify the coil by varying the number of contours in which the stream-function is contoured.

In this work shim homogeneity was calculated using two methods: 1) the maximum absolute deviation between the ideal magnetic field profile and the produced magnetic field profile, as calculated by Biot-Savart calculations, over a sphere of 0.20m:

$$\text{Max Dev} = \max (|B_z(r_k) - B_z^{ideal}(r_k)|) \quad (4.9)$$

Where $B_z(r_k)$ is the z-component of the magnetic field produced by the shim coil at the target point r_k and $B_z^{ideal}(r_k)$ is the z-component of the ideal spherical harmonic at the target point r_k .

and 2) the Euclidean distance between all ideal magnetic field calculation points and the produced magnetic field profile, as calculated by Biot-Savart calculations, over a sphere of 0.20m:

$$\text{Inhom} = \sqrt{\sum_{k=1}^N ((B_z(r_k) - B_z^{ideal}(r_k))^2)} \quad (4.10)$$

Where $B_z(r_k)$ is the z-component of the magnetic field produced by the shim coil at the target point r_k , $B_z^{ideal}(r_k)$ is the z-component of the ideal spherical harmonic at the target point r_k , and N is the total number of target field points used in the BEM calculations. To

account for differences in shim coil efficiencies and the fact that target points are within a range of $-1 \leq B_z^{ideal} \leq 1$ the produced fields are each scaled first so that they fall within the same range prior to analysis.

To select a final set of shim coils for each configuration I selected the candidates which minimized the inhomogeneity in the magnetic field while prioritizing slew rate. To accomplish this, for each spherical harmonic axis, a subset of coils within 10% of the minimum deviation and maximum slew rate were found and from this the coil with the highest efficiency was chosen.

4.2.2 Eddy Current Analysis

Once a final set of shims coils for each configuration was determined I used previously derived wire patterns for an early generation of my X-Mode rotated gradient configuration to analyze the eddy current compensation. Since these gradient axes do not lay on the traditional X- and Y-axes I denote these as the d_1 - and d_2 -gradients. To do this I implemented in-house BEM code which solves for the induced eddy current profile on a representative bore surface, and it's associated magnetic field profile at the imaging region. With the assumption that the gradient coil is driven by a Heavyside step function, the stream function of the induced current in another thin conducting surface, such as a bore surface, is calculated as (7):

$$I^{cryo} = -[L_{nm}^{cryo}]^{-1} M_{mq}^{coil/cryo} \quad (4.11)$$

Where I^{cryo} is the stream function of the induced eddy current, L_{nm}^{cryo} is the self inductance matrix of the cryostat surface and $M_{mq}^{coil/cryo}$ is the mutual inductance matrix between the coil wire pattern and the cryostat surface. In this work I used a cryostat surface of radius = 0.3 m and length = 1.0 m to represent a typical head-only MR scanner geometry. Once the induced eddy current profile is determined the magnetic field produced is calculated over a 0.20 m sphere at the imaging region. This magnetic field profile is then fit to spherical harmonics for comparison in eddy current compensation between shim sets. Using the known magnetic field profile from each shim a current weighting is solved for each shim axis and then the magnetic field profile at that current is summed over all axes. The residual

field is then calculated as the difference in the eddy current magnetic field and the summed shim fields. This residual field is then fit to spherical harmonics to determine the reduction in eddy current magnetic field harmonics.

Post-hoc to explore increasing the performance of the shim sets I designed two extra coils for each configuration using the inverse of the eddy current field data as target points for the BEM algorithm. For these, two coils were designed one using the d_1 -gradient and another using the d_2 -gradient induced eddy current field data. A design study was not performed for these coils and only a total of four were designed, one for each gradient axis for each radius.

4.3 Results

Figure 4-1 shows the final selected shim coils for each configuration with their corresponding electromagnetic information given in Table 4-1. Figure 4-2 shows the spherical harmonic decomposition for the induced eddy current field and the shim compensated residual field profiles. Figure 4-3 shows the spherical harmonic decomposition for each spherical harmonic shim coil. Figure 4-4 shows the wire patterns for the extra eddy current compensation coils.

4.4 Discussion

I performed electromagnetic design simulations to determine the relative performance trade-offs between placing spherical harmonic shims inside or outside of the SCO region in a SCO gradient platform and observed the following: 1) the SCO set of spherical harmonic shims have a higher efficiency and can be driven faster, with a loss in homogeneity. 2) the SCO set of spherical harmonic shims perform worse than the complete cylinder shims when compensating for example eddy currents produced by a previously designed set of X-mode SCO gradient coils, and 3) including a pair of active compensation coils designed to cancel out the eddy current fields into the SCO shim set increases the performance in compensation of eddy currents.

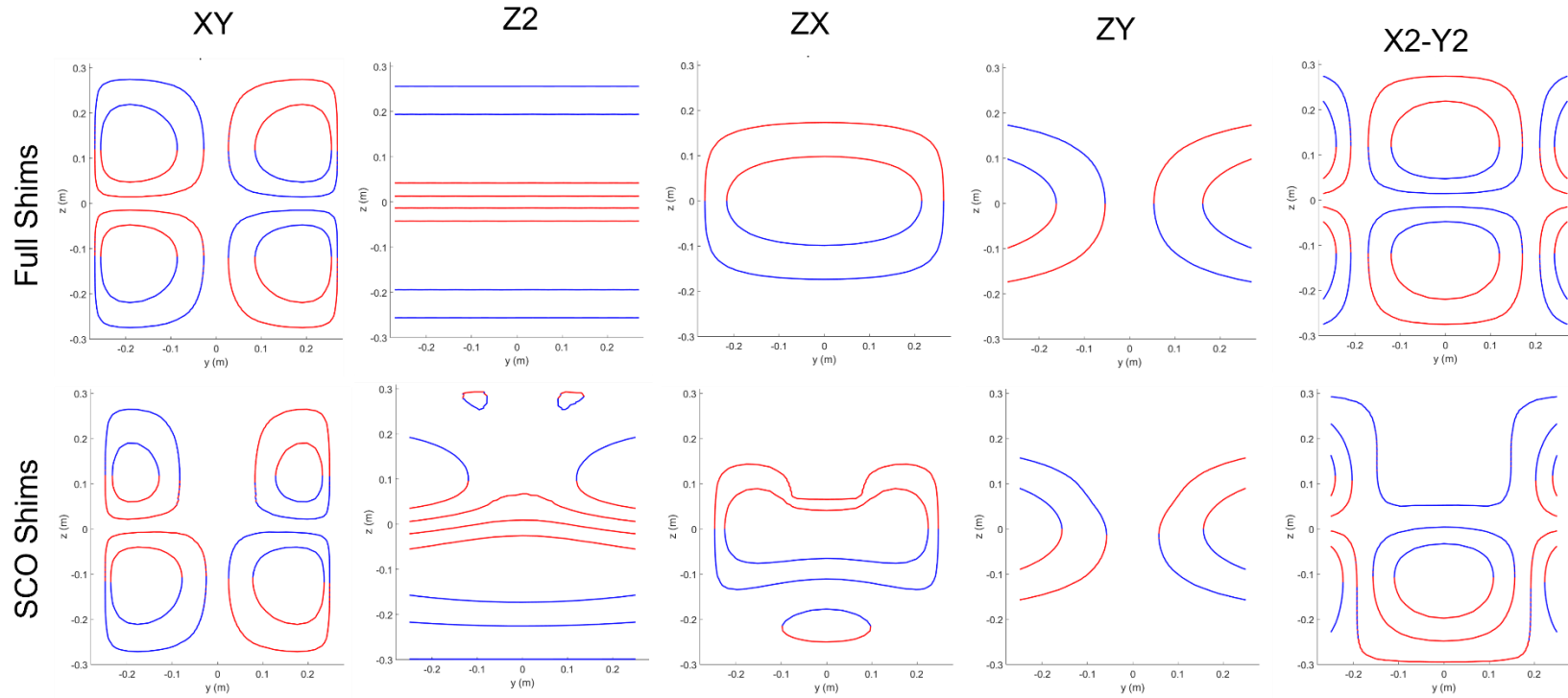


Figure 4-1: Example Shim Wire Patterns

Derived wire patterns for five spherical harmonic shim axes (XY, Z2, ZX, ZY, X2-Y2) for the full cylinder shim and shoulder cut-out shim cases. Colour indicates the direction of current flow with respect to the azimuthal direction.

The spherical harmonic shim sets presented here were designed such that they would be cut into copper clad G10 sheets and as such parameters such as resistance were calculated based on that assumption. Outside of that, there is no reason these could not be designed using wire press fit into grooves or other techniques. Further, anything calculated with this assumption can be easily recalculated using only the exported wire patterns independently of the design study.

Table 4-1: Example Shim Performance Parameters

Parameter	SCO Shims					Full Shims				
	X2Y2	XY	Z2	ZX	ZY	X2Y2	XY	Z2	ZX	ZY
Slew Rate [T/m ² /s]	112	122	509	366	416	87	87	413	290	290
Efficiency [μT/m ²]	46	51	244	83	71	45	45	224	57	57
Max Dev [AU]	9.7E-4	1.7E-4	1.2E-3	2.4E-3	1.1E-4	9.8E-5	9.3E-5	8.7E-4	5.9E-5	5.9E-5
Inhom [AU]	7.2E-6	1.8E-7	1.3E-5	2.9E-5	6.3E-6	6.2E-8	6.2E-8	8.8E-6	1.7E-8	1.7E-8

Max dev = the maximum deviation in the magnetic field between the simulated and ideal fields over a 0.20 m spherical surface. Inhom = inhomogeneity defined as the root-mean-squared difference between the simulated magnetic field profile and the ideal magnetic field profile over a 0.20 m spherical surface.

As can be seen in Figure 4-2, in terms of reducing the coefficients of the spherical harmonics within the eddy current magnetic field the SCO shim set overall performed worse than the full cylinder shim set primarily in the Z^2 , ZX and X^2-Y^2 cases and in some cases increased those components. This motivated performing decomposition on each shim axes produced field to determine the possible cause. The individual coil decompositions are given in Figure 4-3 and from this although both the SCO and full shim coil designs have equal primary spherical harmonic composition the SCO shims have on average higher secondary spherical harmonic components which make it more difficult to independently shim out specific spherical harmonics in the eddy current field. In all cases there was difficulty in compensating for the Z^2 term which is interesting.

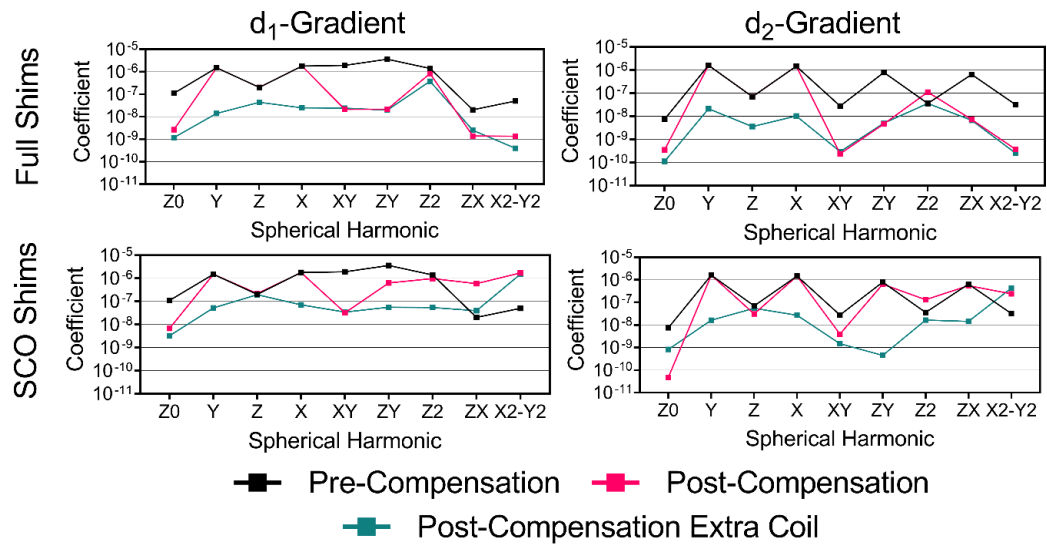


Figure 4-2: Shim Eddy Current Compensation

Decomposition of the induced eddy current field from example d1- and d2-gradient coils before compensation, after compensation with shims, and after compensation with shims + extra coil. Two pairs of extra coils (one SCO and one complete cylinder) were designed using the eddy current field data as field targets in the design algorithm (outlined in Section 4.2). These extra coils were then included with their respective shim set in the compensation algorithm.

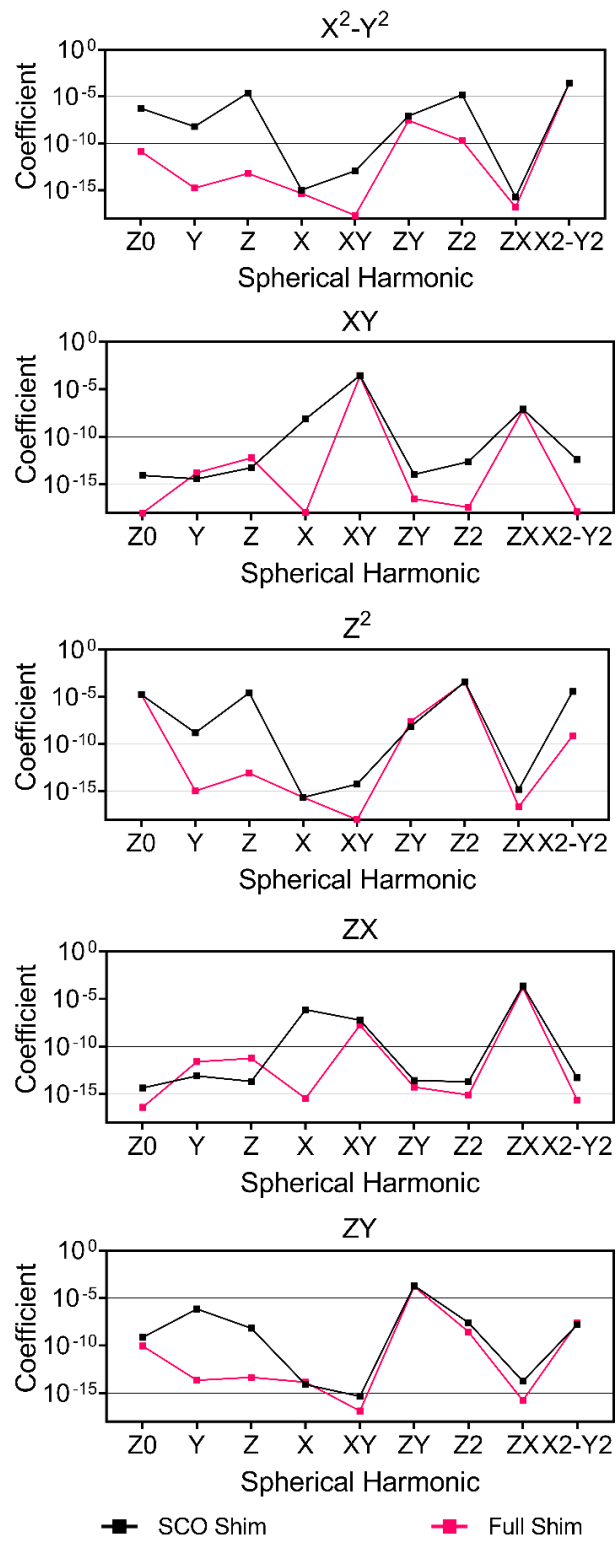


Figure 4-3: Shim Eddy Current Decomposition

SCO Shim = Shoulder cut-out shim, Full Shim = complete cylindrical shim. Decomposition of the produced magnetic field profile from each simulated spherical shim coil. All shims had strong primary field components of the designed spherical harmonic field. However, the SCO shims had stronger secondary field components due to the loss of symmetry in the design surface.

To further explore compensation of the eddy current fields, I designed two more coils using the negative of the d_1 and d_2 eddy current fields as the field targets for the design. I performed this for both cases and did not vary β but instead chose the same β value and number of contours as most designed shims. The individual coil wire patterns are given in Figure 4-4 and the corresponding eddy current compensation is given in Figure 4-2. In the case of the full cylinder shims the addition of these two coils to the problem did not see much of a reduction in the Z^2 term but did have the benefit of compensating for lower terms such as Z_0 , X, Y, Z which is typically accomplished using gradient preemphasis. With the SCO shims the performance benefit from the addition of this extra pair of coils is more noticeable. In addition to compensating most lower terms, there is a noticeable decrease in higher order terms with the exception of the X^2 - Y^2 term which is observed in both SCO cases, with and without the extra coils. As well, in the SCO case we see a reduction in the Z^2 term that I did not observe in the full cylinder case.

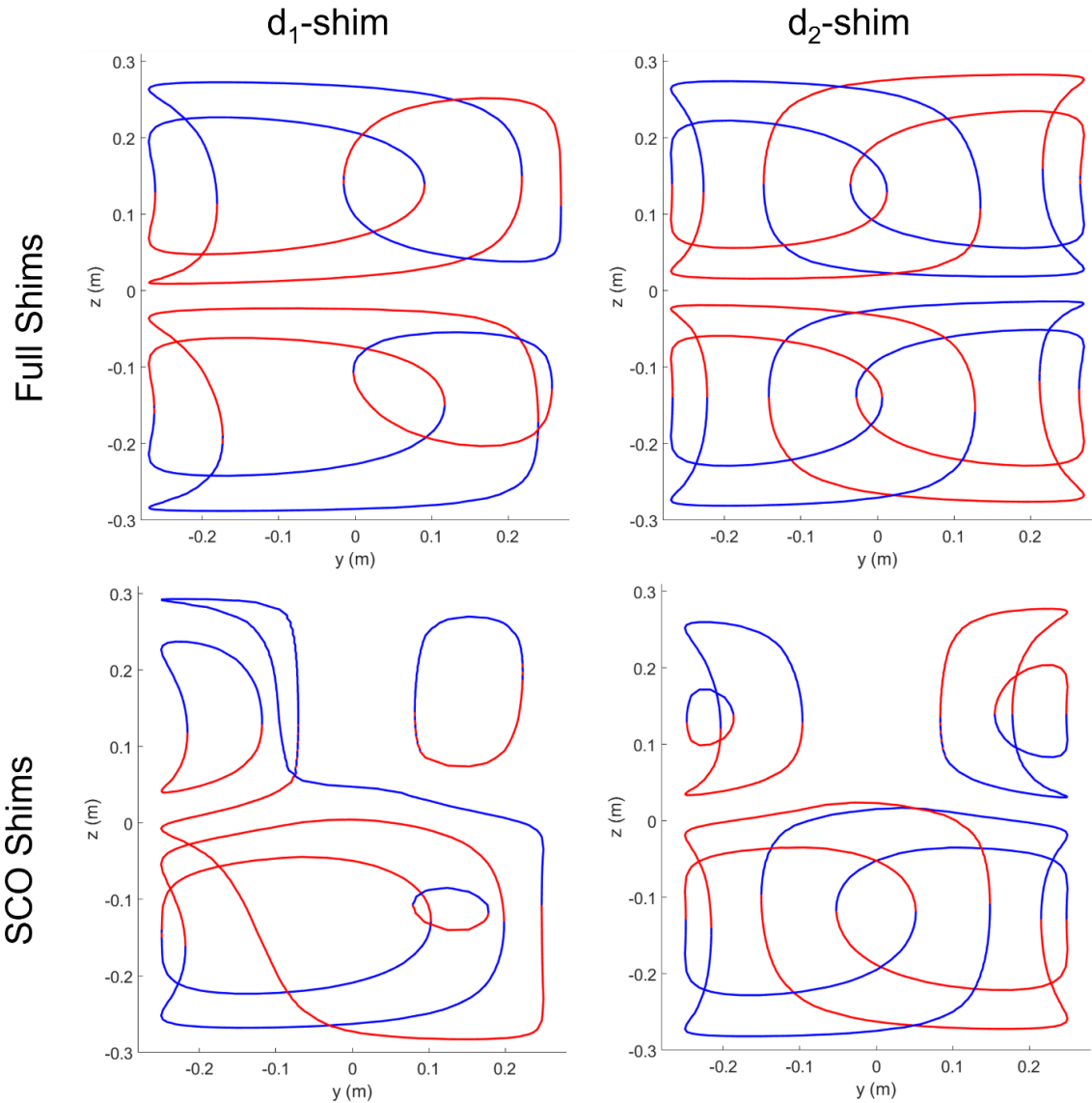


Figure 4-4: Sample Eddy Current Field Coils

Wire patterns created using the eddy current field data for extra compensation performance. Colour indicates the current direction with respect to the azimuthal direction.

One limitation of this work is in the definition of homogeneity and the homogeneity requirements for full dynamic eddy current compensation. While the homogeneity metrics presented here are useful for comparing relative performance between the shoulder cut-out and full cylinder shim set, they are unhelpful in determining the homogeneity requirements in compensating the induced eddy currents. To mitigate this, we implemented spherical harmonic decomposition using previously designed X-mode gradient coils and a stream-

function eddy current solver however, the use of induced eddy current information calculated using the BEM is not without limitations. Primarily although this gives a good approximation of the complexity and magnitude of the eddy currents it fails to provide information on the time evolution. This would require more complex simulations incorporating more realistic cryostat surfaces however, for relative comparisons in exploring the trade-offs in the design of SCO shims this was considered unnecessary. Another limitation in this study is that I did not explore the complexity of the induced eddy current by the shim coils themselves. With the SCO shims breaking symmetry it would be reasonable to expect the introduction of higher order eddy currents in the cryostat surface. However, these would be weaker than those introduced by the gradient switching. This is important but still something that may motivate the exploration of actively shielded SCO shims. Basically, by combining the inner SCO surface and outer non-SCO surfaces into the problem it would be possible to design shims such as those presented here but with active shielding. This is a possible avenue for future work. It is important to note that the extra compensation coils used the complete eddy current field without gradient pre-emphasis. In practice the significant X and Y field terms can be compensated using the gradients and it may be worth exploring the same design with the field targets calculated using the post gradient compensation field. This may be valuable as the original field targets have dominate X and Y field terms that would be removed with gradient preemphasis.

This study gives an indication of the trade-offs in the design of active spherical harmonic shims with shoulder cut-outs for a head and neck platform. However, two main aspects would need to be modified to incorporate shims like those presented here into a finished gradient coil. First, the design study would need to incorporate the mutual inductance with the gradient layers to avoid unnecessary electromagnetic coupling between the shims and the gradient coils. Second, the radii would need small adjustments to account for the thickness of copper and tubing. This would push some of the shim coils to a larger radii which would have to be chosen appropriately to balance the small electromagnetic trade-off that comes with that. Lastly, although these shim coils are operated with lower voltages and currents than a gradient coil incorporating force and torque balancing into the designs may be necessary for implementation in certain platforms. This modification can be made

with a simple addition to the performance functional with the addition of Lagrange multipliers utilizing the magnetic field profile of the B_0 magnet.

4.5 Conclusion

Ultimately, this work provides the first direct comparison between SCO and non-SCO shims for use in a compact head and neck imaging platform. While the SCO shims are stronger and faster which is convenient for dynamic applications the increase in those performance metrics over the non-SCO shim coils does not warrant the decrease in homogeneity that comes with it.

4.6 References

- [1] Juchem C, de Graaf RA: B_0 magnetic field homogeneity and shimming for in vivo magnetic resonance spectroscopy. *Anal Biochem* 2017; 529:17–29.
- [2] Stockmann JP, Wald LL: In vivo B_0 field shimming methods for MRI at 7 T. *Neuroimage* 2018; 168(June 2017):71–87.
- [3] Juchem C, Nixon TW, McIntyre S, Boer VO, Rothman DL, De Graaf RA: Dynamic multi-coil shimming of the human brain at 7 T. *J Magn Reson* 2011; 212:280–288.
- [4] Poole M: Improved Equipment and Techniques for Dynamic Shimming in High Field MRI. *PhD thesis, Univ Nottingham, United Kingdom, 2007(August):25.*
- [5] Lessard EJ, Handler WB, Chronik BA: Preliminary Design Exploration for a Head and Neck Gradient Coil: Effect of Shoulder Cut-out Length on Performance. *Proc Intl Soc Mag Reson Med* 27 2019.
- [6] Lessard EJ, Handler WB, Chronik BA: The X-Mode Gradient: Improved Performance for Select Applications. *Proc Intl Soc Mag Reson Med* 28 2020.
- [7] Peeren GN: Stream function approach for determining optimal surface currents. *J Comput Phys* 2003; 191:305–321.
- [8] Lemdiasov RA, Ludwig R: A stream function method for gradient coil design. *Concepts Magn Reson Part B Magn Reson Eng* 2005; 26B:67–80.

- [9] Tomasi D: Stream function optimization for gradient coil design. *Magn Reson Med* 2001; 45:505–512.
- [10] Poole M, Bowtell R: Novel gradient coils designed using a boundary element method. *Concepts Magn Reson Part B Magn Reson Eng* 2007; 31B:162–175.

Chapter 5

5 Design, Construction and Verification of 21MHz Radiofrequency Coil

This chapter consists of an unpublished manuscript titled:

Eric J. Lessard, Kieffer J. Davieau, Diego F. Martinez, Colin Metrow, William B. Handler, and Blaine A. Chronik. *A 21 MHz RF Coil Designed Using a Boundary Element Method: Theoretical Design, Experimental Results, and Next Steps*

5.1 Introduction

While the clinical and research MR environment has historically observed a race towards high-field platforms recently, low-field MRI has seen a resurgence in terms of research and clinical applications (1-3). This has motivated the design of purpose-built MR systems using permanent magnets (4-6) and superconducting wire (7). These systems typically benefit from simplified siting requirements, decreased capital costs, and lower specific absorption rate. The lower magnetic field in these systems corresponds to a lower Larmor frequency of the nuclei of interest. Table 5-1 gives a list of MR visible nuclei and their Larmor frequency at across a range of field strengths.

Table 5-1: Larmor Frequency for Various Nuclei

	0.064T	0.5T	1.5T	3T	7T
^1H	2.7 MHz	21 MHz	64 MHz	128 MHz	300 MHz
^3He	2.1 MHz	16 MHz	49 MHz	97 MHz	230 MHz
^{13}C	0.7 MHz	5.4 MHz	16 MHz	32 MHz	75 MHz
^{19}F	2.6 MHz	20 MHz	60 MHz	120 MHz	280 MHz
^{129}Xe	0.75 MHz	5.9 MHz	18 MHz	35 MHz	82 MHz

Examples of MR visible nuclei and their relative frequency across a range of field strengths. Low frequency techniques may be possible at comparatively higher field strengths for difference nuclei. ^1H = Proton, ^3He = Helium-3, ^{13}C = Carbon-13, ^{19}F = Fluorine-19, ^{129}Xe = Xenon-129.

While a lower Larmor frequency will have a negative effect on the MR signal it may allow usage of low-frequency development tools towards the design of RF coils. Generally, the role of the RF coil in an MR experiment is transmitting and receiving signal from the MR environment. The transmit coil generates an RF pulse consisting of a magnetic field perpendicular to the B_0 direction. This field oscillates at the Larmor frequency which is nuclei and B_0 dependent. This provides the goal of exciting the spins within the sample and tips them away from their equilibrium. A transmit RF coil has various requirements. Among these are: production of a homogeneous magnetic field across the imaging region, production of a strong magnetic field to tip the spins in a timely manner and for optimal energy transfer it must be tuned to the Larmor frequency of the nuclei of interest within the B_0 field.

For head/neck and brain imaging typical types of transmit radiofrequency coils include birdcage style, surface coil arrays, dipole antennas, and local shim-array coils (8). Considered to be the most successful MR RF coil, the bird cage coil is a volume coil consisting of two end-rings and an even number of rungs connecting them (9). The number of rungs will influence the homogeneity of the produced magnetic field. Capacitors are placed strategically throughout either the centre of the rungs or along the end caps. This has the purpose so that the rungs vary in phase during operation and produce a circularly polarized transmit field.

Previously, I have motivated the design of an MR system wherein the gradient coil subsystem employs a shoulder cut-out design to enable to patient to enter further into the system and within a small radius system allow imaging of both the head and neck (10,11). Unfortunately, a bird cage style RF transmit coil is naturally incompatible with a system such as this due to the end ring requirement. In the bird cage configuration the end rings prevent entrance past the shoulder and cannot be removed. A technique used in the design of MRI gradient coils, known as the boundary element method (BEM), allows calculation of wires in space which produce a target field profile (12-14). This technique is flexible in geometry and allows derivation of wire patterns on arbitrary surfaces. Due to the low

frequencies at which gradient coils operate, the electromagnetics operate within a magnetoquasistatic regime which allows the simplification of Maxwell's equations in terms of neglecting the displacement current, a consequence of rapidly changing fields (15). While this approximation has been demonstrated to be valid at the low operational frequencies used in gradient switching this is not the case for the RF coils and as such these methods are not employed to design clinical frequency RF coils. Due to this, full-wave simulations must be employed when calculating magnetic field profiles from designed RF coils. These simulations include Maxwell's displacement current and are significantly more time consuming and it is impractical to design complex, or unique geometries RF coils using these techniques.

With the resurgence of interest in low-field MRI platforms there have been successful demonstrations of applying these techniques to ultra-low frequencies such as 2.7 MHz. However, there exists clinical interest in low-field scanners operating at 0.5T (7) corresponding to a frequency of 21 MHz. In our lab previous work has been done comparing BEM derived wire patterns and full-wave simulations however, experimental construction and field verification has yet to be performed.

In this work a cylindrical low-field transmit RF coil consisting of two linearly polarized electromagnets is designed, constructed, and verified for use at 21 MHz.

5.2 Methods

5.2.1 Computational Methods

Triangular element meshes were generated using in-house mesh generating software written in MATLAB. The length and outer diameter (OD) were chosen to correspond with typical bird-cage style coils for head-only applications and as such were designed to be installed on tubing of a length of 0.364m and an OD of 0.403 m. The choice was made to use CNC cut copper-clad G10 sheets of 0.25 mm thick copper and 0.50 mm thick G10 to machine the wire patterns which would then be rolled around the tubing and affixed. Choosing to lay the first layer copper side down and the second copper side up to ensure appropriate electromagnetic isolation between the two layers lead to a design radius of 0.2016 m for the X-polarized field and 0.2029 m for the Y-polarized field coils,

respectively. Once the meshes had been generated, they were used in a custom in-house boundary element method solver (14) which aims to determine wire positions in space which when current is ran through best match an input target field profile as constrained by a performance functional accounting for field homogeneity and ohmic power loss throughout the electromagnet. To accomplish this, I solve for a stream-function value at each node on the surface and then contour it to provide wire positions in space. A functional is introduced to provide a single solution and balance the relative importance of field homogeneity and dissipative power as follows:

$$U = \frac{1}{2} \sum_{k=1}^K [B_z(r_k) - B_z^{\text{tar}}(r_k)]^2 + \frac{\beta}{2} P \quad (5.1)$$

Here, the first term represents field homogeneity as the sum of squares difference between the produced magnetic field and the target profile while the second term represents the power dissipated through the RF coil through Joule heating. Once the stream-function is calculated, for a particular performance functional weighting, and contoured all electromagnetic and design-relevant parameters can be calculated. Interest in this work is the minimum wire spacing (W_{\min}), which is determined by the calculated stream-function profile and the number of contours; the RF inhomogeneity calculated as the coefficient of variation of the magnetic field inside a sphere of 0.25 m; and the resistance, which is calculated using the resistivity of copper and the physical wire information.

RF inhomogeneity was calculated as the coefficient of variation in the magnetic field calculated over equally spaced points in a 0.25 m diameter sphere situated at the isocenter of the electromagnet.

$$inhom = \left| \frac{\sigma_{B_1}}{\mu_{B_1}} \right| * 100\% \quad (5.2)$$

A pool of potential coils for each axis was built by varying β , the relative weighting between homogeneity and ohmic loss; and the number of contours used. β was varied from 10^{-13} to 10^{-5} in 100 logarithmically spaced steps and the number of contours was varied, for each β value, from 4 to 24 in step sizes of 2. Coils considered for manufacturing were

narrowed down as the ones with W_{\min} which was larger than the CNC tolerance for manufacturing, an inhomogeneity $<2\%$ over 0.25m and from those the lowest resistance coil was chosen.

5.2.2 Construction Methods

Once the final RF coils were determined from the design study they were converted to flat planes using in-house MATLAB functions. Elements of the wire pattern were removed and individual loops of wire in the wire pattern were joined to make sets of continuous wire. The wire pattern was then exported for final touches in SOLIDWORKS (DS Systems, France) and machined using CNC routing onto copper clad G10 sheets. Once completed final electrical connections were added as needed and the layers were rolled onto the structural cylinder surface. Construction photos at various stages are shown in Figure 5-5. The coil was matched to 50 Ohms using a matching circuit constructed at the coil input.

5.2.3 Field Measurements

Single RF axis fields were produced using a Keysight RF generator operating at 25 dbm at an operational frequency of 21 MHz. Field measurements were performed using a 3-axis CNC stepped field mapping robot as previously described (16). The fields were measured using tuned b-field probes attached to a stepper robot. The b-field probe was attached to an oscilloscope which was controlled by the robotic software and read in at the programmed field positions. This was done by positioning the center of the b-field probe within the geometric center of the radiofrequency coil and defining that as the origin. A plane measurement was taken with respect to this center. Due to the size of the probe the probe could extend further in one direction than the other.

5.2.4 Full-Wave Simulations

Post-hoc, based on measured magnetic field profiles we performed full-wave electromagnetic simulations for a single axis using the commercial software Sim4Life (ZMT, Switzerland). These simulations were performed using the complete wire path with an RF input and output feed attached to the cylindrical wire patterns. The port was driven

with a current of 1 A for the simulations. Post-hoc based on these results we decided to perform the same simulations with the wire pattern split in half with both halves being driven in phase.

5.3 Results

Due to the symmetry in the X-polarized and Y-polarized magnets only the Y-polarized results will be shown in detail. Figure 5-1 shows β vs a) W_{\min} , b) Inhomogeneity, and c) Resistance across all β and contour combinations for the Y-polarized electromagnet. Figure 5-2 shows the selected electromagnet wire pattern Figure 5-3 shows the a) simulated magnetic field at the isocenter over a full period of 2π . Table 5-2 gives the simulated and measured electromagnetic performance parameters for both coils. Figure 5-4 shows a representative magnetic field plot from a) Biot-Savart simulations, b) measurement, and c) full-simulation, d) split-simulation. Construction photos of the RF coil are shown in Figure 5-5.

5.4 Discussion

I performed electromagnet design, simulation and construction of a low-frequency RF coil and observed the following: 1) there is disagreement in the magnetic field between the measured and Biot-Savart calculated field profiles. 2) there is qualitative agreement in the magnetic field profile between the measured and full-wave simulated field profiles. 3) the experimental setup violates the magnetoquasistatic assumption however, I hypothesize that this is due to the current path length of the designed coil as motivated by the split coil simulation results.

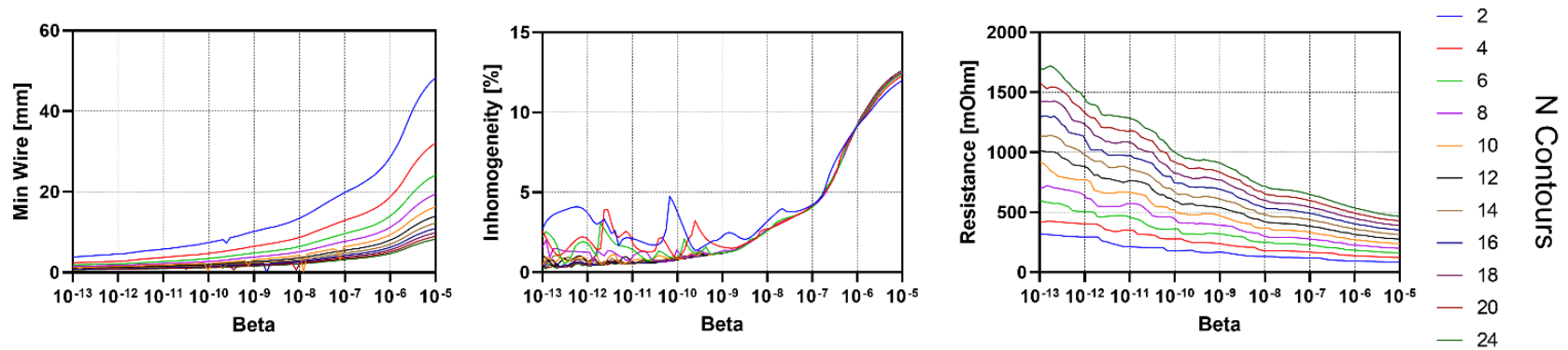


Figure 5-1: Performance Parameters vs Beta Value

Plots demonstrating the effect of changing Beta in the performance functional which varies the relative weighting of homogeneity and power dissipation. Resistance given for DC current. N contours is the number of contour lines used in creation of the RF wire pattern. As the relative importance of minimizing power dissipation is lowered by lowering the beta value the relative importance of field homogeneity is increased. This is observed as an increase in winding density leading to smaller minimum wire spacing, lower inhomogeneity and greater coil resistance. As the relative importance of minimizing power dissipation is increased by increasing the beta value the relative importance of field homogeneity is decreased. This is observed as a decrease in winding density leading to larger minimum wire spacing, higher inhomogeneity, and smaller coil resistance. Increasing the number of contours will increase the coil length and winding density and this is observed as a decrease in minimum wire spacing and increase in coil resistance.

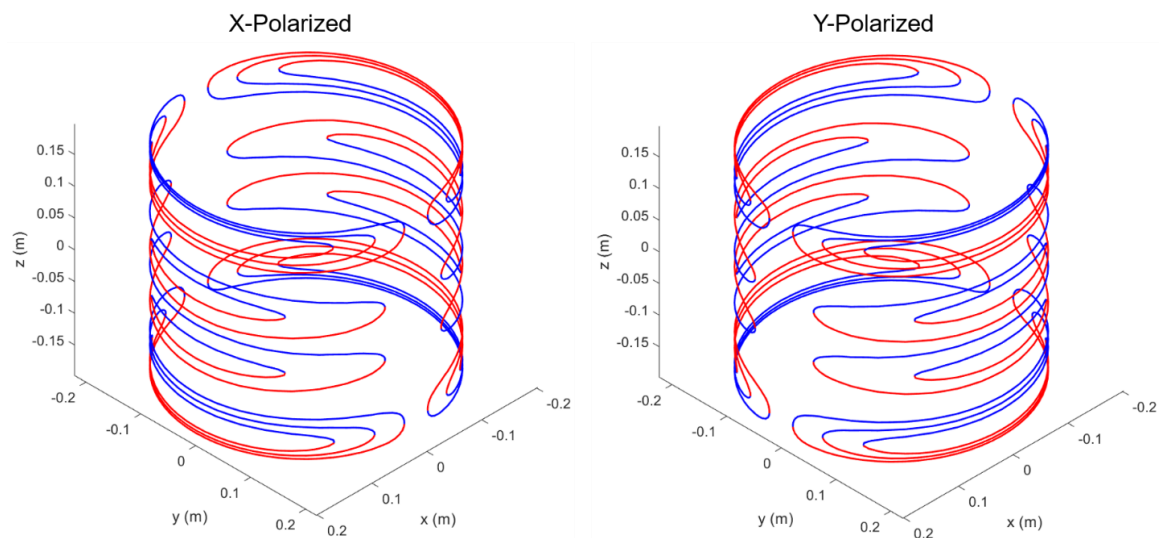


Figure 5-2: RF Coil Wire Patterns

Derived RF coil wire patterns for the X-polarized and Y-polarized coils. Colour indicates direction of current with respect to the azimuthal direction.

Figure 5-5 shows the various stages of construction and measurement of the final coil. Figure 5-5A shows a single layer as received from the machine shop prior to electrical connections being soldered on. Figure 5-5B shows the flat coil after electrical connections and insulating tape has been added as needed. Figure 5-5C shows the flat layer being wrapped around the structural tubing. At this stage the coil is held in place as superglue dries and the clamps are moved circumferentially around the coil to complete the adhesion to the tubing. Finally, Figure 5-5D shows the coil and the setup of the field measurement experiment. Construction photos are shown for both coil layers with measurements only performed for a single layer.

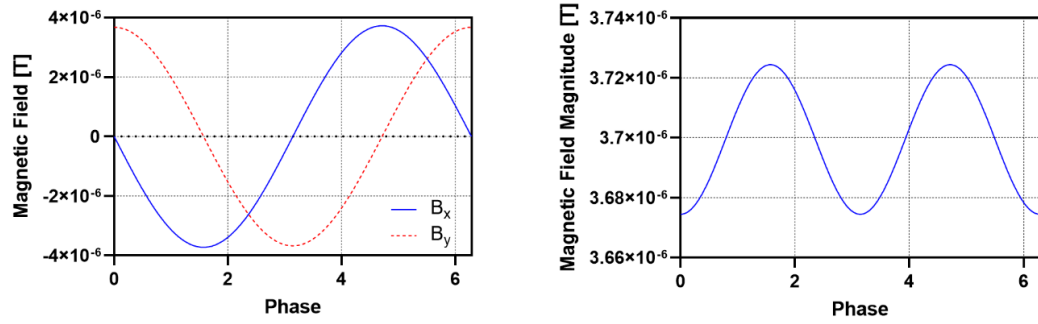


Figure 5-3: Simulated Field at [0,0,0] vs Time

Simulated magnetic field at the isocentre for the X-polarized and Y-polarized coils when run separately and together at a current of 1A.

It can be seen from Figure 5-4 that in the Biot-Savart simulations the center point at current of 1 A, has a mean magnetic field strength of 3.699 uT, a maximum magnetic field strength of 3.72 uT and a minimum magnetic field strength of 3.67 uT over the entire time series when the X- and Y-polarized electromagnets are ran $\pi/2$ out of phase. This corresponds to an overall percent-difference of 1.3% from maximum to minimum.

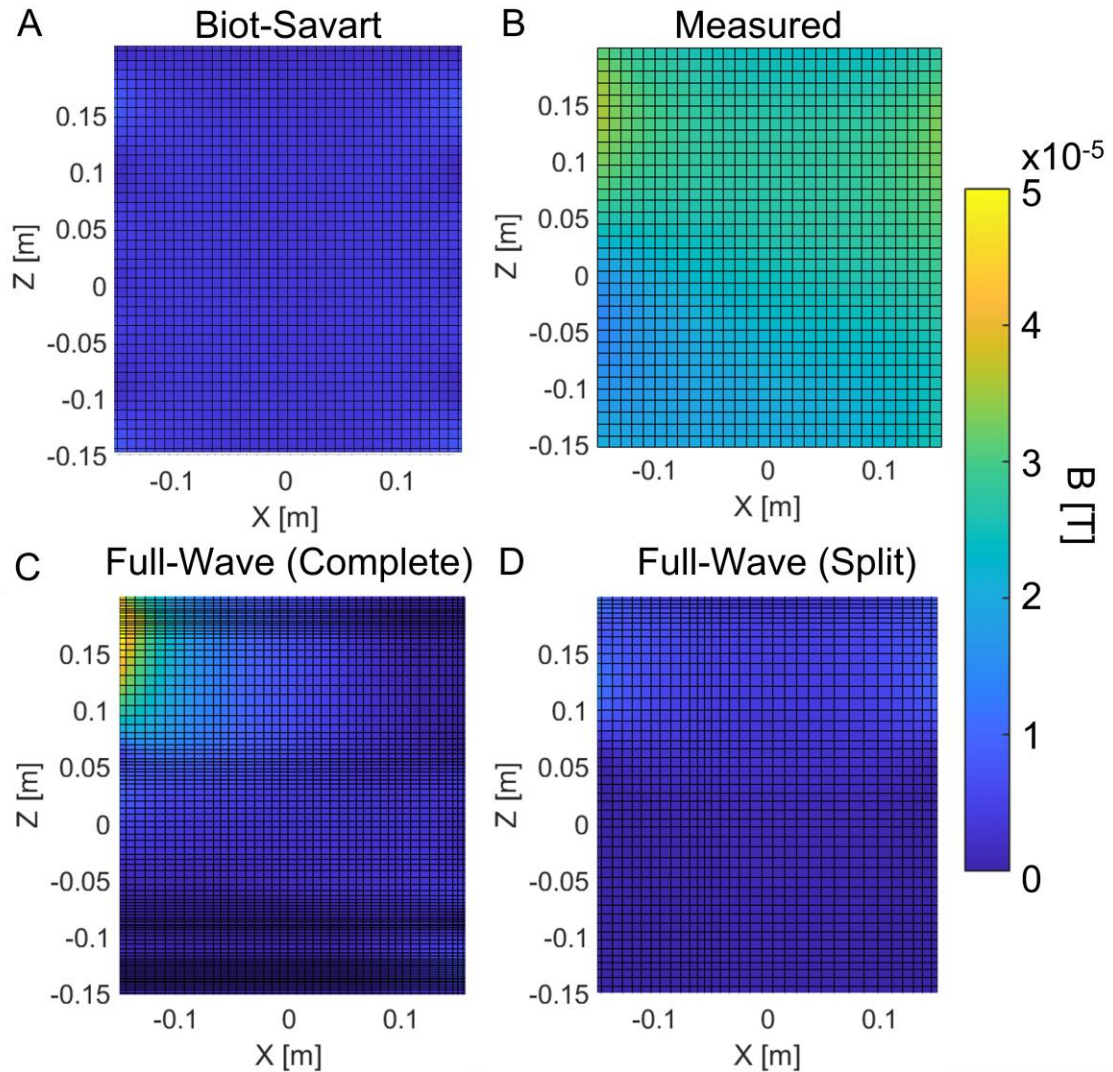


Figure 5-4: Magnetic Field Plots

Magnetic field plots during coil operation for the A) Biot-Savart simulations calculated as part of the quasistatic design process, B) Measured magnetic field using experimental setup shown in Figure 5-5D, C) Full-Wave (complete wire pattern) simulation results using Sim4Life, and D) Full-Wave (split wire pattern) simulation results using Sim4Life. Full-Wave (complete) uses the complete RF wire pattern driven using a single input port and Full-Wave (split) uses the RF wire pattern split into two equal half patterns each driven in-phase using separate input ports.

It is clear from Figure 5-4 that although the Biot-Savart simulations show a strong homogeneous field which encompasses the center of the RF coil this is not the case when looking at experimental measurements. To explore this further we performed full-wave simulations and observed a similar field profile as the experimental. While this difference could be due to a manufacturing issue such as a short between two wires this is unlikely and to explore this, I systematically measured electric properties of the circuit across the

two halves of a single RF axis and between the two layers. The symmetry in the measurements implies that it is likely not a manufacturing issue. This was further verified with the full-wave simulations showing a qualitatively similar field profile between full-wave and experimental. It should be noted that the Biot-Savart and full-wave simulations use a current of 1 A and the experimental measurements use a 25 dBm and are therefore not current matched. Upon further investigation I believe the issue is due to the long current path relative to the wavelength. Previous, unpublished work in which the full-wave simulations consisted of sets of independently driven current loops as opposed to a single current path showed no difference between full-wave and Biot-Savart simulations at this frequency. However, as evident here when the full current path is employed there exists differences in the simulation results. I believe this to be due to the electromagnetic wave delay within the RF circuit due to the finite speed of light. The RF circuit has a current path of approximately 19 m and at 21 MHz an electromagnetic wave has a wavelength of is 14 m in air. The wavelength would be further shortened in a conductor such as copper. Combining the fact that the wavelength is much smaller than the current path and the previous unpublished results showing agreement between full-wave and Biot-Savart simulations when shorter current loops are driven independently the authors believe this technique may be possible in the case of shorter coils which may have poorer homogeneity. We explored this by performing full-wave simulations with each half of the coil being run independently in phase with the other. This corresponds to a current path of approximately 9 m and from these results it appears to closer match the Biot-Savart simulations.

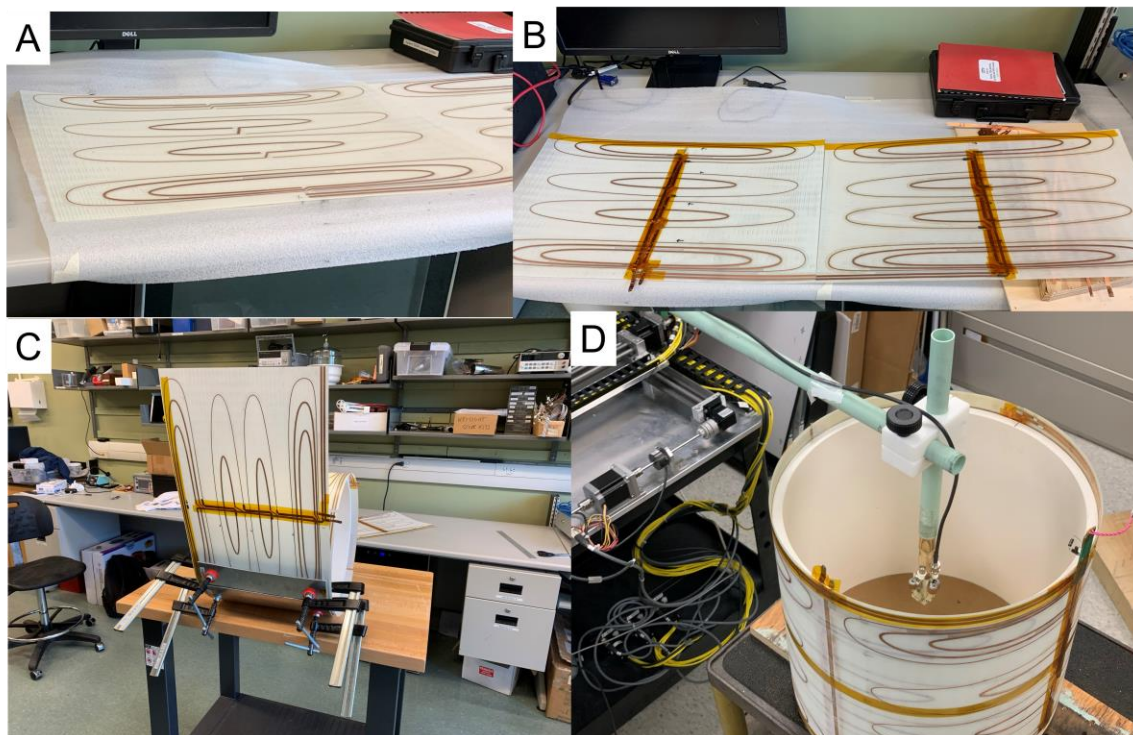


Figure 5-5: RF Coil Construction Photos

A) Flat coil without all electrical connections as received by the machine shop. B) flat coil with electrical connections and insulating tape added. C) in-progress rolling and adhering the coil to the cylindrical surface. D) Field measurement setup with B-field probe positioned within the upright RF coil.

While this work explored the design of a 21 MHz RF coil for ^1H imaging at 0.5T from Table 5-1 we can see that at the same magnetic field strength different nuclei will have a much lower Larmor frequency and in cases this technique may be applicable to multi-nuclei imaging at a wider range of field strength. For example, current research exploring ^{129}Xe at 0.074T (0.87 MHz) is promising (17) and this work may motivate the design of ^{129}Xe coils using low-frequency design techniques such as those outlined here. This is especially promising due to the SNR dependence of the hyperpolarized noble gas signal on field strength makes low-field imaging attractive (18).

By choosing coils with appropriate lengths or driving the coil in independently driven sections it may be possible to apply these techniques towards development of 21 MHz RF coils and design unique geometries such as a shoulder cut-out RF transmit coil. In cases where further entrance into a cylindrical bore is required cradle shaped gradient coils have been explored and this method could provide similar shaped RF coils in cases where the

frequency is low. Permanent magnet style head-cap magnets at much lower frequencies have shown the benefit of similar techniques in the design of head-cap RF coils (4). However, before this is worth exploring these results must be better understood and to accomplish this future work should be focused on designing and testing shorter coils than the ones presented here. The constructed coil presented here can still be used to explore this as the outer coil can be accessed and run as two separate halves. It may also be possible to further reduce this by splitting into four separate quadrants. However, each division would require the design of an appropriate RF power splitter to ensure that the halves/quarters are receiving equal in-phase power. This makes splitting the wire into equal lengths attractive as it ensures the resistance of the path length is equal and therefore makes power splitter easier. Lastly, further study on the inductive coupling between the RF wire patterns and the gradient coils that would be used is important to ensure that imaging is unaffected during operation. This opens up further study through incorporation of the gradient wire patterns into the design algorithm and including an additional mutual inductive term to minimize the electromagnetic coupling.

5.5 Conclusion

Although the constructed coil has field artefacts not captured by the Biot-Savart simulations used in the design this work motivates the potential future exploration of shorter RF coils designed using magnetoquasistatic design methods for the potential of improved B_1^+ homogeneity, unique geometries, and quicker designs.

5.6 References

- [1] Marques JP, Simonis FFJ, Webb AG: Low-field MRI: An MR physics perspective. *J Magn Reson Imaging* 2019; 49:1528–1542.
- [2] Bhat SS, Fernandes TT, Poojar P, et al.: Low-Field MRI of Stroke: Challenges and Opportunities. *J Magn Reson Imaging* 2021; 54:372–390.
- [3] Wald LL, McDaniel PC, Witzel T, Stockmann JP, Cooley CZ: Low-cost and portable MRI. *J Magn Reson Imaging* 2020; 52:686–696.

- [4] McDaniel PC, Cooley CZ, Stockmann JP, Wald LL: The MR Cap: A single-sided MRI system designed for potential point-of-care limited field-of-view brain imaging. *Magn Reson Med* 2019; 82:1946–1960.
- [5] Cooley CZ, McDaniel PC, Stockmann JP, et al.: A portable scanner for magnetic resonance imaging of the brain. *Nat Biomed Eng* 2021; 5:229–239.
- [6] O'Reilly T, Teeuwisse WM, de Gans D, Koolstra K, Webb AG: In vivo 3D brain and extremity MRI at 50 mT using a permanent magnet Halbach array. *Magn Reson Med* 2021; 85:495–505.
- [7] Panther A, Thevathasen G, Connell IRO, et al.: A Dedicated Head-Only MRI Scanner for Point-of-Care Imaging. In *Proc Intl Soc Mag Reson Med* 27; 2019.
- [8] Gruber B, Froeling M, Leiner T, Klomp DWJ: RF coils: A practical guide for nonphysicists. *J Magn Reson Imaging* 2018; 48:590–604.
- [9] Ahmad SF, Kim YC, Choi IC, Kim HD: Recent progress in birdcage RF coil technology for MRI system. *Diagnostics* 2020; 10:1–19.
- [10] Lessard EJ, Handler WB, Chronik BA: Preliminary Design Exploration for a Head and Neck Gradient Coil: Effect of Shoulder Cut-out Length on Performance. *Proc Intl Soc Mag Reson Med* 27 2019.
- [11] Lessard EJ, Handler WB, Chronik BA: The X-Mode Gradient: Improved Performance for Select Applications. *Proc Intl Soc Mag Reson Med* 28 2020.
- [12] Peeren GN: Stream function approach for determining optimal surface currents. *J Comput Phys* 2003; 191:305–321.

- [13] Poole M, Bowtell R: Novel gradient coils designed using a boundary element method. *Concepts Magn Reson Part B Magn Reson Eng* 2007; 31B:162–175.
- [14] Harris CT, Handler WB, Chronik BA: Electromagnet design allowing explicit and simultaneous control of minimum wire spacing and field uniformity. *Concepts Magn Reson Part B Magn Reson Eng* 2012; 41 B:120–129.
- [15] John David Jackson: *Classical Electrodynamics*. 1998.
- [16] Wawrzyn K, Hendriks J, Gignac D, Handler WB, Chronik BA: Comparison of Simulated and Robotically Mapped RF Fields in 64 and 128 MHz Medical Implant Test Systems. In *Proc Intl Soc Mag Reson Med*; 2019.
- [17] Perron S, Ouriadov A, Wawrzyn K, et al.: Application of a 2D frequency encoding sectoral approach to hyperpolarized ^{129}Xe MRI at low field. *J Magn Reson* 2022; 336:107159.
- [18] Parra-Robles J, Cross AR, Santyr GE: Theoretical signal-to-noise ratio and spatial resolution dependence on the magnetic field strength for hyperpolarized noble gas magnetic resonance imaging of human lungs. *Med Phys* 2005; 32:221–229.

Chapter 6

6 Dynamic Eddy Current Compensation using a Matrix Array

This chapter consists of a manuscript in preparation for submission to Magnetic Resonance in Medicine titled:

Eric J. Lessard, William B. Handler, and Blaine A. Chronik. *Dynamic Eddy Current Compensation and Spherical Harmonic Shimming using a Matrix Array Coil.*

6.1 Introduction

The drive for higher performance gradient coils has come with an increased use of increasingly complex designs such as asymmetric gradient coils (1, 2) and unique geometries like gradient coils with shoulder cut-outs (3–5). As the gradient coil moves away from symmetry within the MRI system there is a corresponding increase in the complexity of the induced eddy currents and their associated magnetic field profile. This is traditionally solved with an increase in shielding performance which has the trade-off of a decrease in imaging performance (2, 6, 7). In addition, shielding asymmetric and complex geometry gradient coils is a more challenging task than shielding symmetric coils. This makes eddy current compensation important and is traditionally employed using gradient pre-emphasis to compensate for low order harmonics within the eddy current field. However, in certain gradient coil configurations the residual eddy current profile may have unwanted higher order field harmonics that remain even with gradient pre-emphasis. This poses unique challenges by handling eddy currents through either hardware or post-processing means.

Higher order harmonic eddy current compensation can be accomplished using the resistive spherical harmonic active shims in a similar way to gradient pre-emphasis through dynamic application of the shims during the imaging sequence. Although the shim set is used for correcting of inhomogeneities due to the presence of conducting material within the magnetic field their higher order harmonic field profiles can also be used to remove the unwanted eddy current harmonics. In addition to traditional spherical harmonic shims

matrix array, or multi-coil, techniques have been successful at higher fields for slice-by-slice shimming and even spatial encoding (8–10) and have been proposed as a method of producing gradient fields for MRI (11). They have the benefits of being able to produce arbitrary magnetic field profiles and are often not optimized for a shape and allow non-spherical imaging regions to be constructed. Although, these have had success in shimming higher order harmonics and improving image quality on a dynamic slice-by-slice basis they have not been explored for use of dynamic eddy current compensation. Further, these multi-coil implementations require insert sized matrix coils or inclusion into the RF receive chain and use large numbers of independently driven channels, often 32 and higher, requiring extra hardware that may not be readily available within the MR workflow.

In head-only MRI platforms where the inner diameter is already limited it would be beneficial to implement a matrix array within the gradient housing. However, the radial space within a compact gradient is already at a premium and incorporating more layers of electromagnet wire limits the space available for the gradient axes, shim set and cooling. Therefore, in this work I explored the design of a matrix array coil to *replace* the traditional spherical harmonic shim set within a head-only MRI platform while demonstrating the feasibility of dynamically compensating for eddy current fields and the ability to create arbitrary magnetic field profiles.

6.2 Methods

6.2.1 Theory

In this work a predefined coil profile consisting of independently driven current loops spaced over the surface of a cylinder and a set of field target field points spanning an imaging region location was defined:

$$B^{tar} = \begin{bmatrix} B_{z1} \\ \vdots \\ B_{zk} \end{bmatrix} \quad (6.1)$$

Where B^{tar} is the target field points and B_{zk} is the z-component of the magnetic field at field target point k. A field matrix describing the field contribution at each target point from each loop was constructed as follows:

$$C = \begin{bmatrix} C_{11} & \cdots & C_{n1} \\ \vdots & \ddots & \vdots \\ C_{1k} & \cdots & C_{nk} \end{bmatrix} \quad (6.2)$$

Where C_{nk} is the field contribution from loop n at field point k. From this an individual current weighting can be determined for each current loop that approximates the target field profile. The field is calculated in this work using the Biot-Savart approximation for magnetic fields:

$$B(\mathbf{r}) = \frac{\mu_0}{4\pi} \int_C \frac{I d\boldsymbol{\ell} \times \mathbf{r}'}{|\mathbf{r}'|^3} \quad (6.3)$$

Where I is the current flowing along a path C with $d\boldsymbol{\ell}$ representing a infinitesimal portion of the path at point $\boldsymbol{\ell}$ and $\mathbf{r}' = \mathbf{r} - \boldsymbol{\ell}$ is the distance between the infinitesimal current portion and the point at which the field is calculated. In this work, currents paths are represented as wire patterns described in terms of current elements consisting of an x, y, and z positional value for the centre of the element of length dx, dy, dz and a current running through the element of 1 A.

$$element_i = \begin{bmatrix} x_i \\ y_i \\ z_i \\ dx_i \\ dy_i \\ dz_i \\ 1 \end{bmatrix} \quad (6.4)$$

With this the z-component of the magnetic field from a single current loop (Loop 1) can be calculated through numerical integration of the elements that compose that loop as follows:

$$C_{1k} = \sum_{el=1}^N \frac{(dx_{el}r'_y - dy_{el}r'_x)}{|r'|^3} \quad (6.5)$$

Where C_{1k} is the z-component field contribution of current loop 1 at target point k with $r' = (x_k, y_k, z_k) - (dx_{el}, dy_{el}, dz_{el})$ and the summation is performed over N current elements. This is calculated for all current loops at each field target. Since the total magnetic field at the target points is the sum of the fields produced by each loop and the fields will scale linearly with current the total field with individual current profiles for each loop can be written as:

$$\begin{bmatrix} B_{z1} \\ \vdots \\ B_{zk} \end{bmatrix} = \begin{bmatrix} C_{11} & \cdots & C_{n1} \\ \vdots & \ddots & \vdots \\ C_{1k} & \cdots & C_{nk} \end{bmatrix} \begin{bmatrix} w_1 \\ \vdots \\ w_n \end{bmatrix} \quad (6.6)$$

With W_n being the current weighting value for loop n which can be solved as:

$$W = \begin{bmatrix} w_1 \\ \vdots \\ w_n \end{bmatrix} = \begin{bmatrix} B_{z1} \\ \vdots \\ B_{zk} \end{bmatrix} \begin{bmatrix} C_{11} & \cdots & C_{n1} \\ \vdots & \ddots & \vdots \\ C_{1k} & \cdots & C_{nk} \end{bmatrix}^{-1} \quad (6.7)$$

Where W is the current weighting vector and W_n is the current through loop n. This can be extended to dynamic eddy current compensation by performing the matrix inversion at each measurement time point.

$$W(t) = \begin{bmatrix} w(t)_1 \\ \vdots \\ w(t)_n \end{bmatrix} = \begin{bmatrix} B(t)_{z1} \\ \vdots \\ B(t)_{zk} \end{bmatrix} \begin{bmatrix} C_{11} & \cdots & C_{n1} \\ \vdots & \ddots & \vdots \\ C_{1k} & \cdots & C_{nk} \end{bmatrix}^{-1} \quad (6.8)$$

6.2.2 Design Methods

Using in-house electromagnetic software written in MATLAB matrix coils of independently driven current loops were created over surfaces of radius 0.265 m with a maximum length of 0.36 m. Three sets of matrix coils were created with 8, 16, and 24

current loops. The coil locations were designed to be equally spaced azimuthally around the cylinder and along the longitudinal axis. The wire patterns for each matrix coil configuration are shown in Figure 6-1. A set of field target points corresponding to a sphere of 0.20 m diameter situated around the isocentre were constructed for field calculations. At these field points the magnetic field profile was calculated for each current loop, at a current of 1 A, using an in-house Biot-Savart solver.

6.2.3 Spherical Harmonic Field profiles

To evaluate the matrix coil performance in creating individual spherical harmonic field profiles sets of target fields (B_z^{tar}) were made corresponding to first order spherical harmonics (X-, Y- and Z-gradients), and second order spherical harmonics (XY, Z^2 , ZX, ZY and X^2-Y^2). The idealized gradient profile and spherical harmonics and ones produced by the matrix coils were plotted over a 0.20 m diameter spherical surface to visualize the produced fields.

6.2.4 Eddy Current Analysis

Eddy current analysis was performed two ways: A static eddy current case and a dynamic eddy current case. The static eddy current case is derived using a stream function boundary element method approach and wire patterns from a previously designed research prototype asymmetric X-gradient. With the assumption that the gradient wire pattern is driven with a Heavyside step function the stream function of the induced current in another thin conducting surface, such as a bore surface, is calculated as (12):

$$I^{\text{cryo}} = -[L_{nm}^{\text{cryo}}]^{-1} M_{mq}^{\text{coil/cryo}} \quad (6.9)$$

Where I^{cryo} is the stream function of the induced eddy current, L_{nm}^{cryo} is the self inductance matrix of the cryostat surface and $M_{mq}^{\text{coil/cryo}}$ is the mutual inductance matrix between the coil wire pattern and the cryostat surface. The magnetic field from the stream function induced in the cryostat surface is calculated as previously described (13, 14). Unfortunately, this formulation fails to provide details on the time evolution of the eddy current but can give an estimate of the complexity of the resultant field profile. In this work the stream function eddy current was solved in a radius of 0.3 m and length of 1.0 m

computational bore surface using the mutual inductance between the wire pattern from a previously manufactured research prototype X-gradient. This field profile was fit to the spherical harmonics before and after compensation. Compensation was performed solely with the matrix array coil and did not include any spherical harmonic shims or gradient coils.

For the dynamic eddy current case, I used experimental data for an asymmetric research prototype X-gradient coil. The eddy current magnetic field was compensated at each point and for each time point a current weighting for each current loop was solved for with the residual field calculated as the difference between the experimental field and the simulated matrix field profile. I compared these results to dynamic eddy current compensation using previously designed research prototype spherical harmonic shim coils combined with gradient and B_0 fields. This consisted of 10 field profiles used in the spherical harmonic compensation: B_0 , X-grad, Y-grad, Z-grad, XY, XZ, ZX, Z^2 , Z^3 , and X^2-Y^2 .

6.2.5 Power and Energy Analysis

To evaluate the power dissipated through the current loops in each of the three cases the resistance of the wire was calculated. Combining the current time data from the dynamic eddy current compensation and the resistance of the current loops the power dissipated through each loop was calculated at each time point.

6.3 Results

Figure 6-1 shows the matrix array coils. Figure 6-2 shows the eddy current decomposition of the simulated induced eddy current profile before and after compensation. Figure 6-3 shows the spherical harmonic surface profile over a 0.20 m diameter sphere for the idealized, 8-channel, 16-channel, and 24-channel cases. Figure 6-4 shows the experimental time series eddy current data and the simulated reduced eddy current field. Table 6-1 gives the maximum absolute field value for the experimental eddy current pre- and post-compensation using the 8-, 16-, and 24-channel compensation coils. Calculated resistance and inductance information for single channels in each configuration are given in Table 6-2. Figure 6-5 shows power and energy time curves for the 8-, 16-, and 24-channel compensation coils during dynamic eddy current compensation.

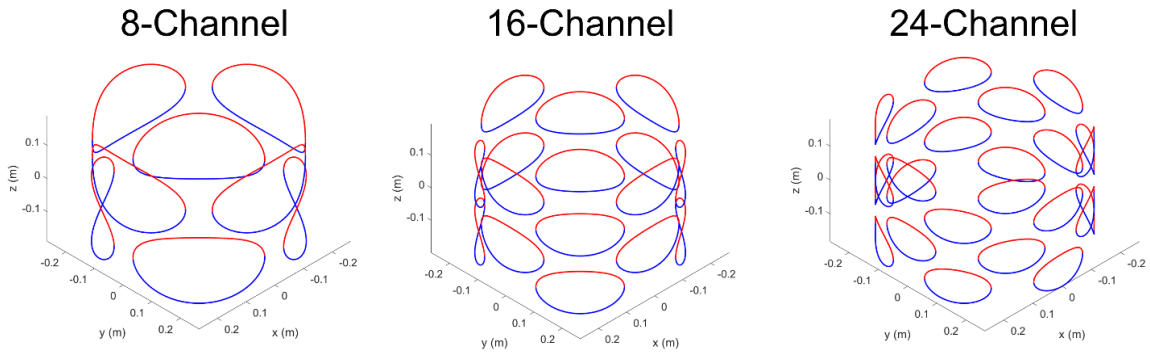


Figure 6-1: Multi-Coil Wire Patterns

Multi-coil wire patterns for the 8-, 16- and 24-channel cases. Colour indicates direction of current flow with respect to the azimuthal direction.

6.4 Discussion

I performed simulations of eddy current compensation using three different matrix array coils of 8-, 16-, and 24-channels of independently driven current loops and observed the following: 1) there was a noticeable increase in performance as the number of channels was increased from 8- to 24-channels, 2) all three configurations can produce a range of magnetic field profiles relevant to MRI and 3) the 16- and 24-channel matrix array coils performed better at compensating experimental eddy current data *in silico* than the spherical harmonic active shims.

Table 6-1: Multi-Coil Single Loop Inductance and Resistance

	Channels		
	8	16	24
Inductance [μH]	0.44	0.29	0.27
Resistance [$\text{m}\Omega$]	4.7	3.1	2.3

Inductance and resistance information calculated using the individual current loops.

In gradient coil configurations utilizing asymmetric or non-cylindrical designs the induced eddy current profile increases in complexity. These induced eddy currents can have higher order field terms that cannot be compensated using gradient compensation alone. This is

typically mitigated using improved magnetic shielding at the cost of gradient coil performance. However, the drive for higher performance gradients can make sacrificing shielding to increase performance attractive however, this comes with the requirement of compensating for eddy currents either through in-line or post-processing methods. Appropriate eddy current compensation accounting for these higher order terms can improve image quality and allow the use of gradient coils with decreased shielding and therefore increased performance while maintaining image quality through dynamic active compensation of induced eddy currents.

One method of evaluating eddy current compensation in this work utilized the boundary element method to derive the induced eddy current in a representative bore surface and the wire pattern of a research prototype X-gradient. The induced eddy current had prominent X and ZX components as shown in Figure 6-2. In all three configurations the residual field coefficients were reduced and in the 8-channel case a large component of the ZX coefficient remained however, in the 16- and 24-channel configurations this was successfully reduced.

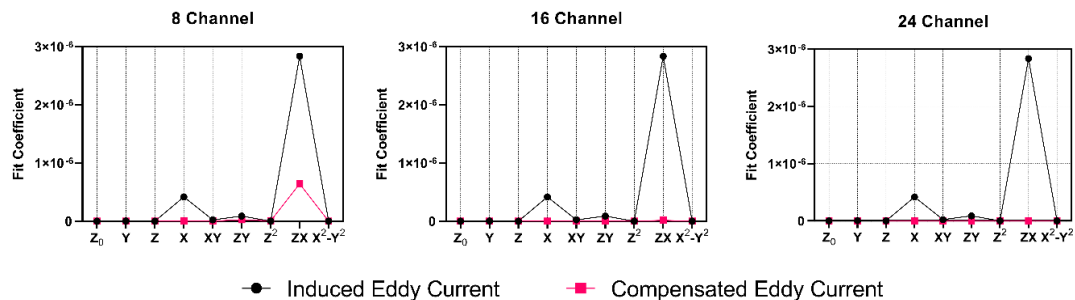


Figure 6-2: Multi-Coil Static Eddy Current Compensation

Spherical harmonic decomposition of the induced eddy current magnetic field from a representative asymmetric X-gradient pre- and post-compensation.

All three configurations were able to recreate spherical harmonics over a 0.20 m diameter spherical volume as shown in Figure 6-3 with the 24-channel configuration performing better than both the 16- and 8-channels.

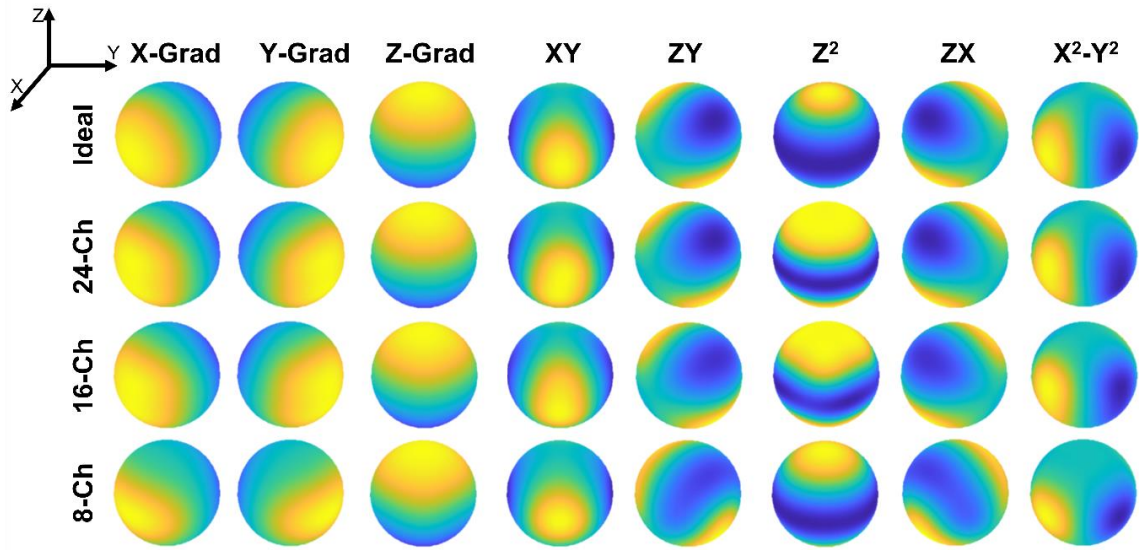


Figure 6-3: Generating Spherical Harmonic Fields

Simulated surface magnetic field plots for 1st and 2nd order spherical harmonic fields (gradients and shim fields) for the ideal case, 24-channel, 16-channel, and 8-channel cases.

To evaluate the performance of compensating for dynamic eddy currents I employed experimental data and at each measurement time point solved for a current profile within the matrix array coil that approximates the inverse of the magnetic field induced by the eddy current. The compensated and uncompensated field profiles are shown in Figure 6-4. It is clear from this figure that increasing the number of channels decreases the strength of the eddy current and increases its decay time. It is important to note that these all used a single loop of wire for each channel and as a result the maximum required current for the 8-, 16-, and 24-channels were 6, 18, and 31 A, respectively. In the case of the smaller loops of wires used in the higher channel configurations the current required is outside of the range that would be feasible given amplifiers that would be used to drive a setup like this. However, this can be solved in the manufacturing process by winding each current loop with multiple windings as this will increase the magnetic field efficiency.

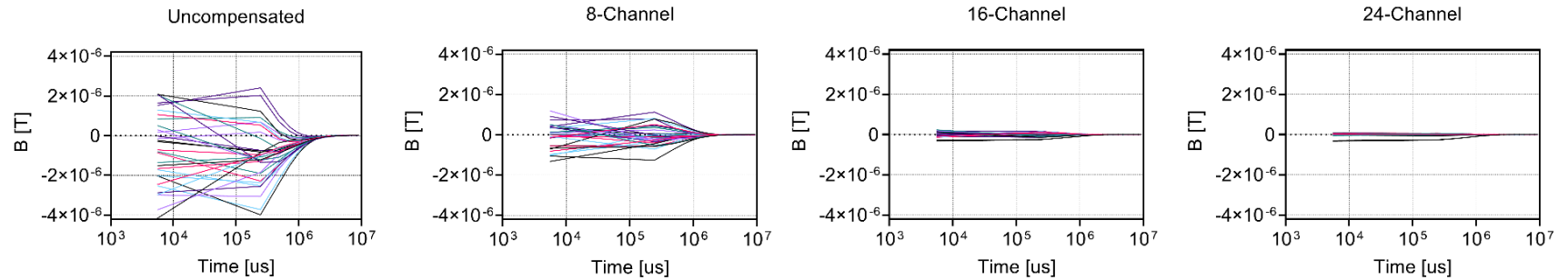


Figure 6-4: Dynamic Eddy Current Compensation

Experimental magnetic field profile and simulated post-compensation magnetic field profile for induced eddy current fields. Experimental measurement points are distributed over the surface of a spherical volume and each take measurements of the magnetic field over time at their specific location on the sphere. This is represented in the above plots as a single line for each measurement location. The multi-coils are used to create the inverse of the magnetic field at each measurement point location over time and the two fields are superimposed leaving a residual field that remains after compensation.

As shown in Table 6-2 each coil configuration was able to significantly reduce the magnitude of the eddy current field when looking at the maximum absolute field point over the time series. A maximum reduction of 69% was observed in the 8-channel case and a maximum reduction of 92% was observed in both the 16- and 24-channel cases. Although, the maximum absolute field reduction was the same in both the 16- and 24-channel cases overall there was a greater reduction in the 24-channel case overall with two points contributing to the maximum field point in both the 16- and 24-channel cases.

Table 6-2: Dynamic Eddy Current Compensation Field Reduction

	Channels					
	Uncompensated	8	16	24	SH Shims + Grads + B ₀	8-Channel + Grads + B ₀
Max Absolute Field [μ T]	4.2	1.3	0.32	0.33	0.64	0.84
Percent Reduction [%]	0	69	92	92	85	80
Max Absolute Compensation Current [A]	0	6.5	18	31	0.3	7

Comparison with spherical harmonic shim coils in reducing the absolute induced eddy current magnetic field.

Since this study was concerned with showing the utility of implementing a matrix array in the space normally occupied by spherical harmonic active shims, I also explored dynamic eddy current compensation using the B_0 , gradients, and spherical harmonic active shim channels for a total of 10 independently driven channels. The maximum residual field and the percent reduction in the eddy current field are given in Table 6-2. Performance of the spherical harmonic shim coils in eddy current compensation between the 8- and 16-channel cases in reducing the absolute field magnitude. It is important to note that the spherical harmonic case utilized B_0 and gradient compensation whereas the multi-coil matrix array did not. In order to explore this further I performed an additional simulation with the 8-channel matrix array combined with B_0 and gradient compensation. The gradient field profiles used for this was the wire pattern from the gradients used in the static eddy current case. The addition of the B_0 and gradient fields improved the maximum field reduction in the 8-channel case however it performed worse than the spherical harmonic active shim case. However, this motivates the potential application of using matrix array coils to act as shims and actively compensate for eddy currents during an imaging sequence. Especially as adding channels to the matrix coil may be more feasible than adding additional spherical harmonic layers to the gradient housing. Traditionally designed spherical harmonic shims are by nature designed over predetermined volumes traditionally using spherical volumes. A matrix coil technique, however, is not optimized for particular imaging region shapes and may provide useful in compensating and shimming non-spherical volumes such as ovals which may better encapsulate certain anatomical regions.

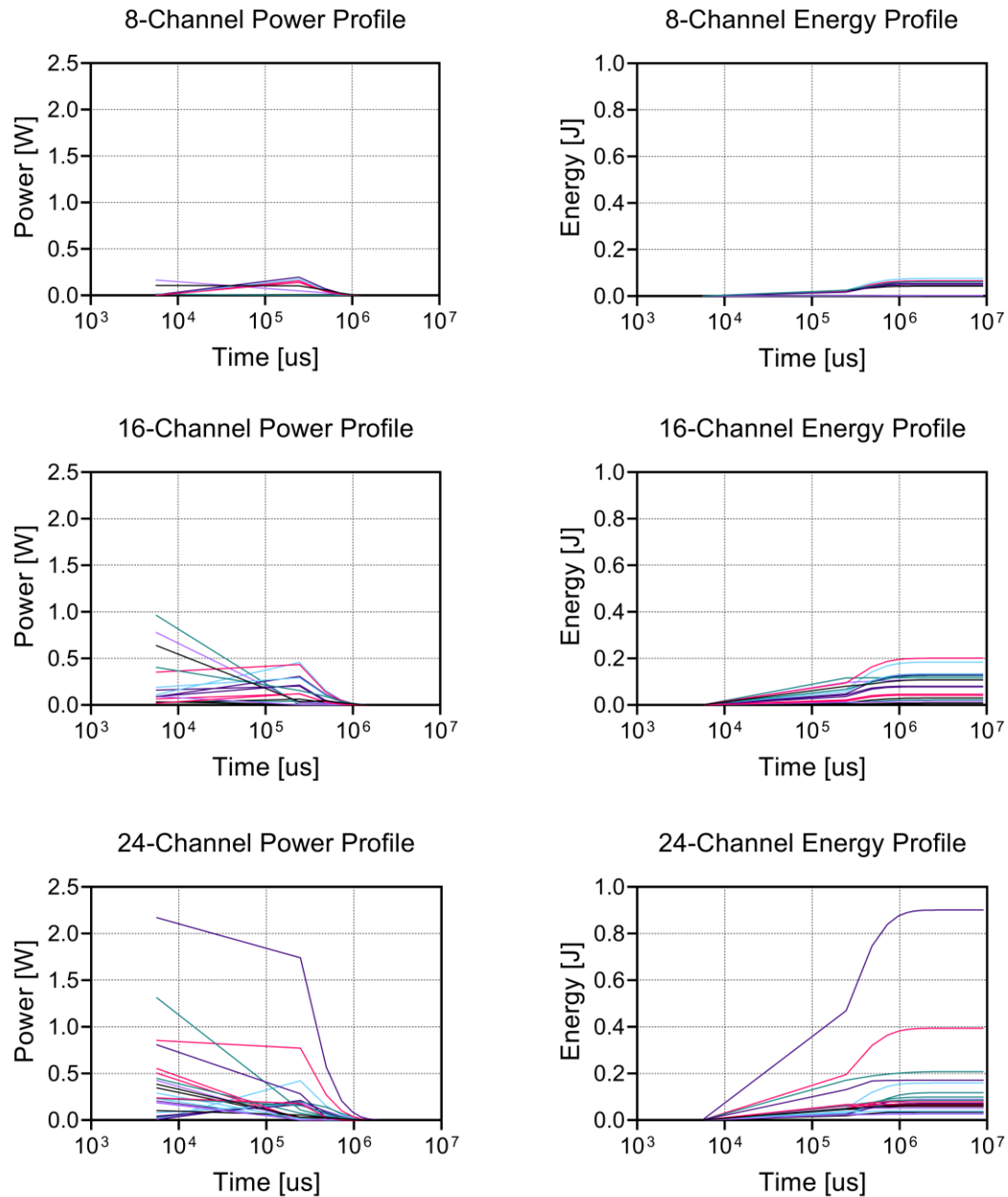


Figure 6-5: Dynamic Eddy Current Compensation Power and Energy Plots

Simulated Power vs Time and Energy vs Time plots over the duration of eddy current compensation using the multi-coil arrays. Each line represents a single current loop (channel) out of 8, 16, and 24 total current loops for the 8-, 16-, and 24-channel current arrays, respectively.

This study is not without limitations. When designing the configuration of the current loops I did not perform optimization on the position and size of the channels. A small study, not shown, was performed on the 8-channel coil to determine the coil size and orientation

however this was not extensive. The metric used for selection of the configuration orientation and channel sizes was evaluation of the compensation of the static eddy current magnetic field induced in a nearby conducting surface. The chosen configuration was the one that best reduced the spherical harmonic coefficients after compensation. Another consideration is in accounting for Joule heating during use, which will lead to heating of the wire and potentially require cooling considerations. Cooling can be accomplished by using larger diameter wire decreasing the electrical resistance, by utilizing hollow wire and implementing direct water cooling or by increasing the winding density of the current loop. Increasing the winding density will decrease the current required and increase the electrical resistance of the current loop however, since Joule heating increases as I^2R , this will lead to an overall decrease in wire heating. Looking at the time series data and the maximum compensation current for a single loop with resistances given in Table 6-2 it can be seen that during dynamic compensating the maximum instantaneous power through a single loop is: 0.2 W, 1.0, W, and 2.2 W, for the 8-, 16-, and 24-channel cases, respectively. With the maximum total energy for a single loop being 0.7, 1.8, and 8.2 J and the total energy over all loops as 3.2, 13, and 27.5 J for the 8-, 16- and 24-channel cases, respectively. This demonstrates the effect of the larger required current as the loops decrease in radius and motivates the use of multiple windings to decrease this. It should also be noted that construction of the C-matrix used in calculating the current weighting which best estimates the time dependent eddy current field data uses the complete set of measurement positions. This may lead to a small bias in performance as it provides no way to evaluate performance outside of the measurement positions. Due to this, it may be worth exploring compensation using a subset of measurement points for the calculations and the complete set of measurement points for evaluation. Importantly, this is also true for the calculation of the shim weightings used in the multi-coil/shim comparison.

In this proof-of-concept study I have demonstrated the use of a matrix array coil to be placed within a gradient coil housing as a method of compensating eddy currents in head-only MRI platforms. I explored the effect on performance of increasing the number of independently driven channels from 8 to 24 and observed an increase in performance as measured by creation of example magnetic fields, reducing spherical harmonic coefficients in a static eddy current simulation and reducing the magnitude of eddy currents using

experimental eddy current data. I believe that as the drive for higher performance and unique geometry gradient coils increases that implementation of a multi-coil matrix array designed for active eddy current compensation may enable improved imaging performance. Finally, while this work demonstrated the feasibility of spherical imaging regions a technique such as the one presented here is not limited to predetermined geometries and can be extended to non-spherical imaging regions without modification.

6.5 References

- [1] Forbes LK, Crozier S: A novel target-field method for magnetic resonance shim coils: III. Shielded zonal and tesseral coils. *J Phys D Appl Phys* 2003; 36:68–80.
- [2] Turner R: Gradient coil design: A review of methods. *Magn Reson Imaging* 1993; 11:903–920.
- [3] Eberlein E, Schmitt F, vom Endt A, Kimmlingen R, Riegler J: A high-performance head gradient coil for 7T systems. *Proc 14th Sci Meet Int Soc Magn Reson Med* 2006; 11:1370.
- [4] DeMeester G, Shvartsman S, Morich M: Discrete Design of an Insert Gradient Coil for Head Imaging in High Field MRI. *Proc 14th Sci Meet Int Soc Magn Reson Med* 2006; 14:1371.
- [5] Poole M, Bowtell R: Novel gradient coils designed using a boundary element method. *Concepts Magn Reson Part B Magn Reson Eng* 2007; 31B:162–175.
- [6] Turner R, Bowley RM: Passive screening of switched magnetic field gradients. *J Phys E* 1986; 19:876–879.
- [7] Hidalgo-Tobon SS: Theory of Gradient Coil Design Methods for Magnetic Resonance Imaging. *Concepts Magn Reson Part A* 2010; 36:223–242.
- [8] Juchem C, de Graaf RA: B₀ magnetic field homogeneity and shimming for in vivo magnetic resonance spectroscopy. *Anal Biochem* 2017; 529:17–29.

- [9] Gao Y, Mareyam A, Sun Y, et al.: A 16-channel AC/DC array coil for anesthetized monkey whole-brain imaging at 7T. *Neuroimage* 2020; 207(August):116396.
- [10] Han H, Song AW, Truong TK: Integrated parallel reception, excitation, and shimming (iPRES). *Magn Reson Med* 2013; 70:241–247.
- [11] Littin S, Jia F, Layton KJ, et al.: Development and implementation of an 84-channel matrix gradient coil. *Magn Reson Med* 2018; 79:1181–1191.
- [12] Peeren GN: Stream function approach for determining optimal surface currents. *J Comput Phys* 2003; 191:305–321.
- [13] Harris CT, Haw DW, Handler WB, Chronik BA: Shielded resistive electromagnets of arbitrary surface geometry using the boundary element method and a minimum energy constraint. *J Magn Reson* 2013; 234:95–100.
- [14] Handler WB, Bindseil G, Chaddock R, et al.: Design and construction of a gradient coil for high resolution marmoset imaging. *Biomed Phys Eng Express* 2020; 6:45022.

Chapter 7

7 Thesis Conclusions and Future Directions

The research outlined in this thesis presents the beginning in the development of a novel MR scanner configuration which aims to enable head and neck imaging in a compact head-optimized scanner geometry. This would enable implementation of high-performance imaging of the neck in emergency room environments and the development of a comprehensive stroke imaging platform for cervical spine and brain imaging. However, there is further work that must be performed before this is possible. This chapter will summarize and outline the work performed in this thesis as well as discuss some of the future work which must be performed to take this research to the next stage.

7.1 Overview and Research Questions

Looking back to Chapter 1 the question which motivated this research was “*can we design an MRI gradient coil for compact head-optimized geometries which allows imaging of the cervical spine*” and this question has remained throughout each of the chapters.

Chapter 2 expanded this by asking the question “*what trade-offs in electromagnetic performance do we observe by adding cut-outs to a cylindrical gradient coil and moving the imaging region from the center further down the patient end?*”

Chapter 3 took the experiences from Chapter 2 and asked, “*how do we balance the performance in the transverse axes due to the asymmetrical loss in conducting surface?*”

With the designs of the gradient coils explored, it was time to determine the location within the gradient housing at which the shim coils would be placed. This could take form in one of two places, near the primary windings requiring a shoulder cut-out or near the shield windings allowing the use of a full cylindrical surface. I asked the question in Chapter 4 “*what electromagnetic trade-offs do we make by placing the spherical harmonic active shims at these two distinct locations?*”

With the gradient and shim designs completed the next MR system to be explored was in designing an RF coil. Development of unique geometry RF coils using traditional

techniques is extremely difficult, if possible. However, this work was primarily focused on comparatively low field MRI at 0.5T which may allow design of unique geometry RF coils like a shoulder cut-out RF transmit coil. Next, in Chapter 5 I asked the question “*can we use the design methods we use for gradients and shims and apply it towards low-frequency RF coils?*”

Finally, motivated by the complexity of induced eddy currents in asymmetric and shoulder cut-out MRI gradient coil systems I wanted to explore hardware methods of overcoming this problem. In Chapter 6 I asked the question “*can we use a multi-coil matrix array to dynamically compensate for complex induced eddy currents?*”

7.2 Summary and Conclusions

In Chapter 2 I demonstrated that adding cut-outs to a cylindrical coil while compensating for the cut-outs with extra length leads to small changes in performance when compared to a simple cylindrical surface. I also demonstrated that moving the imaging region towards the patient end, regardless of cut-out lengths decreases performance when holding efficiency constant. This performance decrease is most noticeable when looking at shielding and inductance. I also observed the difficulty in balancing the transverse axes performance due to the asymmetrical loss of conducting surface. I concluded from this work that designing an asymmetric shoulder cut-out gradient coil with a compact inner radius is possible while maintaining performance suitable for high quality imaging.

In Chapter 3 I demonstrated the feasibility of designing a gradient configuration I have denoted the X-Mode Gradient Coil, in which the transverse axes are rotated by 45° with respect to the cartesian axes. This allows the transverse axes to have similar performance as each other with no noticeable difference in performance. I also modified the design geometries compared to Chapter 2 to accommodate a wider range of patient sizes and included real-field based force and torque balancing into the design study to enable use within the xMR Labs 0.5T MR scanner. I concluded in this work the feasibility of designing a unique configuration X-Mode Gradient Coil for use in our head-optimized compact 0.5T scanner. With available in-house gradient amplifiers this configuration would be capable

of maximum gradient strengths of over 80 mT/m at slew rates above 400 T/m/s enabling high-performance imaging.

In Chapter 4 I explored the design of spherical harmonic active shims by designing two sets at different radii. The first set implemented a shoulder cut-out and a smaller radius, whereas the second consisted of full cylinders and a larger radius. I determined that the smaller radius shims can be driven harder and faster but suffer in homogeneity compared to the full cylinder shims. To overcome this, I explored the design of a complementary set of electromagnets using the residual field as field targets demonstrating the feasibility of purpose-built compensation coils. Here, I concluded that the trade-off in field homogeneity in this small study was not worth the benefit in switching speed and efficiency and for shimming and eddy current compensation the choice should be full shims further away. However, it may be worth experimentally exploring the extra compensation coil implementation.

To explore the possibility of unique geometry RF transmit coils in Chapter 5 I explored the design and construction of a pair of transmit RF coils designed using the BEM. In this work I found that the constructed RF coil had field artefacts not agreeing with simulation. After exploring full-wave RF simulations, I hypothesized that this was due to the large current path in the constructed coil and that by manufacturing a coil with a shorter current path this method may be viable. Future work should include splitting the constructed coil and comparing the measurement magnetic field with simulations. Lastly, when performing a design study to construct a shorter coil it may be important to consider the coupling between the gradients and RF coil during operation.

Finally, in Chapter 6 I explored the design of a multi-coil matrix array to compensate for induced eddy currents throughout an imaging sequence. I showed that across a range of independently driven channels ranging from 8 to 24 that each can successfully reduce the spherical harmonic coefficients in an induced field and using experimental data demonstrated the real-world feasibility of this approach. I demonstrated their performance by comparing the matrix array compensation to a traditional spherical harmonic set.

7.3 Limitations

Study specific limitations were discussed within their respective body chapters within this thesis. However, discussion of some of the major limitation throughout are important to mention here.

Unfortunately, when designing gradient coils the shielding metric which is considered acceptable is not known. Therefore, it is not uncommon when choosing a selected design to choose the design with performance one desires that has the minimum power deposited into the bore. While this method works, it runs the risk of leaving performance on the table if worse shielding is tolerable but unknown.

The dynamic eddy current compensation work demonstrates a promising result in silico when it comes to reducing the parasitic magnetic fields. However, for this to find use and contribution within the MR community experimental verification must be performed.

Lastly, it is important to note and discuss the fact that the wire patterns for Chapter 2 and Chapter 4 cannot be directly implemented without minor modifications. In Chapter 2 the study was primarily concerned with observing the bulk trends associated with adding cut-outs and shifting the imaging region and did not use realistic field data for torque balancing. Similarly, in Chapter 4 the wire patterns were not designed with any previous gradient wire patterns in mind to pair them with in terms of minimizing inductive coupling between them. This is important and would be required before implementation. However, like Chapter 2 the bulk trends were the overall design goal. These two chapters provide more of a “general understanding” of the designs than specific designs to be machined and implemented.

7.4 Future Directions

This thesis represents the first steps towards implementing a head and neck shoulder cut-out gradient coil for implementation on the xMR Labs 0.5T compact MR scanner. However, much of the work has been focused on electromagnetic design studies answering the trade-offs and benefits of implementing a setup such as this. There are still unanswered questions and unfinished work spanning both computational methods and the construction and verification of the gradients, shims and multi-coils presented in this thesis.

7.4.1 Computational

As previously mentioned, while the shielding metric used in the BEM design is a good tool for comparing the relative performance between designs it fails to give the entire electromagnetic picture. Fundamentally, it is unknown what bore power gives “acceptable shielding” and the static eddy current results are not necessarily indicative of the complex time dynamics within a full MR system. During the design stage these BEM derived metrics are useful for narrowing down the pool of potential candidates and gleaning the trade-off in shielding as geometry changes. However, separate software such as CST Studio Suite capable of low frequency magnetoquasistatic time domain simulations can give a broader understanding of the time dynamics of eddy current generation, heating and the resultant field. Unfortunately, these simulations are incredibly time consuming, and it is impractical to perform them on the potentially thousands or tens of thousands of gradient candidates that can be designed during a design study. As such, this may be implemented on a significantly smaller subset of candidates perhaps when deciding between less than 10 coils for each axis. It may be worth exploring the relationship between BEM derived metrics and full simulation results across a range of design gradients with varying bore power, eddy current fields and efficiencies to determine a stronger understanding of these metrics as they relate to the dynamic power information. However, it should be noted that in the authors experience the BEM derived and full simulation results are highly correlated however, it is still worth potentially exploring.

In Appendix A, I outline the utility of using surface eigenmodes to design gradient coils and this work is currently in an early, incomplete state with many avenues of future work possible. While the proposed methods of removing eigenmodes from the design study has been focused on symmetry and spatial variation there still has yet to have been a complete design study implementing either of these techniques and has only been shown as a proof-of-concept.

7.4.2 Construction and Verification

Unfortunately, the designs presented here in this work have yet to have been constructed and their utility in enabling neck imaging and eddy current compensation has not been

demonstrated experimentally. This is important before drastic conclusions can be drawn about these designs and is the logical next step in extending this work. Designing the gradient coil with a complimentary shim set would require modifications to the current gradient design techniques within our lab which is further exacerbated if all hollow wire is to be implemented for improved cooling. While the electromagnetic design techniques used in this thesis have been well validated through the design and construction of a significant number of research gradient coils across a range of field strengths the designs presented here may require extra care in mapping electric fields to avoid unnecessary cardiac stimulation with the cardiac region being located closer to the imaging region.

7.5 Significance and Impact

This thesis ultimately builds on the foundation of shoulder cut-out gradient coils which have been the interest of literature or commercial/research implementations. To date, implementations of gradient coils with shoulder cut-outs have not been developed for improving neck imaging but instead increasing patient comfort or ensuring the brain is contained within the linear region of the gradient coil without a significant imaging region shifted towards the patient end. In this work, I was focused on using this type of geometry to allow a significant portion of the linear region to extend into the cut-out region to allow imaging of the lower cervical vertebra while still maintaining superior brain imaging. This thesis expands the current MRI systems development literature in different ways:

The first three body chapters present a complete design study in the design of a neck and head imaging gradient coil and complimentary shim set. This work presents the first design study on the relative performance trade-offs across a range of imaging region offsets and cut-out lengths gaining insight into the feasibility of a dual neck and head gradient coil for compact scanners. Next, I presented the unique gradient coil configuration to mitigate some of the performance issues gleaned in the shoulder cut-out gradient coil which may benefit other implementations such as head-optimized shoulder cut-out gradients to balance their transverse axis performance regardless of the anatomical target. I presented the first exploration of shim coil locations in a compact shoulder cut-out gradient coil. Although previous work has shown the design of shoulder cut-out shim coils, I have expanded on this by determining the relative trade-offs in radial positioning which is an important

consideration when optimizing the performance of the spherical harmonic shims. In this work, I have also demonstrated the feasibility of using purposely designed electromagnets to compliment the traditional spherical harmonic shims.

The next focus of this thesis was on the experimental design and construction of a low-frequency RF coil to demonstrate the use of gradient coil design techniques towards RF coils. While this chapter did not reach the design goals of a functional and artefact free RF coil, when compared to simulations, this provided a first step towards applying these techniques for head-optimized sized coils and motivates further study exploring shorter coils which may be less homogeneous but still provide acceptable performance.

Finally, motivated by the complexity of the induced eddy currents in asymmetric and unique geometry gradients I demonstrated, for the first time, the potential use of a matrix array coil in compensating for eddy current fields. Although these hardware configurations have been shown to be useful in static and dynamic shimming and creation of arbitrary fields this was the first *in silico* demonstration of the potential utility of implementing a matrix array in compensating eddy currents dynamically. I also demonstrated they can be placed within the gradient housing in the interest of space within a compact gradient coil.

Appendices

Appendix A: Stream Function Performance Functional

A.1 Creation of a Performance Functional

The introduction of a performance functional accomplishes two things. First, it allows fine tuning the relative importance of various electromagnetic features of the electromagnet such as field homogeneity, heating, and shielding. This is important because one desires electromagnets to be designed that achieve certain standards. Second, it reduces the problem to a single solution satisfying the design problem and functional specifics. I begin by defining a performance functional U and incorporating the terms of importance into it to be used in the design process. This isn't an exhaustive list but instead a description of the relevant characteristics to this work. In practice, anything that can be written in terms of current density can be added to the performance functional.

A.2 Calculating Magnetic Field

The first thing to be added to our performance functional is the ideal magnetic field profile that is desired. The goal is to produce a magnetic field that best matches this target magnetic field. This is specified during the design process and can take any form. It is defined by a set of k target points, \mathbf{r}_k , each with a corresponding magnetic field value $B_z^{\text{tar}}(\mathbf{r}_k)$

Since anything that can be written in terms of the current density can now be written in terms of the stream function we can write the z -component of the magnetic field as follows:

Starting from the magnetic vector potential $\mathbf{A}(\mathbf{r})$. The magnetic field $\mathbf{B}(\mathbf{r})$ can be computed directly:

$$\mathbf{A}(\mathbf{r}) = \frac{\mu_0}{4\pi} \int \frac{\mathbf{J}(\mathbf{r}')}{|\mathbf{r} - \mathbf{r}'|} d^3r' \quad (\text{A.1})$$

$$\mathbf{B}(\mathbf{r}) = \nabla \times \mathbf{A}(\mathbf{r}) \quad (\text{A.2})$$

Using these relationships, Equation 1.23 and expanding further we can write the z -component as:

$$B_z(\mathbf{r}) = \frac{\mu_0}{4\pi} \sum_{n=1}^N I_n \int_{S'} \left[\frac{J_{nx}(\mathbf{r}')(y - y') - J_{ny}(\mathbf{r}')(x - x')}{|\mathbf{r} - \mathbf{r}'|} \right] dS' \quad (\text{A.7})$$

It is convenient to write the integral as:

$$c_{nz}(\mathbf{r}) = \frac{\mu_0}{4\pi} \int_{S'} \left[\frac{J_{nx}(\mathbf{r}')(y - y') - J_{ny}(\mathbf{r}')(x - x')}{|\mathbf{r} - \mathbf{r}'|} \right] dS' \quad (\text{A.8})$$

Which allows the convenient representation of the B_z component of the magnetic field to be expressed as the sum of all node contributions:

$$B_z(\mathbf{r}) = \sum_{n=1}^N I_n c_{nz}(\mathbf{r}) \quad (\text{A.9})$$

In practice, the c matrix is pre-computed allowing direct calculation of the magnetic field based on a stream-function residing on the surface to be easily calculated for any stream function. With the z-field contribution at point k from all nodes given as:

$$B_z(r_k) = \sum_{n=1}^N (I_n C_n(r_k)) \quad (\text{A.10})$$

It is now possible to incorporate the deviation from our ideal magnetic field profile into our functional as follows:

$$U = \frac{1}{2} \sum_{k=1}^K \left[\sum_{n=1}^N (I_n C_n(r_k)) - B_z^{\text{tar}}(r_k) \right]^2 \quad (\text{A.11})$$

$$U = \frac{1}{2} \sum_{k=1}^K [B_z(r_k) - B_z^{\text{tar}}(r_k)]^2 \quad (\text{A.12})$$

Here, the functional now includes the least squares difference between the user defined target points and the produced magnetic field profile. It is possible to include individual target point weighting coefficients if the design process requires it, or if there is trouble

achieving homogeneity across certain planes. However, in this most basic form the weights of the individual target points are unity.

A.3 Calculating Power

The next consideration is the dissipative power within our electromagnet. It is simple to calculate as power is directly related to the surface current density as follows:

$$P = \frac{\rho}{t} \int_{S'} |\mathbf{J}(\mathbf{r}')|^2 dS' \quad (\text{A.3})$$

Here, P is the dissipative power within the electromagnet, ρ is the resistivity of the surface, t is the coil surface thickness and $\mathbf{J}(\mathbf{r})$ is the current density on the surface. Using the formulation of Poole and Bowtell (1) in terms of the parameterizing the of power dissipation in terms stream function representation of the current density this can be approximated as:

$$P = \sum_{n=1}^N \sum_{m=1}^M I_n I_m R_{nm} \quad (\text{A.4})$$

With R_{nm} being the self-resistance matrix of the discretized mesh surface:

$$R_{nm} = \frac{\rho}{t} \sum_i \sum_j \begin{cases} (v_{ni} \cdot v_{nj}) A_j, & \Delta_{ni} = \Delta_{nj} \\ 0, & \Delta_{ni} \neq \Delta_{nj} \end{cases} \quad (\text{A.5})$$

Here, A_j is the area of the i^{th} mesh element belonging to the n^{th} node and v_{ni} (for $i = 1$ to N) describes a unit current flow on each of the N triangular elements, Δ_{ni} , associated with the n^{th} node.

With this the power term can be added to the performance functional as follows:

$$U = \frac{1}{2} \sum_{k=1}^K [B_z(\mathbf{r}_k) - B_z^{\text{tar}}(\mathbf{r}_k)]^2 + \frac{\beta}{2} \sum_{n=1}^N \sum_{m=1}^M I_n I_m R_{nm} \quad (\text{A.6})$$

$$U = \frac{1}{2} \sum_{k=1}^K [B_z(r_k) - B_z^{\text{tar}}(r_k)]^2 + \frac{\beta}{2} P \quad (\text{A.13})$$

The performance functional now contains the least squares difference in produced magnetic field and the power dissipated within the electromagnet. The term β can be modified during the design process to weight the relative importance between field homogeneity and power dissipation.

A.4 Incorporating Shielding

As discussed previously shielding of an electromagnet is important to reduce the stray magnetic field and minimize the interactions of the switching gradient coil with the surrounding environment. Incorporation of shielding in the BEM can be accomplished in a variety of ways. To incorporate a shield a second surface is added outside of the primary radius and a shielding method is chosen. This can be done by defining a second set of target field points with zero magnetic field or by additional minimization terms. In this thesis, I use the addition of a third surface representing the MRI bore, or cryostat, in which I want to minimize the induced power. To accomplish this the mutual inductance between the gradient coil and bore surfaces are computed as follows (2):

$$M^{\text{coil/cryo}} = \frac{\mu_0}{4\pi} \int_S \int_{S'} \frac{J_{\text{cryo}}(r) \cdot J_{\text{coil}}(r')}{|r_{\text{cryo}} - r_{\text{coil}}|} dS' dS \quad (\text{A.14})$$

Which can be written in terms of the discretized current basis function:

$$M^{\text{coil/cryo}} = \frac{\mu_0}{4\pi} \sum_{n=1}^N \sum_{m=1}^M I_n I_m \int_S \int_{S'} \left[\frac{J_{n,\text{cryo}}(r) \cdot J_{m,\text{coil}}(r')}{|r_{\text{cryo}} - r_{\text{coil}}|} dS' dS \right] \quad (\text{A.15})$$

From this, the induced eddy current stream function in the bore surface can be computed directly as:

$$I_n^{\text{cryo}} = -[L_{nm}^{\text{cryo}}] M_{mq}^{\text{coil/cryo}} I_q^{\text{coil}} \quad (\text{A.16})$$

Here, L_{nm}^{cryo} is the self-inductance matrix of the cryostat surface, $M_{mq}^{coil/cryo}$ is the mutual inductance between the coil surfaces and the bore surface relating node m on the bore surface to node q on the coil surface, and I_q^{coil} is the stream function at node q of the coil. The calculation of both self-inductance matrices is the same as previously described minimum inductance methods (2) which is similar in computation to the mutual inductance.

It is convenient to write this in terms of a coupling term as follows:

$$I_n^{cryo} = D_{nq} I_q^{coil} \quad (\text{A.17})$$

Where D_{nq} can be considered the coupling matrix between the gradient coil and cryostat surfaces. It relates the induced stream function, or eddy current, at the cryostat nodes with the stream function values at the coil nodes. With the eddy current stream function known it is as simple as calculating the dissipative power as previously done and the power deposited into the bore can be written as:

$$P^{cryo} = \sum_{n=1}^N \sum_{m=1}^M I_n^{cryo} I_m^{cryo} R_{nm}^{cryo} \quad (\text{A.18})$$

Or, written in terms of the coil stream function:

$$P^{cryo} = \sum_{n=1}^N \sum_{m=1}^M [D_{nq} I_q^{coil} D_{mk} I_k^{coil}] R_{nm}^{cryo} \quad (\text{A.19})$$

Incorporation of this power term in the functional allows a minimum bore power shielding method to be used which is the following:

$$U = \frac{1}{2} \sum_{k=1}^K [B_z(r_k) - B_z^{\text{tar}}(r_k)]^2 + \frac{\beta}{2} P + \frac{\gamma}{2} \sum_{n=1}^N \sum_{m=1}^M [D_{nq} I_n D_{mk} I_m] R_{nm}^{cryo} \quad (\text{A.20})$$

$$U = \frac{1}{2} \sum_{k=1}^K [B_z(r_k) - B_z^{\text{tar}}(r_k)]^2 + \frac{\beta}{2} P + \frac{\gamma}{2} P^{\text{cryo}} \quad (\text{A.21})$$

The performance functional now includes a shielding term with γ being the weighting of the importance of shielding. During the design process this term is also varied adding another dimension to the design space.

A.5 Incorporating Torque

Earlier it was mentioned that it is important that the gradient coils do not experience significant net torque during operation, and this is accomplished by including the torque on the gradient coil as part of the design functional. This requires the B_0 field that the gradient coil will be installed within and can be accomplished using a field map made experimentally or assuming an idealized B_0 field which is single valued throughout the entirety of the calculation points. A current density will experience a force when in the presence of an external magnetic field:

$$\mathbf{F} = \int [\mathbf{J}(\mathbf{r}) \times \mathbf{B}(\mathbf{r})] dV \quad (\text{A.22})$$

It follows that the torque is then:

$$\mathbf{M} = \int \mathbf{r} \times [\mathbf{J}(\mathbf{r}) \times \mathbf{B}(\mathbf{r})] dV \quad (\text{A.23})$$

With the discretized current density and considering a constant valued (B_0) external magnetic field only in the z-direction the torque, in the z-direction can be written as:

$$M_z = \sum_{n=1}^N I_n [B_0 \int_S (-J_{nx}(\mathbf{r})x - J_{ny}(\mathbf{r})y) dS] \quad (\text{A.24})$$

$$M_z = \sum_{n=1}^N I_n M_{nz} \quad (\text{A.25})$$

The other two directions M_x , and M_y are computed in similar ways and can all be incorporated into the performance functional as Lagrange multipliers constraining the net torque to zero as:

$$U = \frac{1}{2} \sum_{k=1}^K [B_z(r_k) - B_z^{\text{tar}}(r_k)]^2 + \frac{\beta}{2} P + \frac{\gamma}{2} P^{\text{cryo}} - \lambda_x \sum_{n=1}^N I_n M_{nx} - \lambda_y \sum_{n=1}^N I_n M_{ny} - \lambda_z \sum_{n=1}^N I_n M_{nz} \quad (1.51)$$

$$U = \frac{1}{2} \sum_{k=1}^K [B_z(r_k) - B_z^{\text{tar}}(r_k)]^2 + \frac{\beta}{2} P + \frac{\gamma}{2} P^{\text{cryo}} - \lambda_x M_x - \lambda_y M_y - \lambda_z M_z \quad (1.52)$$

The performance functional now includes Lagrange multipliers whose purpose is to constrain the net torque on the gradient coil to zero during operation.

A.6 From Functional to Wire Pattern

At this point the functional contains all the important parameters to the design. Differentiating and minimizing the functional with respect to the stream function values at each node and the relevant Lagrange multipliers yields:

$$\frac{\partial U}{\partial I_n} = \frac{1}{2} I_m c_{nk} c_{mk} - \frac{1}{2} B_k^{\text{tar}} + \frac{\beta}{2} I_m R_{nm} + \frac{\gamma}{2} [D_{nq} D_{mk} I_m] R_{nm}^{\text{cryo}} - \lambda_x M_{nx} - \lambda_y M_{ny} - \lambda_z M_{nz} = 0 \quad (1.53)$$

$$I_m [c_{nk} c_{mk} - \beta R_{nm} - \gamma D_{nq} D_{mk} R_{nm}^{\text{cryo}}] = c_{mk} B_k^{\text{tar}} + \lambda_x M_{nx} + \lambda_y M_{ny} + \lambda_z M_{nz} \quad (1.54)$$

$$\frac{\partial U}{\partial \lambda_x} = -I_n M_{nx} = 0 \quad (1.55)$$

$$\frac{\partial U}{\partial \lambda_y} = -I_n M_{ny} = 0 \quad (1.56)$$

$$\frac{\partial U}{\partial \lambda_z} = -I_n M_{nz} = 0 \quad (\text{A.26})$$

This can be conveniently written into matrix form:

$$\mathbf{Z} = \begin{bmatrix} c_{nk}c_{mk} - \beta R_{nm} - \gamma D_{nq}D_{mk}R_{nm}^{cryo} & M_{nx} & M_{ny} & M_{nz} \\ & M_{nx}^T & 0 & 0 & 0 \\ & M_{nx}^T & 0 & 0 & 0 \\ & M_{nx}^T & 0 & 0 & 0 \end{bmatrix} \quad (\text{A.27})$$

$$\mathbf{I} = \begin{bmatrix} I_n \\ \lambda_x \\ \lambda_y \\ \lambda_z \end{bmatrix} \quad (\text{A.28})$$

$$\mathbf{b} = \begin{bmatrix} c_{mk}B_k^{tar} \\ 0 \\ 0 \\ 0 \end{bmatrix} \quad (\text{A.29})$$

And finally written as:

$$\mathbf{ZI} = \mathbf{b} \quad (\text{A.30})$$

From this, the matrix is inverted and the stream function values at each node which produces the magnetic field profile of interest while minimizing the performance functional is calculated. To ensure the shape of the stream function is closed and constrained to the surface the stream function values on edges are constrained such that they are the same value. To accomplish this the relevant matrices are condensed by summing along these edges and uncondensed when solved for. This process is outlined in (3) and ensures the stream function will flow along the edge and not through it. To create wire patterns that can be machined for use in an MR scanner the stream function is contoured over the surface. An example transverse gradient mesh, stream function and wire pattern for a cylindrical gradient surface is shown in Figure A-1.

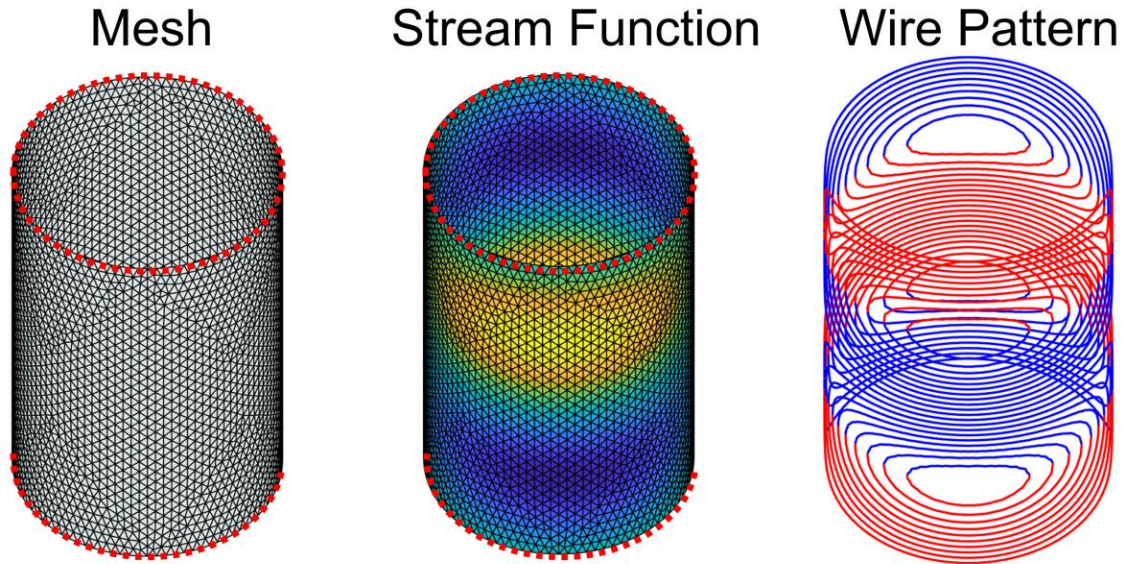


Figure A-1: Cylindrical Mesh, Stream Function, and Transverse Gradient Wire Pattern

Example mesh, computed surface stream function and final wire pattern. The red nodes indicate edges in which the stream function would be constrained through matrix condensing. The colour of the stream function plot shows node values linearly interpreted over the elements on the surface and the colour of the wire pattern shows the current direction with respect to the azimuthal direction.

A.7 References

- [1] Poole M, Bowtell R: Novel gradient coils designed using a boundary element method. *Concepts Magn Reson Part B Magn Reson Eng* 2007; 31B:162–175.
- [2] Harris CT, Haw DW, Handler WB, Chronik BA: Shielded resistive electromagnets of arbitrary surface geometry using the boundary element method and a minimum energy constraint. *J Magn Reson* 2013; 234:95–100.
- [3] Harris CT: Optimization of a boundary element approach to electromagnet design with application to a host of current problems in Magnetic Resonance Imaging. *Phd thesis, West Univ* 2013.

Appendix B: Designing MRI Gradient Coils using Surface Eigenmodes

Modifications to the BEM approaches used in this thesis may also provide benefits in terms of computational speed up or gradient performance. One method is using surface eigenmodes of the stream-function on the computational surfaces. Briefly, the allowed current modes in which the current density may take over the computational surface is governed by the resistance and self-inductance properties of the meshed surface and can be computed from the general eigenvalue problem:

$$\mathbf{R}\mathbf{U} = \mathbf{L}\mathbf{U}\mathbf{\Lambda} \quad (\text{B-1})$$

Where, \mathbf{R} is the resistance matrix of the surface, \mathbf{L} is the self-inductance matrix, \mathbf{U} is an eigenmode basis set of allowable current paths (with φ_m being the m^{th} eigenmode consisting of a stream function vector I_m) and $\mathbf{\Lambda}$ is the corresponding diagonal eigenvalue matrix. Using the allowed basis set to modify the performance functional and therefore the problem at hand the stream-function can then be solved for as a weighted linear combination of eigenbasis vectors. From this, it follows that the stream function for a single mode m can be calculated as:

$$\varphi_m = \sum_{n=1}^N I_{mn} \psi_n \quad (\text{B-2})$$

Where φ_m is the m^{th} eigenmode consisting of a stream function vector I_m with N node values and the total stream function of interest is then the weighted sum of each of these stream function vectors as follows:

$$I = \sum_{m=1}^{N_{\text{modes}}} W_m \varphi_m \quad (\text{B-3})$$

Here W_m is the weight for eigenbasis m comprising of a number of nodes given by N_{modes} , φ_m is the m^{th} eigenbasis vector and I is the total stream function on the computational surface which we are solving for.

For a simple minimum power design, we begin by writing the problem in terms of the weighting of the eigenmodes by defining an eigenmode field matrix:

$$C_{\varphi_i}(r_k) = \sum_{n=1}^N (\varphi_{in}(c_n(r_k))) \quad (\text{B-4})$$

This gives the field from eigenmode i at the field targets calculated using the original field matrix c which describes the field contribution from each node. We also define an eigenmode resistance matrix as follows:

$$R_{\varphi_i} = \sum_{n=1}^N \sum_{m=1}^M \varphi_{in} \varphi_{im} R_{nm} \quad (\text{B-5})$$

Which describes the resistance contribution for mode i . With this the minimum power functional can be written as:

$$U = \frac{1}{2} \sum_{k=1}^K \left[\sum_{i=1}^{N_{modes}} (W_i C_{\varphi_i}(r_k)) - B_z(r_k) \right] + \frac{\beta}{2} \left[\sum_{i=1}^{N_{modes}} W_i R_{\varphi_i} \right] \quad (\text{B-6})$$

With W_i being the weighting of eigenmode i . The functional is differentiated with respect to the weightings and a series of matrix equations are setup to solve for the W vector which gives the weighting for each eigenmode. Using the complete eigenbasis set provides no benefit and arrives at the same solution as using the traditional methods. However, by examining the eigenbasis set with a critical lens it is possible to observe particular basis vectors which negatively, or neutrally affect the problem which can be then removed for speed up or potential manufacturability. Figure B-1 shows the first three eigenbasis stream functions and their resultant wire pattern contours.

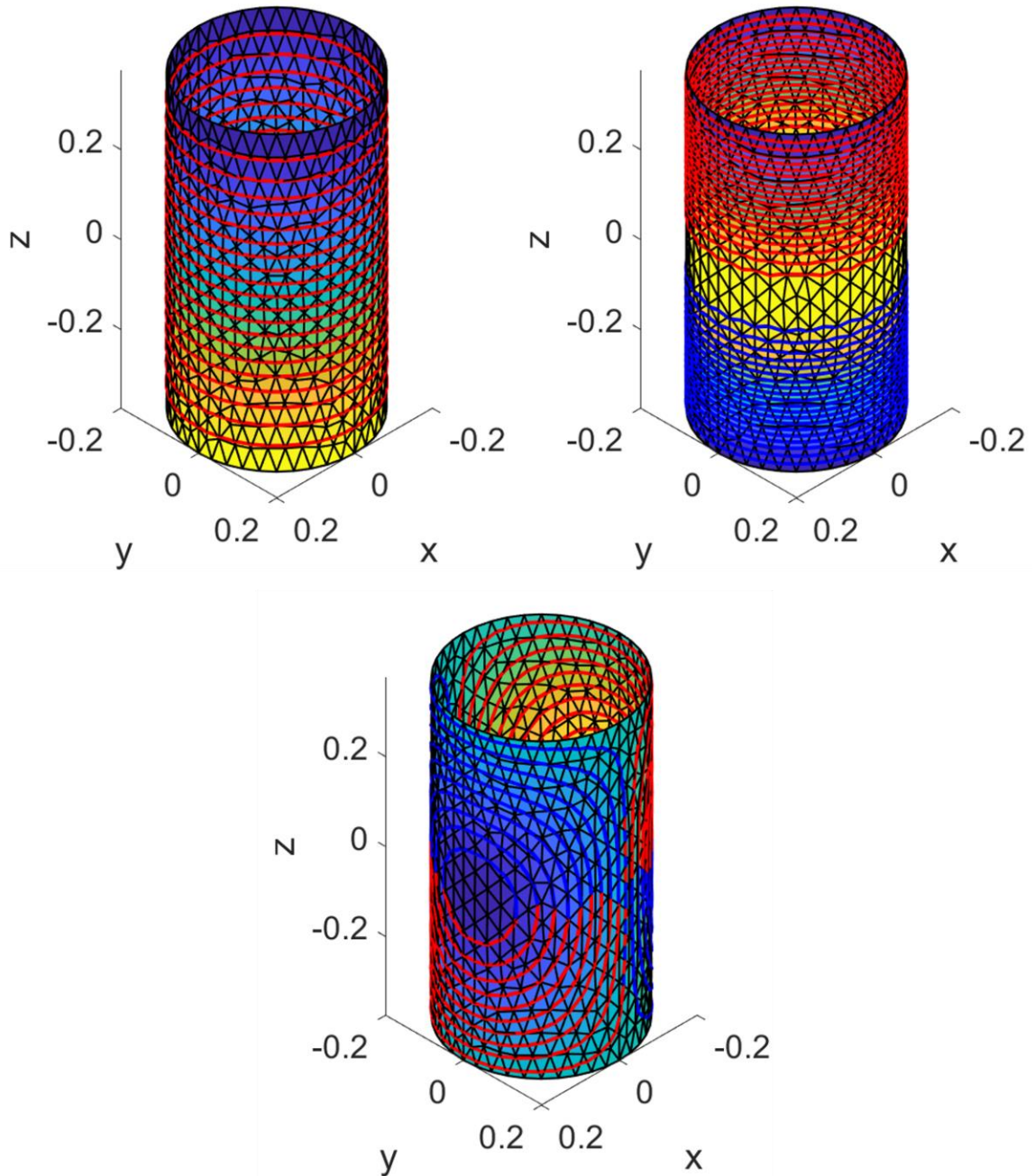


Figure B-1: Example Cylindrical Eigenmodes

Example eigenmode plots. Plot shows stream function node values linearly interpreted over the surface for example stream function eigenmodes with contoured wire pattern overlaid. Wire pattern colour indicates current direction with respect to the azimuthal direction.

Using the symmetry of the stream function and its produced magnetic field values it is possible to remove modes in which the desired symmetry to the problem is not found. An example of this is shown below for a Y-gradient coil using the entire eigenbasis set and a

condensed eigenbasis set where non-symmetric modes have been removed. Figure B-2 shows the computational surfaces, stream function and resultant wire contours and Table B-1 gives the simulated design parameters. Note the approximate reduction of $\frac{3}{4}$ of the modes corresponding to an equal decrease in computational time with minimal effect on derived metrics.

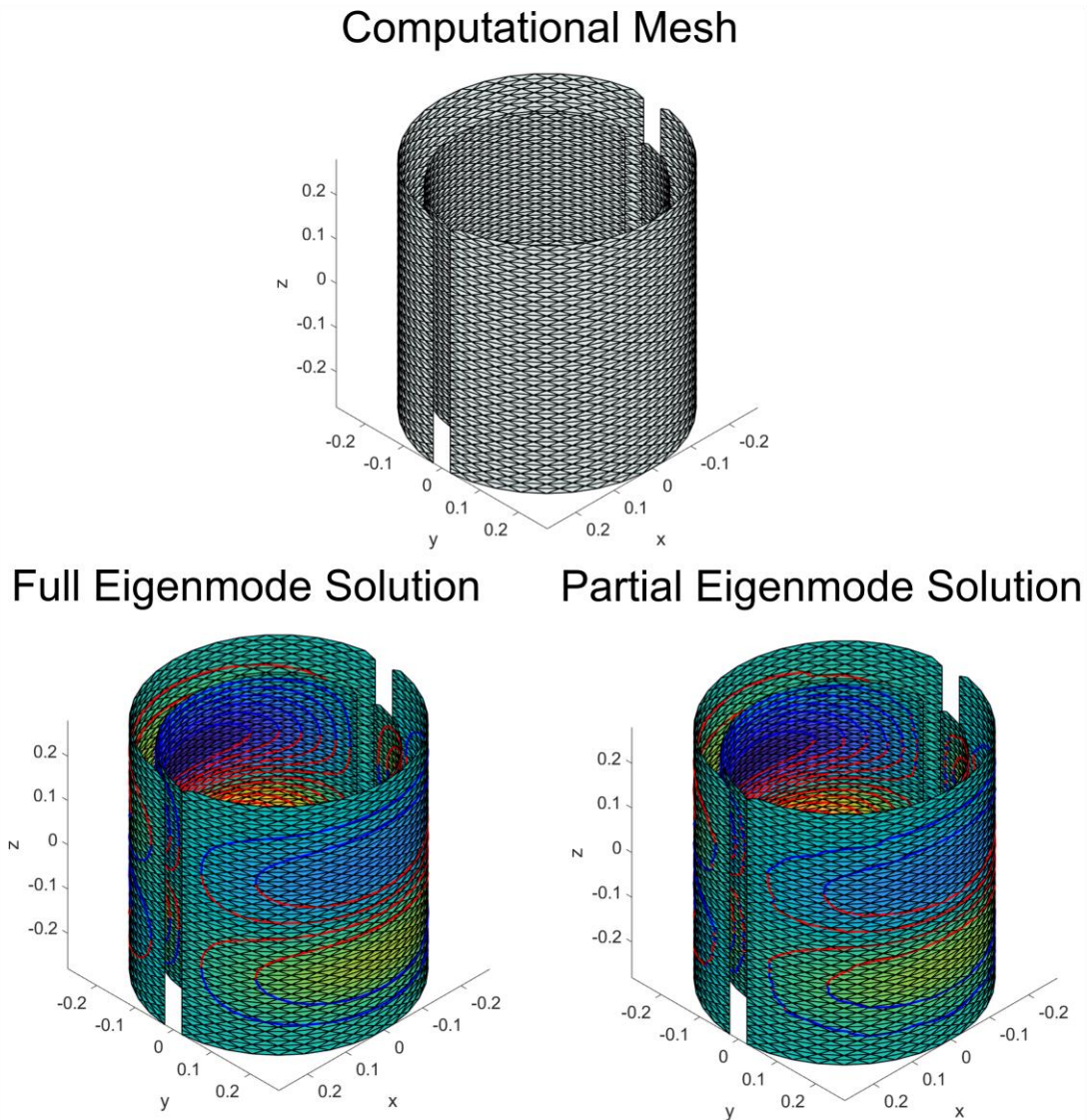


Figure B-2: Full vs Partial Eigenmode Solution Example

Example partial mode solution. Plot shows stream function node values linearly interpreted over the surface for example stream function eigenmodes with contoured wire pattern overlaid. Wire pattern colour indicates current direction with respect to the azimuthal direction.

Table B-1: Full vs Partial Eigenmode Solution Performance Parameters

Parameter	Full Mode Solution	Partial Mode Solution
Included Eigenmodes [n]	3433	907
Efficiency [mT/m/A]	0.08	0.08
Slew Rate [T/m/s]	3071	3138
DSV ₂₀ [m]	0.1	0.1
Bore Power [W]	1.0E-3	1.3E-5
Resistance [mΩ]	49	49
Minimum Wire Spacing [mm]	9	9
Elapsed Time [s]	25	6

DSV₂₀ = diameter of spherical volume where the gradient field deviates <20%.

It may be possible to extend this further by looking at the spatial variation in the eigenmodes and removing modes which have variations which are impractical to include in the design and then manufacture. Looking at a high order eigenmode Figure B-3 with the wire pattern superimposed on top this can be easily seen.

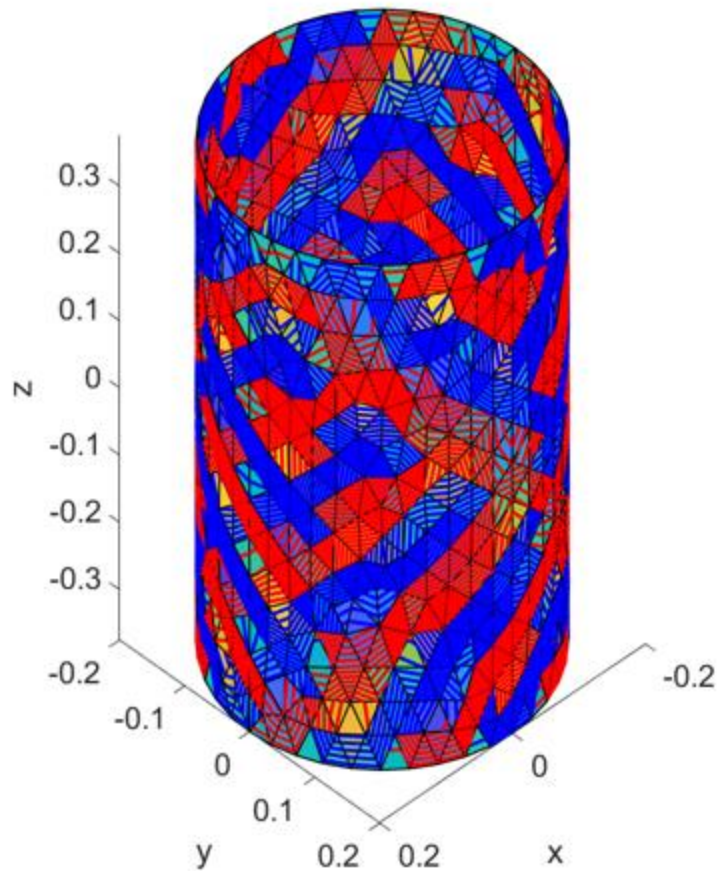


Figure B-3: Higher Order Eigenmode Spatial Variation

Example eigenmode plots. Plot shows stream function node values linearly interpreted over triangular elements on the surface with wire pattern contour overtop. Wire pattern colour indicates current direction with respect to the azimuthal direction.

The higher order terms contain the high frequency components, and the lower order terms the low frequency components. From this it may be possible to provide the majority of the performance and field profile using the lower orders and fill in the higher orders as needed to ensure the optimal coil performance. This may provide a significant benefit in speed up and manufacturing capabilities with current work ongoing to demonstrate the utility of this technique by converting the cylindrical eigenmode to a 2D plane and performing Fourier Analysis to observe the spatial frequencies that the mode contains of. This is visualized in Figure B-4.

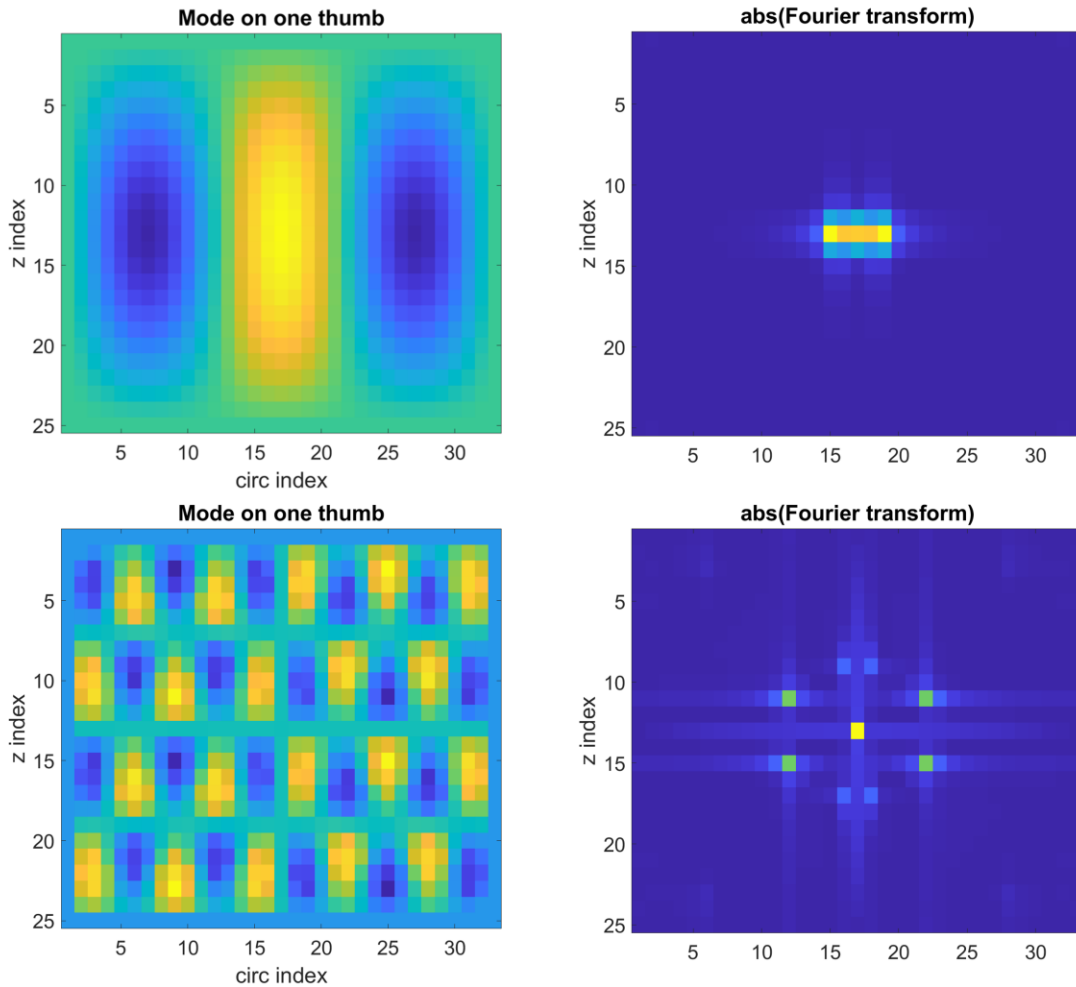


Figure B-4: Example Eigenmode Frequency Analysis

Flat plane representations of example stream function modes and the respective 2D Fourier transform demonstrating the spatial frequency variations contained in various eigenmodes.

From Figure B-4 we can see that the high spatial variation is observed in the frequency analysis of the 2D representation of the stream function. It may be possible to determine an absolute cut-off frequency that provides variations in the gradient wire pattern which are too difficult or impossible to manufacture for use. It may be also possible to use this technique to increase the performance of the designed gradient coils by exploring modes which have high interactions with the surrounding environment and investigating the designs with those removed.

Curriculum Vitae

Name: Eric J. Lessard

Post-secondary Education and Degrees:

The University of Western Ontario
London, Ontario, Canada
2017-2022 PhD. Medical Biophysics

The University of Western Ontario
London, Ontario, Canada
2015-2017 MSc. Medical Biophysics

University of Windsor
Windsor, Ontario, Canada
2008-2015 BSc. Physics

Honours and Awards:

International Society for Magnetic Resonance in Medicine
Educational Stipend Award
2016, 2019, 2020

Western Graduate Research Scholarship
2015-2022

Related Work Experience

Teaching Assistant
The University of Western Ontario
2019-2020

Teaching Assistant
University of Windsor
2014-2015

Publications:

E Lessard, HM Young, A Bhalla, D Pike, K Sheikh, DG McCormack, A Ouriadov and G Parraga. Pulmonary ³He Magnetic Resonance Imaging Biomarkers of Regional Airspace Enlargement in Alpha-1 Antitrypsin Deficiency, *Acad Radiol*, 24 (11), 1402-1411

A Ouriadov, E Lessard, K Sheikh and G Parraga. Pulmonary MRI Morphometry Modelling of Airspace Enlargement in Chronic Obstructive Pulmonary Disease and Alpha-1 Antitrypsin Deficiency, *Magn Reson Med*, 79 (1), 439-448

G Paulin, A Ouriadov, E Lessard, K Sheikh, DG McCormack and G Parraga. Non-Invasive Quantification of Alveolar Morphometry in Elderly Never- and Ex-Smokers *Physiol Rep*, 3 (10), 2015, e12583

Oral Presentations:

E Lessard, A Ouriadov, DPI Capaldi, DG McCormack and G Parraga, Novel Biomarkers of Lung Parenchyma Destruction and Emphysema Progression in COPD Using Inhaled Gas MRI Morphometry. American Thoracic Society Annual Scientific Meeting 2016 San Francisco CA May 13-18, 2016

A Ouriadov, E Lessard, DG McCormack and G Parraga, Can the Stretched Exponential Model of Gas Diffusion Provide Clinically-Relevant Parenchyma Measurements of Lung Disease? International Society of Magnetic Resonance in Medicine Annual Scientific Meeting 2016 Suntec City, Singapore May 7-13, 2016.

A Ouellette, E Lessard, AM Chertov, RG Maev. Real Time 2D Imaging of the Spot Weld Process, The American Society for Non-destructive Testing 23rd Research Symposium, March 27, 2014, Las Vegas, NV

Poster Presentations:

E Lessard, WB Handler, BA Chronik. Spherical Harmonic Active Shim Set Design for a Shoulder Cut-out MRI Platform. Submitted on November 10th, 2021 to the International Society of Magnetic Resonance in Medicine Annual Scientific Meeting 2022.

E Lessard, WB Handler, BA Chronik. The X-Mode Gradient: Improved Performance for Select Applications. International Society of Magnetic Resonance in Medicine Annual Scientific Meeting 2020.

DF Martinez, KJ Davieau, E Lessard, WB Handler, and BA Chronik. MRI Room Placement: The Effect of an Elevator Operation on Local Magnetic Environment. International Society of Magnetic Resonance in Medicine Annual Scientific Meeting 2020.

E Lessard, WB Handler, BA Chronik. Development of an MRI Gradient Coil for Use in a Compact Head-only MRI Platform Capable of Imaging C7 and Below. American Association of Physicists in Medicine and Canadian Organization of Medical Physicists Joint Annual Meeting 2020.

E Lessard, WB Handler, BA Chronik. The X-Mode Gradient: Improved Performance for Select Applications. Imaging Network of Ontario (ImNO), 18th Annual Imaging Network Ontario Symposium, Toronto, Ontario, March 26-27, 2020.

DF Martinez, KJ Davieau, E Lessard, WB Handler, and BA Chronik. MRI Room Placement: The Effect of an Elevator Operation on Local Magnetic Environment. Imaging Network of Ontario (ImNO), 18th Annual Imaging Network Ontario Symposium, Toronto, Ontario, March 26-27, 2020.

E Lessard, WB Handler, BA Chronik. Preliminary Design Exploration for a Head and Neck Gradient Coil: Effect of Shoulder Cut-out Length on Performance. International Society of Magnetic Resonance in Medicine Annual Scientific Meeting 2019.

E Lessard, WB Handler, BA Chronik. Design Exploration for a Head and Neck Gradient Coil: Effect of Shoulder Cut-out Length on Performance. Imaging Network of Ontario (ImNO), 17th Annual Imaging Network Ontario Symposium, London, Canada, March 28-29, 2019

A Ouriadov, E Lessard, F Guo, HM Young, A Bhalla, DG McCormack and G Parraga. Accelerated Diffusion-weighted ^{129}Xe MRI Morphometry of Emphysema. Imaging Network of Ontario (ImNO), 15th Annual Imaging Network Ontario Symposium, London, Canada, March 15-16, 2017.

A Ouriadov, E Lessard, F Guo, HM Young, A Bhalla, HO Coxson, DG McCormack and G Parraga. Biomarkers of Emphysema in COPD and Alpha-1 Antitrypsin Deficiency: ^{129}Xe MRI Morphomics. American Thoracic Society Annual Scientific Meeting 2017 Washington DC May 19-24, 2017.

A Ouriadov, E Lessard, F Guo, HM Young, A Bhalla, DG McCormack and G Parraga. Accelerated Diffusion-weighted ^{129}Xe MRI Morphometry of Emphysema in COPD and Alpha-1 Antitrypsin Deficiency Patients. International Society of Magnetic Resonance in Medicine Annual Scientific Meeting Honolulu, HI April 22-27, 2017.

E Lessard, A Bhalla, A Ouriadov, D Pike, DG McCormack and G Parraga, Longitudinal Three-Year Decline in Alpha-1 Antitrypsin Deficiency: Regional Worsening in Emphysema and Ventilation. Robarts Research Retreat 2016 London, Canada, June 13, 2016.

E Lessard, A Ouriadov, DG McCormack and G Parraga, Single Compartment model estimates of acinar duct measurements from inhaled noble gas MRI: Proof of Concept in alpha-1 antitrypsin deficiency emphysema. London Health Research Day 2016 London, Canada March 29, 2016.

A Bhalla, A Ouriadov, E Lessard, DG McCormack and G Parraga, Longitudinal MRI Morphomics: towards an understanding of response to therapy and disease progression in patients with Alpha-1 Antitrypsin Deficiency pulmonary emphysema. London Health Research Day 2016 London, Canada March 29, 2016. (Top 100 Poster)

E Lessard, A Ouriadov, DG McCormack and G Parraga, Single Compartment model estimates of acinar duct measurements from inhaled noble gas MRI: Proof of Concept in alpha-1 antitrypsin deficiency emphysema. International Society of Magnetic Resonance in Medicine Annual Scientific Meeting 2016 Suntec City, Singapore May 7-13, 2016.

E Lessard, A Bhalla, A Ouriadov, D Pike, DG McCormack and G Parraga, Longitudinal Three-Year Decline in Alpha-1 Antitrypsin Deficiency: Regional Worsening in Emphysema and Ventilation. American Thoracic Society Annual Scientific Meeting 2016 San Francisco CA May 13-18, 2016.

A Ouriadov, E Lessard, DG McCormack, G Parraga. Single-breath ^3He Whole Lung Morphometry in Alpha-1 Antitrypsin Deficiency: Towards an Understanding of Parenchymal Destruction and Response to Treatment. International Workshop for Pulmonary Functional Imaging Edinburgh, UK September 30th, 2015